INTERNATIONAL DOCTORAL PROGRAM IN SCIENCE
ARENBERG DOCTORAL SCHOOL
Double Doctoral Degree

UNIVERSITÀ
CATTOLICA
del Sacro Cuore

KU LEUVEN

Many-body tunneling effects in nonstandard Hubbard models

Matteo Zendra

Supervisors:

Prof. Fausto Borgonovi
Prof. Wojciech De Roeck

Dissertation presented in partial
fulfillment of the requirements
for the degree of
Doctor of Science (PhD): Physics -
Dottore di ricerca in Science
Ciclo XXXVI
S.S.D.: FIS/02

December 2024

Many-body tunneling effects in nonstandard Hubbard models

Matteo Zendra

N. Matricola (UCSC): 5015413
U-Number (KU Leuven): 0148070

Coordinator:
Prof. Luca Gavioli
(Università Cattolica del Sacro Cuore)

Examination committee:
Prof. Giuseppe Nardelli, chair
(Università Cattolica del Sacro Cuore)
Prof. Fausto Borgonovi, supervisor
(Università Cattolica del Sacro Cuore)
Prof. Wojciech De Roeck, supervisor
(KU Leuven)
Prof. Claudio Giannetti
(Università Cattolica del Sacro Cuore)
Prof. Nikolay Bobev
(KU Leuven)
Prof. Alessio Lerose
(KU Leuven)
Prof. Sandro Marcel Wimberger
(Università degli studi di Parma)

Dissertation presented in partial
fulfillment of the requirements
for the degree of
Doctor of Science (PhD): Physics -
Dottore di ricerca in Science
Ciclo XXXVI
S.S.D.: FIS/02

December 2024

© 2024 KU Leuven – Faculty of Science
Uitgegeven in eigen beheer, Matteo Zendra, Celestijnenlaan 200D, B-3001 Leuven (Belgium)

Alle rechten voorbehouden. Niets uit deze uitgave mag worden vermenigvuldigd en/of openbaar gemaakt worden door middel van druk, fotokopie, microfilm, elektronisch of op welke andere wijze ook zonder voorafgaande schriftelijke toestemming van de uitgever.
Generatieve AI werd gebruikt als een zoekmachine om meer te leren over enkele onderwerpen die in de Inleiding van de thesis worden genoemd, zoals hoogtemperatuursuperconductiviteit, kwantummagnetisme en metaal-isolatorovergangen.
De tekst/code/afbeeldingen in deze thesis zijn van mijzelf (tenzij anders vermeld) en generatieve AI is alleen gebruikt in overeenstemming met de richtlijnen van KU Leuven, waarbij de juiste referenties zijn toegevoegd. Ik heb de inhoud beoordeeld en bewerkt waar nodig, en ik neem volledige verantwoordelijkheid voor de inhoud van de thesis.

All rights reserved. No part of the publication may be reproduced in any form by print, photoprint, microfilm, electronic or any other means without written permission from the publisher.
Generative AI was used as a search engine to learn about some topics cited in the Introduction of the thesis, such as high-temperature superconductivity, quantum magnetism and metal-insulator transitions.
The text/code/images in this thesis are my own (unless otherwise specified) and generative AI has only been used in accordance with the KU Leuven guidelines and appropriate references have been added. I have reviewed and edited the content as needed and I take full responsibility for the content of the thesis.

“Take your time.
Sei un imprenditore di te stesso ora.”
F.

Abstract

The standard Hubbard model, while effective in describing interacting many-body systems, has limitations in addressing long-range and complex interparticle interactions. Specifically, the Hubbard model assumes a single-band approximation, neglecting the role of multiple electronic bands that are often critical in real materials. It also focuses only on local on-site Coulomb repulsion, overlooking the longer-range interactions between electrons at different lattice sites. Additionally, the model simplifies electron hopping by assuming uniform tunneling between nearest neighbors, failing to capture the more intricate tunneling processes observed in many materials. These simplifications make the Hubbard model inadequate for describing systems exhibiting multi-orbital effects, nonlocal interactions, or spatially varying tunneling, thus highlighting the need for extensions that account for these complexities.

To address these limitations, nonstandard Hubbard Hamiltonians, incorporating additional terms such as density-induced tunneling and pair tunneling, were proposed long ago. These terms explicitly depend on Wannier functions, which describe electron localization within the system. The standard Hubbard model employs maximally localized Wannier functions, overlooking the full spatial extent of these functions, particularly their tails. In contrast, we show here that the nonstandard Hubbard terms are strongly influenced by these tails, which play a crucial role in generating long-range interactions that significantly impact the system's dynamics.

In this thesis, we present a novel treatment of Wannier functions, developing a perturbative approach that utilizes the barrier penetration coefficient as a perturbation parameter. With these newly defined Wannier functions, we are able to evaluate the nonstandard Hubbard terms and use them to re-derive the nonstandard Hubbard Hamiltonian. Our results demonstrate that enhanced long-range interparticle interactions can lead to a mechanism for repulsive particle pairing, driven by the suppression of single-particle tunneling due to density-induced tunneling. Contrary to predictions from the standard Hubbard model, this suppression does not lead to an insulating state. Instead, it allows the coherent motion of correlated electron pairs via pair tunneling, with these pairs remaining resistant to decay caused by single-electron tunneling transitions.

Using perturbative analytical approximations and extensive numerical simulations, we further investigate nonstandard Hubbard terms and their impact on many-body dynamics, with a particular focus on tunneling dynamics in arbitrary double-well potentials. Our results show that the influence of these nonstandard terms becomes increasingly significant as the interaction strength grows, underscoring their role in driving novel transport behaviors in strongly correlated systems.

These insights are particularly relevant for understanding materials like twisted bilayer graphene and systems undergoing metal-insulator transitions, where strongly correlated interactions are crucial. By validating our model through extensive numerical simulations and comparisons with experimental data, such as second-order tunneling in optical double-well potentials, we provide a more accurate framework for analyzing strongly correlated systems. This work not only enhances our understanding of these complex materials, but also opens new paths for the study of many-body physics.

Sommario

Il modello di Hubbard standard, pur essendo efficace nella descrizione di sistemi interagenti a molti corpi, presenta limitazioni nell'affrontare interazioni a lungo raggio e interazioni interparticellari complesse. In particolare, il modello di Hubbard assume un'approssimazione a banda singola, trascurando il ruolo delle bande elettroniche multiple, spesso critiche nei materiali reali. Inoltre, il modello si concentra solo sulla repulsione coulombiana locale, trascurando interazioni a più lungo raggio tra elettroni in siti reticolari diversi. Inoltre, il modello semplifica l'*hopping* elettronico ipotizzando un *tunneling* uniforme tra primi vicini, non riuscendo a cogliere i processi di *tunneling* più intricati osservati in molti materiali. Queste semplificazioni rendono il modello di Hubbard inadeguato a descrivere sistemi che presentano effetti multiorbitali, interazioni non locali o *tunneling* che varia nello spazio, evidenziando così la necessità di estensioni che tengano conto di queste complessità.

Per ovviare a queste limitazioni, già da tempo sono state proposte Hamiltoniane di Hubbard non standard, che incorporano termini aggiuntivi come il *density-induced tunneling* e il *pair tunneling*. Questi termini dipendono esplicitamente dalle funzioni di Wannier, che descrivono la localizzazione degli elettroni all'interno del sistema. Il modello di Hubbard standard impiega funzioni di Wannier massimamente localizzate, trascurando l'intera estensione spaziale di queste funzioni, in particolare le loro code. Al contrario, questa tesi dimostra che i termini di Hubbard non standard sono fortemente influenzati da queste code, che svolgono un ruolo cruciale nel generare interazioni a lungo raggio che influenzano in modo significativo la dinamica del sistema.

Questa tesi introduce un nuovo approccio alle funzioni di Wannier, sviluppando un approccio perturbativo che utilizza il coefficiente di penetrazione della barriera come parametro perturbativo. Con le funzioni di Wannier appena definite, siamo in grado di valutare i termini di Hubbard non standard e di utilizzarli per rideterminare l'Hamiltoniana di Hubbard non standard. I nostri risultati dimostrano che l'aumento dell'intensità delle interazioni interparticellari a lungo raggio può portare ad un meccanismo di accoppiamento repulsivo delle particelle, guidato dalla soppressione del *tunneling* di particella singola dovuto al *density-induced tunneling*. Contrariamente alle previsioni del modello di Hubbard standard, questa soppressione non porta a uno stato isolante. Al contrario, essa consente il movimento coerente di coppie di elettroni correlati tramite *pair tunneling*, con queste coppie che resistono al decadimento causato dalle transizioni di *tunneling* di singolo elettrone.

Utilizzando approssimazioni analitiche perturbative e ampie simulazioni numeriche, studiamo ulteriormente i termini di Hubbard non standard e il loro impatto sulla dinamica a molti corpi, con particolare attenzione alla dinamica di *tunneling* in potenziali arbitrari a doppia buca. I nostri risultati mostrano che l'influenza di questi termini non standard diventa sempre più significativa all'aumentare dell'intensità dell'interazione, sottolineando il loro ruolo nel determinare nuovi comportamenti di trasporto in sistemi fortemente correlati.

Queste intuizioni sono particolarmente importanti per la comprensione di materiali come il *twisted bilayer graphene* e i sistemi che subiscono transizioni metallo-isolante, dove le interazioni fortemente correlate sono cruciali. Convalidando il nostro modello attraverso ampie simulazioni numeriche e confronti con dati sperimentali, come il *tunneling* del secondo ordine in potenziali ottici a doppia buca, forniamo un quadro più accurato per analizzare i sistemi fortemente correlati. Questo lavoro di tesi non solo migliora la nostra comprensione di questi materiali complessi, ma apre anche nuove strade per lo studio della fisica a molti corpi.

Beknopte samenvatting

Het standaard Hubbard-model, hoewel effectief in het beschrijven van interacties in veeldeeltjessystemen, beperkingen heeft bij het adresseren van langeafstands- en complexe interacties tussen deeltjes. Het Hubbard-model gaat specifiek uit van een enkelbandbenadering en negeert de rol van meerdere elektronische banden, die vaak cruciaal zijn in echte materialen. Bovendien richt het model zich alleen op lokale Coulomb-afstoting op dezelfde locatie, waarbij de langereafstandsinteracties tussen elektronen op verschillende roosterplaatsen worden over het hoofd gezien. Daarnaast vereenvoudigt het model het elektronenspringen door aan te nemen dat er een uniforme tunneling is tussen de dichtstbijzijnde buren, waardoor de meer complexe tunnelingprocessen die in veel materialen worden waargenomen, niet worden vastgelegd. Deze simplificaties maken het Hubbard-model ontoereikend voor het beschrijven van systemen die multi-orbitaal effecten, niet-lokale interacties of ruimtelijk variërende tunneling vertonen, wat de noodzaak benadrukt van uitbreidingen die met deze complexiteiten rekening houden.

Om deze beperkingen aan te pakken, werden al lang geleden niet-standaard Hubbard-Hamiltonianen voorgesteld, waarin extra termen zoals dichtheid-geïnduceerde tunneling en paarvormingstunneling zijn opgenomen. Deze termen zijn expliciet afhankelijk van Wannier-functies, die de lokalisatie van elektronen binnen het systeem beschrijven. Het standaard Hubbard-model maakt gebruik van maximaal gelokaliseerde Wannier-functies en negeert de volledige ruimtelijke omvang van deze functies, met name hun uitlopers. Wij tonen echter aan dat de niet-standaard Hubbard-termen sterk worden beïnvloed door deze uitlopers, die een cruciale rol spelen bij het genereren van langeafstandsinteracties die de dynamiek van het systeem aanzienlijk beïnvloeden.

In deze thesis presenteren we een nieuwe behandeling van Wannier-functies en ontwikkelen we een perturbatieve benadering die de barrière-penetratiecoëfficiënt gebruikt als een perturbatieparameter. Met deze nieuw gedefinieerde Wannier-functies kunnen we de niet-standaard Hubbard-termen evalueren en ze gebruiken om de niet-standaard Hubbard-Hamiltoniaan opnieuw af te leiden. Onze resultaten tonen aan dat verbeterde langeafstandsinteracties tussen deeltjes kunnen leiden tot een mechanisme voor afstotende deeltjesparing, gedreven door de onderdrukking van enkeldeeltjestunneling door dichtheid-geïnduceerde tunneling. In tegenstelling tot voorspellingen van het standaard Hubbard-model leidt deze onderdrukking niet tot een isolerende toestand. In plaats daarvan maakt het de coherente beweging van gecorreleerde elektronenparen mogelijk via paarvormingstunneling, waarbij deze paren bestand blijven tegen verval veroorzaakt door enkel-elektronentunnelingovergangen.

Door gebruik te maken van perturbatieve analytische benaderingen en uitgebreide numerieke simulaties onderzoeken we verder de niet-standaard Hubbard-termen en hun invloed op de dynamiek van veeldeeltjessystemen, met een bijzondere focus op tunnelingdynamiek in willekeurige dubbele-putpotentiaalvelden. Onze resultaten tonen aan dat de invloed van deze niet-standaard termen steeds significanter wordt naarmate de interactiesterkte toeneemt, wat hun rol onderstreept in het aandrijven van nieuwe transportgedragingen in sterk gecorreleerde systemen.

Deze inzichten zijn met name relevant voor het begrijpen van materialen zoals getwist bilayer-graphene en systemen die een metaal-isolatorovergang ondergaan, waar sterk gecorreleerde interacties cruciaal zijn. Door ons model te valideren via uitgebreide numerieke simulaties en vergelijkingen met experimentele gegevens, zoals tweede-orde tunneling in optische dubbele-putpotentiaalvelden, bieden we een nauwkeuriger kader voor de analyse van sterk gecorreleerde systemen. Dit werk verbetert niet alleen ons begrip van deze complexe materialen, maar opent ook nieuwe wegen voor de studie van veeldeeltjesfysica.

Contents

Abstract iii

Sommario v

Beknopte samenvatting vii

Contents ix

List of Figures xiii

1 Introduction 1

2 Nonstandard Hubbard model and electron pairing 11
- 2.1 Beyond the standard Hubbard model 12
  - 2.1.1 The cotunneling process 12
  - 2.1.2 The nonstandard Hubbard terms 13
- 2.2 Wannier functions 14
  - 2.2.1 Multiwell potential 14
  - 2.2.2 Symmetric double-well potential 15
  - 2.2.3 Symmetric triple-well potential 16
  - 2.2.4 Comments on the uniqueness of Wannier functions . . . 17
- 2.3 Two-potential approach for a double-well potential 18
  - 2.3.1 The standard orbitals 18
  - 2.3.2 The modified orbitals 19
- 2.4 Two-potential approach for a triple-well potential 21
  - 2.4.1 The triple-well spectrum 22
  - 2.4.2 Wannier functions for a triple-well potential 23
- 2.5 Nonstandard Hubbard Hamiltonian 25
  - 2.5.1 Distinguishable interacting particles in a symmetric double-well potential 25
  - 2.5.2 Contact interaction 26

2.5.3 Long-range interaction 27
2.5.4 Two interacting electrons with parallel spins in a square triple-well potential 28
2.5.5 Quantum dynamics of two interacting electrons with parallel spins in a square triple-well potential 30
2.6 Discussion 33

3 Many-body tunneling in a double-well potential 35
3.1 Nonstandard Hubbard models 36
3.1.1 Nonstandard Hubbard terms and the Wannier functions 36
3.2 Theoretical and experimental double-well potentials 38
3.3 Two-potential approach and Wannier functions for a double-well potential 39
3.3.1 Generic symmetric double-well potential 40
3.3.2 The modified orbitals 42
3.3.3 Analytical approximated and exact Wannier functions for a double-well potential: a comparison 47
3.4 Nonstandard Hubbard terms in a double-well potential 52
3.4.1 Standard and nonstandard Hubbard terms 52
3.5 Analytical approximated results with contact interaction 55
3.5.1 Contact interaction 55
3.5.2 Single-particle tunneling amplitude renormalization due to density-induced tunneling 56
3.5.3 Pair tunneling 58
3.5.4 Exact and analytical approximated results: a comparison 59
3.6 Comparison with existing literature 60
3.7 Dynamics of two distinguishable particles in a square double-well potential 63
3.7.1 Equations of motion and oscillation frequencies of a pair of distinguishable particles 63
3.7.2 Frequencies of dynamics processes and discussion 64
3.8 Comparison with experiments: two bosons in a double-well potential 67
3.9 Discussion 71

4 Conclusions and outlook 73

A Exact equations of motion of two electrons in a symmetric triple-well potential 77
A.1 Wannier functions of a symmetric triple-well potential 77
A.2 Two electrons with parallel spins in a triple-well potential . . . 79

B Two-potential approach to the bound-state spectrum and the Bardeen formula 83

B.1 The two-potential approach 83
B.2 The Bardeen formula 88

C Comparison between the extended and the single-band nonstandard Hubbard model 91
C.1 Analytical calculations 91
C.2 Discussion 92

D Squared sine double-well potential 95

E Sinusoidal double-well potential 99

F Dynamics of two distinguishable particles in a double-well potential 101

G Dynamics of two bosons in a sinusoidal double-well potential: numerical analysis and experimental comparisons 105
G.1 Dynamics of two bosons in a sinusoidal double-well potential . 105
G.2 Metal-insulator phase transition 109

Bibliography 111

List of publications 123

List of Figures

2.1 Symmetric double-well potential and single-well potentials for the two-potential approach 14
2.2 First three eigenfunctions and energy spectrum of a square triple-well potential 16
2.3 Exact calculations and analytical approximated results for left-, middle-, and right-well Wannier functions of a square triple-well potential, and corresponding orbital functions 24
2.4 Density-induced tunneling and pair tunneling as a function of the interaction range in a square double-well potential 27
2.5 Occupancy probabilities for two interacting electrons with parallel spins in a symmetric square triple-well potential, for two different geometries of the system 31
2.6 Occupancy probabilities for the case of complete single-particle tunneling suppression in a symmetric square triple-well potential, for the extended Hubbard model and the nonstandard Hubbard model 32

3.1 Symmetric double-well potential and single-well potentials for the two-potential approach 41
3.2 The theoretical framework: a symmetric square double-well potential 47
3.3 Comparison between exact and analytical approximated left-well Wannier functions in a square double-well potential and corresponding orbital function, for two different geometries of the system 50
3.4 Comparison between exact and analytical approximated results for standard and nonstandard Hubbard terms for two distinguishable particles in a square double-well potential, interacting via contact interaction 60

3.5 Comparison of exact results obtained with single-band nonstandard model and results from Ref. [1] for standard and nonstandard Hubbard terms, for two bosons in a double-well potential interacting via contact interaction 62
3.6 Time-evolution of the left-well occupancy probability of two distinguishable particles, interacting via attractive contact interaction, in a symmetric square double-well potential for standard and nonstandard Hubbard models 65
3.7 Comparison of frequencies of the different processes involved in the dynamics of two particles in a square double-well potential 66
3.8 Comparison between experimental results of Ref. [2] and Hubbard model results for the oscillation dynamics of a single boson . . 68
3.9 Comparison between experimental results of Ref. [2], Hubbard model, single-band nonstandard model and multiband nonstandard model results for the oscillation dynamics of two bosons in the weakly and strongly interacting regimes 68

A.1 Next-to-nearest neighbor interaction, density-induced tunneling and pair tunneling as a function of the interaction range, for two electrons with parallel spins in a triple-well potential, for three different geometries of the system 81

C.1 Occupancy probabilities for two interacting electrons with parallel spins in a symmetric square triple-well potential, for two different geometries, for extended Hubbard model, single-band nonstandard Hubbard model and analytical approximated results 93
C.2 Occupancy probabilities for two interacting electrons with parallel spins in a symmetric square triple-well potential, for two different interaction strengths, for extended Hubbard model, single-band nonstandard Hubbard model and analytical approximated results 94

D.1 Squared sinusoidal double-well potential with corresponding energy spectrum and comparison between exact calculations and analytical approximated results for the left-well Wannier function and corresponding orbital function 96

E.1 Sinusoidal double-well potential with corresponding energy spectrum and comparison between exact calculations and analytical approximated results for the left-well Wannier function and corresponding orbital function 100

F.1 Left and right exact Wannier functions for a symmetric square double-well potential and initial state for the dynamics 102

F.2 Time-evolution of the left well occupancy probability of two distinguishable particles, interacting via repulsive contact interaction, in a symmetric square double-well potential, for standard and nonstandard Hubbard model 103

G.1 Exponential relation between the interaction-to-tunneling ratio and the lattice depth, and relation between the lattice depth and the short-lattice amplitude 107
G.2 Average position of two interacting bosons as a function of time, with varying U/J ratios, evaluated with the standard Hubbard model, the single-band nonstandard model and the multiband nonstandard model 108
G.3 Frequency spectrum of the dynamics of two bosons as a function of the interaction-to-hopping parameter U/J, evaluated with the standard Hubbard model, the single-band nonstandard model and the multiband nonstandard model, together with density-induced tunneling term and pair tunneling term 109

Chapter 1

Introduction

The enigma of strongly correlated materials. Condensed matter physics explores the intricate world of solid materials, whose behavior and characteristics are ruled by the quantum properties of electrons. Among the many challenges in this field, understanding the dynamics of strongly correlated electron systems stands out as one of the most complex and elusive tasks [3–11]. These systems, where electron-electron interactions are so strong that they cannot be treated as independent entities, give rise to a rich variety of fascinating phenomena that continue to intrigue and puzzle physicists worldwide.

Strongly correlated materials are not just an academic curiosity, but rather they are the key to unlock some of the most intriguing mysteries of modern physics. From high-temperature superconductivity to quantum magnetism, metal-insulator transitions, and beyond, these materials exhibit behaviors that challenge our understanding and push the boundaries of what we know about the quantum world. Therefore, the study of these systems represents a journey towards understanding the fundamental principles that rule the behavior of matter at its most basic level. This exploration has the potential to revolutionize technology, leading to new materials and devices that could change the way we live and interact with the world.

High-temperature superconductivity. One of the most remarkable phenomena observed in strongly correlated systems is high-temperature superconductivity [12–29]. Unlike conventional superconductors, where electron pairing is mediated by phonon interactions, high-temperature superconductors operate at temperatures much higher than those predicted by the BCS theory. The exact mechanism that allows these materials to conduct electricity without resistance at such elevated temperatures remains one of the greatest unsolved problems in condensed matter physics. Strong correlations among electrons are believed to play a crucial role in the formation of Cooper pairs in these materials, but the precise nature of these interactions is still a subject of intense research and debate among physicists.

The discovery of high-temperature superconductors in the late 20th century was a breakthrough that promised to revolutionize technology by enabling the creation of lossless power grids, ultra-efficient magnetic levitation systems, and even quantum computers [30]. However, despite decades of research, the underlying principles that make high-temperature superconductivity possible remain elusive [31]. The interplay of electron correlations, lattice vibrations, and magnetic interactions creates a complex and delicate balance that challenges our theoretical models and experimental techniques [32]. Understanding the long-standing scientific puzzle of high-temperature superconductivity would unlock the potential of these materials for practical applications. As we continue to probe the nature of these fascinating materials, we move closer to a future where the promise of high-temperature superconductivity can be fully realized.

Magnetism in strongly correlated systems. Quantum magnetism is another phenomenon that has fascinated researchers since its discovery. The interaction of electron spins leads to the emergence of various magnetic orders, ranging from simple ferromagnetism to more exotic configurations like spin glasses and antiferromagnetic orders [33]. These magnetic states are fundamental to the functionality of many modern technologies, including data storage devices and quantum computing components.

The study of quantum magnetism provides deep insights into the behavior of strongly correlated systems. The rich variety of magnetic phases and transitions observed in these materials reflects the complex interplay between spin, charge, and lattice degrees of freedom. Understanding these interactions is crucial for developing new materials with tailored magnetic properties, which could lead to advances in memory storage, spintronics, and quantum information processing [34].

In recent years, the exploration of quantum spin liquids (a state of matter where spins remain disordered even at absolute zero) has opened up new research pathways in quantum magnetism. These highly entangled states of matter could potentially be controlled for topological quantum computation, offering a robust platform for the development of fault-tolerant quantum computers.

Metal-insulator transitions. Metal-insulator transitions provide another fascinating aspect of strongly correlated systems. In these transitions, a material can switch from being a conductor to an insulator as a result of changes in temperature, pressure, or chemical composition [35]. This transition is closely linked to the Mott insulator phase, where electron correlations prevent the material from conducting, even though band theory would predict metallic behavior.

The study of metal-insulator transitions offers a window into the complex interplay between electron localization and delocalization. In a Mott insulator, strong electron-electron interactions dominate, leading to a state where electrons are localized, and the material behaves as an insulator [36]. However, by tuning external parameters such as pressure or doping, it is possible to induce a transition to a metallic state, where electrons are free to move and conduct electricity [37]. This transition has practical implications for the development of new materials and devices. For example, the ability to control the metal-insulator transition could lead to the creation of materials with tunable electronic properties, which could be used in sensors, switches, and other electronic devices.

Beyond these well-known phenomena, strong electron correlations can lead to other complex behaviors such as charge and spin density waves, quantum spin liquids, and the fractional quantum Hall effect, where strong correlations give rise to quasiparticles with fractional charge [38]. Additionally, orbital ordering (the spatial arrangement of electron orbitals in a material) can lead to significant changes in its magnetic and electronic properties. This ordering often competes with other interactions, resulting in complex phase diagrams and rich physics that are still not fully understood.

The standard Hubbard model. To describe and predict all the fascinating phenomena observed in strongly correlated systems, physicists have developed various theoretical models, with the standard Hubbard model [39–42] emerging as a fundamental framework. The standard Hubbard model is celebrated for its simplicity and effectiveness in capturing the essence of electron correlations within a lattice structure, making it a cornerstone in the study of strongly correlated systems. In such systems, the interactions between electrons are so intense that they cannot be treated as independent particles, making traditional models inadequate.

Characterized by its simplicity and effectiveness, the standard Hubbard model is built on two main components: the kinetic energy term (Ω_0), which describes electron hopping between adjacent lattice sites, and the on-site Coulomb interaction term (U), which accounts for the repulsive ($U > 0$) or attractive ($U < 0$) forces between electrons on the same site. Despite its simplicity, this framework has proven to be remarkably powerful in explaining a wide range of phenomena in strongly correlated systems, from metal-insulator transitions to magnetic ordering.

In particular, the standard Hubbard model has been instrumental in understanding metal-insulator transitions, where a material can shift from a conducting to an insulating state depending on electron interactions. Here, strong Coulomb interactions localize electrons, leading to complex magnetic and electronic behaviors. These materials, often transition metal oxides, exhibit properties that can be accurately predicted by the standard Hubbard model, making it an indispensable tool for researchers in the field. It also provides valuable insights into magnetic ordering, where the interplay between electron hopping and on-site interactions leads to the formation and alignment of magnetic moments. Another significant application is in high-temperature superconductors, where the model helps to explore mechanisms leading to superconductivity at temperatures much higher than those predicted by conventional BCS theory.

The standard Hubbard model is particularly effective for systems where electron correlations are dominant, namely in scenarios where the on-site interaction energy U is comparable to or greater than the kinetic energy associated with electron hopping Ω_0. In this strong-coupling regime, the standard Hubbard model effectively captures the competition between electron delocalization (due to hopping) and localization (due to strong interactions).

Beyond the standard Hubbard model. Despite its success and widespread use, the standard Hubbard model has significant limitations in fully capturing the complexities of strongly correlated systems. While it offers valuable insights into single-particle dynamics and electron-electron interactions, it oversimplifies many aspects of real-world systems, particularly when higher-order interaction effects come into play [43–47]. One of its main shortcomings is its focus on single-particle dynamics, often neglecting critical higher-order interaction effects [2, 48, 49]. To address these limitations, extended and nonstandard versions of the Hubbard model have been developed, offering a more comprehensive description of many-body dynamics [43, 50–57].

The extended Hubbard model, studied extensively since the 1970s, introduces additional terms beyond the standard nearest-neighbor hopping. These include next-to-nearest-neighbor hopping, long-range interactions, and intersite Coulomb repulsion. Such extensions enable the model to capture the more complex spatial interactions and correlation effects seen in systems like transition metals and high-temperature superconductors. By incorporating these terms, the extended Hubbard model provides a more accurate understanding of electron motion and interactions in these systems.

In many real-world scenarios, electron hopping is not independent of interactions. The nonstandard Hubbard model incorporates interaction-dependent modifications, accounting for phenomena such as density-induced tunneling (DT) [43–45, 58–67] and pair tunneling (PT) [54, 68, 69], which are particularly relevant in strongly correlated systems. The DT term describes how the presence of neighboring particles modifies the tunneling rates, suppressing single-particle hopping in high-density regimes [70–83]. Meanwhile, the PT term allows for the coherent tunneling of particle pairs, a process analogous to Cooper pairing in superconductors, that can become dominant in strongly correlated regimes.

Nonstandard Hubbard terms and Wannier functions. A critical aspect of accurately evaluating these nonstandard terms involves the Wannier functions (WFs), which describe the localized states of electrons within a periodic potential, giving a real-space representation. The precise determination of WFs, including their spatial extent and tails, is crucial for evaluating the nonstandard Hubbard terms [50–52, 84]. Traditional methods, such as maximally localized Wannier functions (MLWFs) [85], often fail to account for the long tails of these functions. These tails and their overlap are essential for determining the magnitude and sign of the nonstandard terms, and their omission can lead to incomplete or inaccurate descriptions of the system's dynamics.

WFs, originally introduced by Wannier in 1937, are a crucial tool in condensed matter physics for providing a localized basis to represent electronic states in periodic systems. These functions have been extensively applied in band theory and the study of electron localization in crystalline solids. Traditional methods for constructing WFs, such as the MLWFs, have proven effective for weakly correlated systems. However, challenges arise when applying these methods to strongly correlated materials, such as Mott insulators or high-temperature superconductors. In such systems, the standard construction, typically based on non-interacting band structures, often fails to accurately capture interaction effects and may lead to incorrect descriptions of electronic states. Recent advancements, including the inclusion of many-body effects and multiband extensions, have sought to address these limitations. Building upon these developments, this thesis introduces a novel treatment of WFs tailored for nonstandard Hubbard models, improving the accuracy of interaction matrix elements, particularly in systems where correlation effects are dominant.

In this thesis, we develop a novel method for evaluating WFs that takes into account their complete spatial extent, including their critical tails. This method improves the accuracy in the evaluation of the nonstandard Hubbard terms, providing a more reliable foundation for theoretical predictions. By using these newly evaluated WFs, we can accurately capture how the lattice structure and interactions influence tunneling dynamics, leading to a more precise evaluations of DT and PT terms. This approach improves our understanding of the interplay between interactions and tunneling dynamics, crucial for modeling the behavior of strongly correlated systems.

Recent advancements in experimental techniques, particularly with ultra-cold atoms in optical lattices, have revolutionized the study of strongly correlated systems, enabling more accurate simulations [43, 45, 82, 86–95]. These experiments have uncovered several phenomena that challenge the standard Hubbard model. For instance, the standard Hubbard model fails to account for the suppression of single-particle tunneling in systems with strong long-range interactions, and it cannot describe the formation of bound states or coherent particle pairs without leading to an insulating state. Moreover, the model is unable to capture multi-particle dynamics and long-range correlations observed in these systems.

To overcome these limitations, the nonstandard Hubbard model incorporates additional terms, such as DT and PT, evaluated by considering the full spatial extent of electron WFs, including their tails, which are crucial for describing long-range interactions. The inclusion of these terms significantly improves the standard Hubbard model's ability to describe the many-body dynamics in systems with strong correlations [1, 43, 43, 45, 53, 70, 70, 96–101]. Specifically, the DT term modifies the effective tunneling rate of particles due to the presence of other particles, while the PT term facilitates the coherent tunneling of particle pairs. These terms capture interaction-driven effects that are missed by the standard Hubbard model, making them crucial for modeling the full range of behaviors experimentally seen in strongly correlated systems.

In particular, the DT effect can suppress single-particle tunneling in strongly interacting systems, leading to a regime of effective particle localization. This phenomenon reflects real experimental observations where interactions inhibit particle mobility, an indication of strong correlations. On the other hand, the PT term enables the formation of coherent particle pairs, similar to Cooper pairs in superconductivity, allowing for correlated tunneling processes that would otherwise be neglected.

As a result, the nonstandard Hubbard model offers a more comprehensive framework for understanding strongly correlated systems, providing better agreement with experimental observations and deeper insights into the underlying physics. This expanded framework is promising for explaining complex phenomena, such as superconductivity in twisted bilayer graphene and metal-insulator transitions, further enhancing its relevance in the field of condensed matter physics.

From theoretical models to optical lattices. This thesis focuses on extending the standard Hubbard model to scenarios involving periodic potentials, such as those observed in optical lattices. While this extension holds great promise, it is essential to acknowledge its limitations. The methods developed herein, though powerful, may not smoothly apply to more intricate or disordered systems without significant adaptations. Furthermore, while the new proposed WFs' evaluation method aims to enhance approximation accuracy, it remains tied to the assumptions underlying the model and the type of the potential used.

The core of this work lies in applying this theoretical framework to various potential profiles, including square double-well and sinusoidal potentials, which are particularly relevant for experimental setups like optical lattices. Our findings demonstrate that the nonstandard Hubbard model provides a more accurate description of system behavior across different interaction regimes. Notably, the inclusion of the PT term, which allows for coherent pair propagation, shows strong alignment with experimental observations, especially in explaining second-order tunneling processes. This is particularly significant in understanding the transport properties of the system, which are inadequately captured by the standard Hubbard model alone.

The square double-well potential. The square double-well potential, a simplified yet insightful model, provides an ideal framework for studying tunneling dynamics in strongly correlated systems [50, 51]. Its value lies in the fact that the potential is piecewise constant, enabling an exact solution of the Schrödinger equation. This exact solvability allows for a precise evaluation of nonstandard tunneling terms such as DT and PT, which can be directly compared to the single-particle tunneling amplitude. This comparison is essential for assessing the relevance of these nonstandard terms and understanding their true impact on the system's dynamics.

Furthermore, the double-well configuration offers a controlled environment by simplifying the problem to just two sites, while still capturing essential features of more complex lattices. By focusing on this reduced framework, we gain significant insights into the behavior of a full lattice, typically consisting of many sites, without the computational complexity of extensive numerical simulations. As a result, this model serves as a powerful tool for investigating the role of nonstandard interactions in larger, more intricate systems.

By focusing on the square double-well potential, this thesis clarifies basic tunneling dynamics, providing a benchmark for more complex scenarios. The simplicity of this model allows for a detailed examination of how electron pairs behave under the influence of DT and PT terms, offering insights that can be generalized to other potential profiles. This exploration not only validates the nonstandard Hubbard model, but also enhances our understanding of the fundamental processes that rule strongly correlated systems.

The sinusoidal potential in optical lattices. Moving from the simplicity of the square double-well to the more complex sinusoidal potential, this thesis focuses on a scenario that closely mirrors experimental conditions found in optical lattices [2]. Sinusoidal potentials, with their periodic structure, provide a rich landscape for exploring the behavior of electrons under strong correlation effects. This potential is particularly suited for investigating higher-order terms and the role of multiple energy bands, aspects that are critical for understanding the full spectrum of behaviors in strongly correlated systems.

The sinusoidal potential serves as a bridge between theoretical predictions and experimental observations, offering a realistic platform for validating our nonstandard Hubbard model. By aligning theoretical outcomes with experimental data, especially from ultra-cold atom systems, this work confirms the relevance of nonstandard terms like DT and PT in capturing complex many-body phenomena. The sinusoidal potential's correspondence to real-world experimental setups ensures that the insights gained from this study are not only theoretically significant, but also practically applicable.

Validation of the model. One of the critical aspects of this research is the validation of theoretical predictions through comparison with experimental data. Ultra-cold atom experiments in optical lattices provide an unparalleled opportunity to test the accuracy of the nonstandard Hubbard model. These experiments, with their precise control over interaction strengths and tunneling rates, are particularly well-suited for studying effects like DT and PT, key aspects of the nonstandard Hubbard model.

The nonstandard Hubbard model's predictions can be tested against these experimental results to assess the validity and accuracy of the theoretical framework. In particular, experiments have shown that the DT effect can be significant even at moderate interaction strengths, contrary to the predictions of the standard Hubbard model. Similarly, the PT term has been observed to play a crucial role in systems with strong interactions, influencing the formation of bound states and the overall transport properties of the system [102–104]. These experimental validations not only confirm the theoretical framework developed in this thesis, but also highlight the importance of incorporating nonstandard terms for a more accurate and comprehensive understanding of strongly correlated systems.

Thesis structure. This thesis is structured as follows: Ch. 2 presents an approach for evaluating the WFs in a multiwell potential, based on the two-potential approach (TPA) to tunneling problems, originally developed for tunneling to the continuum [105–107], which allows for an accurate evaluation of nonstandard Hubbard terms. Specifically, after a proper definition of the WFs of a multiwell potential in Sec. 2.2, we present the TPA in Sec. 2.3 and we apply it to the case of a triple-well potential in Sec. 2.4. Finally, in Sec. 2.5 we analyze the effect of the DT and PT terms, for both a contact interaction and a long-range constant interaction. Specifically, in Sec. 2.5.1 we analyze the case of a square double-well potential, showing that the DT term can effectively suppress the total single-particle tunneling amplitude only in the presence of a long-range interaction. In Sec. 2.5.4, we study the dynamics of two electrons with parallel spins in a square triple-well potential. In particular, we show under which conditions the nonstandard DT and PT terms become important and when the nonstandard Hubbard model should be used instead of the extended Hubbard model.

Ch. 3 presents an analysis of the nonstandard Hubbard model in a double-well potential, as well as a comparison with theoretical and experimental literature. Specifically, after recalling the TPA discussed in Ch. 2, we accurately define the WFs of a double-well potential in Sec. 3.3. In Sec. 3.4, we analyse the nonstandard Hubbard model, evaluating the corresponding nonstandard Hubbard terms through the TPA for a contact interaction in Sec. 3.5. We compare the results with existing theoretical literature in Sec. 3.6. Finally, in Sec. 3.7, we examine the effects of DT and PT terms on the dynamics of two distinguishable particles in a square double-well potential. Our findings are compared with experimental observations of Ref. [2] in Sec. 3.8, highlighting the regimes where nonstandard DT and PT terms are particularly relevant.

Finally, Ch. 4 summarizes the key findings of our research, discussing the implications of including nonstandard interaction terms into the standard Hubbard model, and highlighting the significance of our novel method for evaluating WFs. It also outlines the potential impact of these advancements on the understanding and application of strongly correlated electron systems.

A new horizon in quantum materials. As we stand at the frontier of condensed matter physics, the work presented in this thesis represents a significant step further in the theoretical modeling of strongly correlated systems. By integrating nonstandard terms into the standard Hubbard model and refining the evaluation of the WFs, this research offers a more precise framework for exploring the complexities of these systems. The theoretical advancements achieved here may have real-world implications, paving the way for future explorations into high-temperature superconductivity, quantum magnetism, metal-insulator transitions, and other phenomena that lie at the heart of modern physics.

Finally, the journey outlined in this thesis is far from complete. As we continue to refine and expand our theoretical models, we move closer to a comprehensive understanding of the quantum world. The improved models developed here are expected to serve as a foundation for future research, enabling scientists to probe deeper into the mysteries of strongly correlated systems. The potential applications of this work are wide, ranging from the development of new materials with tailored properties to advances in quantum computing.

Chapter 2

Nonstandard Hubbard model and electron pairing

This chapter is an adaptation of the published article [50].

In this Chapter, we present a nonstandard Hubbard model applicable to arbitrary potential profiles and interparticle interactions. Our approach involves a novel treatment of Wannier functions (WFs), free from the ambiguities of conventional methods and applicable to finite systems without periodicity constraints.

To ensure a consistent evaluation of the WFs, we develop a perturbative approach, employing the barrier penetration coefficient as a perturbation parameter. With the newly defined WFs as a basis, we derive the Hubbard Hamiltonian, revealing the emergence of density-induced tunneling (DT) and pair tunneling (PT) terms alongside standard contributions.

Our investigation demonstrates that long-range interparticle interactions can induce a mechanism for repulsive particle pairing. This mechanism relies on the effective suppression of single-particle tunneling due to DT. Contrary to expectations based on the standard Hubbard model, an increase in interparticle interaction does not lead to an insulating state. Instead, our proposed mechanism implies the coherent motion of correlated electron pairs, similar to bound states within a multiwell system, resistant to decay from single-electron tunneling transitions. These findings carry significant implications for various phenomena, including the formation of flat bands, the emergence of superconductivity in twisted bilayer graphene, and the possibility of a metal-insulator transition.

We present an approach for evaluating the WFs in a multiwell potential, based on the two-potential approach (TPA) to tunneling problems, originally developed for tunneling to the continuum, see Refs. [105–107], which allows for an accurate evaluation of nonstandard Hubbard terms. Specifically, after a proper definition of the WFs of a multiwell potential in Sec. 2.2, we present the TPA in Sec. 2.3 and we apply it to the case of a triple-well potential in Sec. 2.4. Finally, in Sec. 2.5 we analyze the effect of the PT and DT terms, for both a contact interaction and a long-range constant interaction. Specifically, in Sec. 2.5.1 we analyze the simple case of a square double-well potential, showing that the DT term can effectively suppress the total single-particle tunneling amplitude only in the presence of a long-range interaction. In Sec. 2.5.4, we study the dynamics of two electrons with parallel spins in a square triple-well potential. In particular, we show under which conditions the nonstandard DT and PT terms become significant and when the nonstandard Hubbard model should be used instead of the extended Hubbard model (which neglects DT and PT contributions).

2.1 Beyond the standard Hubbard model

2.1.1 The cotunneling process

Electron pairing in solids has traditionally been attributed to phonon-mediated attraction. However, a fundamental question is whether repulsive particles can form pairs independently of the presence of phonons. To explore this idea further, we examine two interacting electrons within the same site of a periodic structure, as described by the Hubbard model [39]. When the on-site two-particle repulsive energy, denoted as U, significantly exceeds the tunneling coupling Ω, *single-electron* hopping to a neighboring site is strongly suppressed due to the large energy mismatch. Concerning the tunneling of an electron pair, the *elastic* two-electron hopping (known as “cotunneling”) is also suppressed in the standard Hubbard model. Indeed, the corresponding amplitude representing two consecutive hoppings is a second-order process that involves a large virtual energy variation $\sim 2\Omega^2/U$ [2], which decreases with U. Even if weak, this second-order process survives for any finite interaction U, so that the repulsive interaction cannot completely localize the electron pair within the framework of the standard Hubbard model.

2.1.2 The nonstandard Hubbard terms

It is evident that the standard Hubbard Hamiltonian fails to capture all the interaction effects [43–45]. For instance, the cotunneling process can occur with both particles staying together, without changing their total energy, a nonstandard Hubbard process known as PT [43]. Even with increasing U, the latter can become a major contributor to the cotunneling process [53]. Indeed, even in the case of single-electron tunneling coupling suppression ($\Omega \to 0$), PT remains uninhibited, offering an effective mechanism for electron pairing, independent of the attractive interaction. A similar idea was proposed by Anderson in the theory of cuprate superconductivity in Ref. [69]. Inspired by this idea, we demonstrate how this specific mechanism can be realized within the framework of a nonstandard Hubbard model, which includes both the pair tunneling term and the DT term, also known as *bond-charge interaction* [43–45, 58–65].

While the influence of the PT term on superconductivity is rather obvious, the effect of the DT term (with the adequate sign) also favors superconductivity. Indeed, analytical demonstrations have highlighted the role of this term in supporting the emergence of superconductivity within models characterized by repulsive on-site interaction at half filling [67]. Thus, the DT and PT terms play a crucial role in electron dynamics, both in terms of their magnitude and sign. Specifically, we show that the DT term, in the presence of a long-range interparticle interaction, has the ability to lower and even totally suppress the single-particle coupling, due to an effective mean-field generated by the other particles, thus providing stability of the electron pair.

An extension of the standard Hubbard model concerning strongly correlated systems has been explored long ago in Ref. [70]. However, only recently has the nonstandard Hubbard model attracted more attention, particularly due to experimental results with ultracold atoms in optical lattices [43, 45, 96–98], as well as because they have been shown to host many different effects, ranging from superconducting pairing to localization [73–81]. Currently, the accurate evaluation of nonstandard Hubbard terms and the understanding of their influence on the dynamics of correlated systems remain open problems. Indeed, these terms are closely related to the overlap of WFs from adjacent sites, often accurately represented by the corresponding orbital wave functions. However, their overlap, crucially dependent on their tails being situated in neighboring sites, significantly affects both the magnitude and sign of nonstandard Hubbard terms, on which consensus is yet to be reached [1, 43, 70].

2.2 Wannier functions

2.2.1 Multiwell potential

Let us consider a particle placed in an N-site potential chain

$$\mathcal{V}(x) = \sum_{j=1}^{N} \mathcal{V}_j(x)\,, \tag{2.2.1}$$

where $\mathcal{V}(x) \to 0$ as $x \to \pm\infty$. The exact eigenstates are obtained from the Schrödinger equation (we take $\hbar = 1$)

$$\mathcal{H}\,|\psi_k\rangle \equiv \left(-\frac{\nabla_x^2}{2m} + \mathcal{V}(x)\right)|\psi_k\rangle = \mathcal{E}_k\,|\psi_k\rangle\ , \tag{2.2.2}$$

with boundary conditions at infinity ($x \to \pm\infty$) given by

$$\psi_k(x) \sim e^{-\sqrt{-2m\mathcal{E}_k}|x|} \tag{2.2.3}$$

that uniquely define the bound state energy spectrum ($\mathcal{E}_k < 0$) of the exact Hamiltonian $\mathcal{H}$. We assume that the N lowest eigenstates form a band, well separated from the other eigenstates of the spectrum.

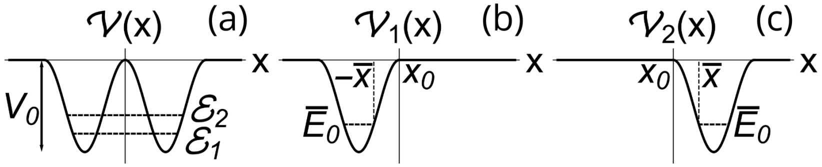

Figure 2.1: (a) Symmetric double-well potential $\mathcal{V}(x) = \mathcal{V}_1(x) + \mathcal{V}_2(x)$, with lattice depth V_0. Dashed lines represent the first two lowest-band energy levels $\mathcal{E}_{1,2}$. (b), (c) Single-well potentials $\mathcal{V}_{1,2}(x)$, with classical turning points $\mp\,\overline{x}$, so that $\mathcal{V}_{1,2}\left(\mp\,\overline{x}\right) = \overline{E}_0$, the single-site ground state energy. The separation point x_0 is defined so that $\mathcal{V}_1(x_0) = \mathcal{V}_2(x_0) = 0$.

We consider the corresponding tight-binding tunneling Hamiltonian H_N, which describes the lowest band of the exact Hamiltonian $\mathcal{H}$, given by

$$H_N = \sum_{j=1}^{N} \overline{E}_j\,|\Psi_j\rangle\,\langle\Psi_j| + \sum_{j=1}^{N-1} \overline{\Omega}_j\,(|\Psi_j\rangle\,\langle\Psi_{j+1}| + H.c.)\ , \tag{2.2.4}$$

where $\overline{E}_j$ represents the single-site energy, $\overline{\Omega}_j$ is the nearest neighbor tunneling coupling, while

$$\Psi_j(x) = \langle x|\Psi_j\rangle$$

are the WFs. In order to define $\overline{E}_j$ and $\overline{\Omega}_j$ in a consistent way, we identify the spectrum of the tunneling Hamiltonian in Eq. (2.2.4) with the one of the lowest bands of the original Hamiltonian $\mathcal{H}$ in Eq. (2.2.2). When employing such a procedure, unlike when solving exactly the Schrödinger Eq. (2.2.2), we are neglecting the influence of interband transitions on electrons' motion. Indeed, if the lowest band is sufficiently separated from the other bands, the exact spectrum obtained from Eq. (2.2.2) and the one of the tunneling Hamiltonian will produce the same dynamics. Therefore, we diagonalize the Hamiltonian H_N by a unitary transformation R and then we apply the same transformation to the lowest-band spectrum, namely $\mathcal{E}_k$ and $|\psi_k\rangle$, to obtain the WFs. In particular, these are uniquely defined by

$$|\Psi_k\rangle = \sum_{k'=1}^{N} R_{kk'}\,|\psi_{k'}\rangle\ . \tag{2.2.5}$$

Notice that the exact eigenfunctions $\psi_k(x)$ do not contain uncertainty, as belonging to the bound-state spectrum of the Schrödinger Eq. (2.2.2). In the following, we will illustrate the unitary transformation given in Eq. (2.2.5) for the double-well and triple-well potential cases (for further details, see Appendix A).

2.2.2 Symmetric double-well potential

Let us exemplify this method considering the symmetric double-well potential $\mathcal{V}(x)$ in Fig. 2.1(a), where the lowest band contains two eigenstates $\psi_{1,2}(x)$, with corresponding eigenenergies $\mathcal{E}_{1,2}$. The tunneling Hamiltonian of this system is given by Eq. (2.2.4) for $N=2$ and can be explicitly written as

$$H_2 = \overline{E}_0 \sum_{j=1}^{2} |\Psi_j\rangle\langle\Psi_j| + \overline{\Omega}_0\left(|\Psi_1\rangle\langle\Psi_2| + H.c.\right)\ . \tag{2.2.6}$$

By diagonalizing H_2 through the unitary transformation R in Eq. (2.2.5), and identifying its eigenspectrum with $\mathcal{E}_{1,2}$ and $\psi_{1,2}(x)$, we find

$$\overline{E}_0 = \frac{1}{2}\left(\mathcal{E}_1 + \mathcal{E}_2\right) , \tag{2.2.7a}$$

$$\overline{\Omega}_0 = \frac{1}{2}\left(\mathcal{E}_1 - \mathcal{E}_2\right) , \tag{2.2.7b}$$

$$\Psi_{1,2}(x) = \frac{1}{\sqrt{2}}\left[\psi_1(x) \pm \psi_2(x)\right] . \tag{2.2.7c}$$

In contrast with the “extended”eigenstates $\psi_{1,2}(x)$, the WFs $\Psi_{1,2}(x)$ are localized respectively in the left and right well, although their tails are extended to the neighboring wells.

2.2.3 Symmetric triple-well potential

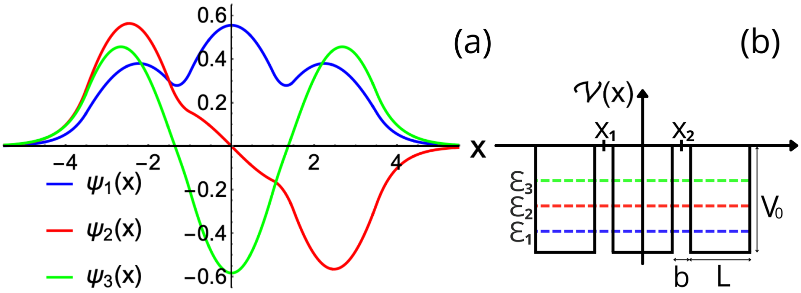

Figure 2.2: (a) First three exact eigenfunctions $\psi_1(x)$ (blue curve), $\psi_2(x)$ (red curve) and $\psi_3(x)$ (green curve) of a square triple-well potential. (b) Symmetric square triple-well potential. The three wells have width L and depth V_0 and are separated by barriers of width b, where $x_{1,2}$ are the separation points. Dashed colored lines represent the first three exact energy levels of the system $\mathcal{E}_{1,2,3}$, corresponding to the eigenfunctions shown in panel (a), which read $\mathcal{E}_1 = -4.171$, $\mathcal{E}_2 = -3.897$ and $\mathcal{E}_3 = -3.545$. Parameters: $L = 2$, $b = 0.5$ and $V_0 = 5$, in arbitrary units.

This procedure can be easily extended for the symmetric triple-well potential ($N = 3$) in Fig. 2.2, where the lowest band consists of three eigenstates $\psi_{1,2,3}(x)$ with energies $\mathcal{E}_1 < \mathcal{E}_2 < \mathcal{E}_3$. The corresponding tight-binding tunneling

Hamiltonian, given by Eq. (2.2.4) for $N = 3$, can be explicitly written as

$$H_3 = \overline{E}_0 \sum_{j=1}^{3} |\Psi_j\rangle \langle\Psi_j| + \overline{\Omega}_0 \left(|\Psi_1\rangle \langle\Psi_2| + |\Psi_2\rangle \langle\Psi_3| + H.c.\right) . \tag{2.2.8}$$

Following the same procedure, i.e., by diagonalizing H_3 and identifying the obtained spectrum with the exact lowest-band one, we obtain

$$\begin{aligned}
\overline{E}_0 &= \frac{1}{2}\left(\mathcal{E}_1 + \mathcal{E}_3\right) , \\
\overline{\Omega}_0 &= \frac{1}{2\sqrt{2}}\left(\mathcal{E}_1 - \mathcal{E}_3\right) , \\
\Psi_1(x) &= \frac{1}{2}\psi_1(x) + \frac{1}{\sqrt{2}}\psi_2(x) + \frac{1}{2}\psi_3(x) , \\
\Psi_2(x) &= \frac{1}{\sqrt{2}}\left[\psi_1(x) - \psi_3(x)\right] , \\
\Psi_3(x) &= \frac{1}{2}\psi_1(x) - \frac{1}{\sqrt{2}}\psi_2(x) + \frac{1}{2}\psi_3(x) .
\end{aligned} \tag{2.2.9}$$

As in the previous case, the WFs $\Psi_{1,2,3}(x)$ are respectively localized in the left, middle and right well, and are uniquely defined.

2.2.4 Comments on the uniqueness of Wannier functions

Let us point out that our approach for a consistent determination of the tunneling Hamiltonian parameters and the related WFs can be generalized for an arbitrary number of potential wells N, regardless of the periodicity of $\mathcal{V}(x)$. Additionally, we observe that, for a *periodic* potential $\mathcal{V}(x)$, in the limit $N \to \infty$, this procedure looks similar to the method used to derive a set of localized WFs from the Bloch functions, subjected to periodic boundary conditions, through a unitary transformation. However, due to the additional “gauge freedom”, the resulting WFs become strongly nonunique, so that different choices of the gauge correspond to different sets of WFs having different shapes and spreads.

A widely used approach to avoid the gauge freedom consists in a proper choice of the unitary transformation of the Bloch functions that enforces the maximal localization of the WFs (see Ref. [85] for a detailed discussion). However, this procedure does not guarantee that the tunneling Hamiltonian dynamics corresponds to that obtained from the exact solution of the original multiwell Schrödinger equation.

In contrast, our approach is based on this correspondence, which allows one to uniquely construct the tunneling Hamiltonian and the WFs by assuming only the single-band (SB) approximation. Notice that the resulting WFs, although localized at the corresponding site, exhibit *tails* penetrating to neighboring sites. These tails play a crucial role in the evaluation of the nonstandard Hubbard terms, as we will show in the following. On the contrary, the condition of maximal localization of the WFs would decrease correspondingly the contribution from these tails and therefore the amplitude of the nonstandard Hubbard terms. Since our approach relates the WFs to the exact Schrödinger eigenstates, in the next Section we present a consistent perturbative approach for their evaluation in terms of single-site orbitals.

2.3 Two-potential approach for a double-well potential

2.3.1 The standard orbitals

Let us consider the symmetric double-well potential in Fig. 2.1(a), given by the sum of two single-well potentials

$$\mathcal{V}(x) = \mathcal{V}_1(x) + \mathcal{V}_2(x)\,,$$

such that $\mathcal{V}_1(x) = 0$ for $x \geq x_0$ and $\mathcal{V}_2(x) = 0$ for $x \leq x_0$, where $x_0 = 0$ is the separation point; see Figs. 2.1(b) and 2.1(c). The lowest eigenstates (orbitals) of the left- and right-well Hamiltonians are obtained from

$$\left(-\frac{\nabla_x^2}{2m} + \mathcal{V}_{1,2}(x)\right)\Phi_0^{(1,2)}(x) = E_0\Phi_0^{(1,2)}(x)\,, \tag{2.3.1}$$

with the following boundary conditions:

$$\begin{aligned} &\Phi_0^{(1)}(x) \sim e^{\sqrt{-2mE_0}x} \quad \text{as} \quad x \to -\infty\,, \\ &\Phi_0^{(1)}(x) = \Phi_0^{(1)}(0)e^{-\sqrt{-2mE_0}x} \quad \text{as} \quad x \geq x_0\,, \end{aligned} \tag{2.3.2}$$

and similarly for $\Phi_0^{(2)}(x) = \Phi_0^{(1)}(-x)$. These orbitals can be used as a basis to obtain the eigenstates $\psi_{1,2}(x)$ and the WFs $\Psi_{1,2}(x) \equiv \Psi_{L,R}(x)$, through a perturbative approach. For instance, we could consider the left-well orbital $\Phi_0^{(1)}(x)$ as the unperturbed state and the right-well potential $\mathcal{V}_2(x)$ as the perturbation (or vice versa).

However, such a perturbative approach does not include a small parameter, which makes the corresponding expansion unusable. This issue can be solved by employing the TPA, which uses an alternative expansion in powers of the orbitals overlap

$$\beta \equiv \langle \Phi_0^{(1)} | \Phi_0^{(2)} \rangle \ , \tag{2.3.3}$$

a small parameter proportional to the barrier penetration coefficient

$$T_0 = \exp\left(- \int_{-\overline{x}}^{\overline{x}} |p(x')| \, dx' \right) \ll 1 \, . \tag{2.3.4}$$

Here, $p(x)$ represents the (imaginary) momentum under the potential barrier and $\pm\overline{x}$ are the classical turning points, shown in Figs. 2.1(b) and 2.1(c) (for further details, see Appendix B). Using this approach, we derive the tunneling Hamiltonian parameters in Eq. (2.2.7a) and Eq. (2.2.7b), which read

$$\overline{E}_0 = E_0 + \mathcal{O}\left(\beta^2\right) \ ,$$

$$\overline{\Omega}_0 = \Omega_0 + \mathcal{O}\left(\beta^2\right) \ ,$$

where E_0 is given by Eq. (2.3.1), and

$$\Omega_0 = -\sqrt{\frac{2|E_0|}{m}} \left[\Phi_0(0)\right]^2 \propto T_0 \tag{2.3.5}$$

is a simplified (1D) version of the well-known Bardeen formula [108]. Similarly, we obtain

$$\mathcal{E}_{1,2} = E_\pm + \mathcal{O}\left(\beta^2\right) \ ,$$

where

$$E_\pm = E_0 \pm \Omega_0 \, .$$

Consequently, all the parameters of the tunneling Hamiltonian are completely determined by the single-well orbitals.

2.3.2 The modified orbitals

At first glance, we may expect to derive the eigenstates $\psi_{1,2}(x) \equiv \psi_{1,2}(E_\pm, x)$ from Eq. (2.2.7c) by replacing the WFs $\Psi_{1,2}(x)$ with the corresponding orbitals $\Phi_0^{(1,2)}(x) \equiv \Phi_0^{(1,2)}(E_0, x)$ given by Eq. (2.3.1), so that

$$\psi_{1,2}(E_\pm, x) \simeq \frac{1}{\sqrt{2}} \left[\Phi_0^{(1)}(E_0, x) \pm \Phi_0^{(2)}(E_0, x) \right] \, . \tag{2.3.6}$$

However, Eq. (2.3.6) exhibits an inconsistency between the energy arguments of $\psi_{1,2}(E_\pm, x)$ and $\Phi_0^{(1,2)}(E_0, x)$. To solve this issue, we introduce an energy shift in the orbital functions by replacing the ground state energy E_0 with a free parameter $E < 0$. The resulting modified orbitals $\overline{\Phi}^{(1,2)}(E, x)$ (normalized to unity) are obtained from Eq. (2.3.1) with the substitution $E_0 \to E$ and imposing the boundary condition at infinity given in Eqs. (2.3.2). However, unlike $\Phi_0^{(1,2)}(E_0, x)$, the modified orbitals $\overline{\Phi}^{(1,2)}(E, x)$ are defined respectively on two different segments

$$\mathcal{X}_1 = (-\infty, 0) \quad \text{and} \quad \mathcal{X}_2 = (0, \infty)\,,$$

and vanish elsewhere. As a result, they are *nonoverlapping* and therefore *orthogonal*. Replacing $\Phi_0^{(1,2)}(E_0, x)$ in Eq. (2.3.6) with $\overline{\Phi}^{(1,2)}(E_\pm, x)$, we obtain

$$\psi_{1,2}(E_\pm, x) = \frac{1}{\sqrt{2}}\left[\overline{\Phi}^{(1)}(E_\pm, x) \pm \overline{\Phi}^{(2)}(E_\pm, x)\right], \tag{2.3.7}$$

which gives the *exact* result for $\psi_{1,2}(E_\pm, x)$, in contrast with Eq. (2.3.6). Indeed, the exact treatment of the Schrödinger Eq. (2.2.2) involves solving it on the two segments and combining the results by imposing the continuity condition at the separation point. This condition is automatically satisfied if $E_\pm$ are the energies of the symmetric and antisymmetric states, respectively.

Substituting Eq. (2.3.7) into Eq. (2.2.7c), we obtain the exact left- and right-well WFs, $\Psi_{L,R}(x)$, in terms of the modified orbitals:

$$\begin{aligned}
\Psi_L(x) &= \frac{1}{2}\left[\overline{\Phi}_+^{(1)}(x) + \overline{\Phi}_+^{(2)}(x) + \overline{\Phi}_-^{(1)}(x) - \overline{\Phi}_-^{(2)}(x)\right], \\
\Psi_R(x) &= \frac{1}{2}\left[\overline{\Phi}_+^{(1)}(x) + \overline{\Phi}_+^{(2)}(x) - \overline{\Phi}_-^{(1)}(x) + \overline{\Phi}_-^{(2)}(x)\right],
\end{aligned} \tag{2.3.8}$$

where

$$\overline{\Phi}_\pm^{(1,2)}(x) \equiv \overline{\Phi}^{(1,2)}(E_0 \pm \Omega_0, x)\,.$$

Expanding the modified orbitals in powers of Ω_0 and neglecting $\mathcal{O}\left(\Omega_0^2\right)$ terms (since $\Omega_0 \propto \beta \propto T_0$) we obtain

$$\overline{\Phi}_\pm^{(1,2)}(x) = \overline{\Phi}_0^{(1,2)}(x) \pm \Omega_0\, \partial_E \overline{\Phi}_0^{(1,2)}(x)\,, \tag{2.3.9}$$

where

$$\overline{\Phi}_0^{(1,2)}(x) \equiv \begin{cases} \Phi_0^{(1,2)}(E_0, x) & \text{for } x \in \mathcal{X}_{1,2} \\ 0 & \text{elsewhere} \end{cases}, \tag{2.3.10}$$

and

$$\partial_E \overline{\Phi}_0^{(1,2)}(x) \equiv \left(\frac{\partial \overline{\Phi}^{(1,2)}(E, x)}{\partial E}\right)_{E=E_0}.$$

Substituting Eq. (2.3.9) into Eqs. (2.3.8), we get

$$\begin{aligned}\Psi_L(x) &= \overline{\Phi}_0^{(1)}(x) + \Omega_0 \partial_E \overline{\Phi}_0^{(2)}(x)\,,\\ \Psi_R(x) &= \overline{\Phi}_0^{(2)}(x) + \Omega_0 \partial_E \overline{\Phi}_0^{(1)}(x)\,,\end{aligned} \tag{2.3.11}$$

which represents our main result for the WFs. Looking at Eqs. (2.3.11), we can observe that each WF consists of two *nonoverlapping* terms, describing respectively the WF inside the respective well (first term) and its tail penetrating into the neighboring well (second term), which is $\propto \Omega_0$ and therefore much smaller than the first term. Since $\overline{\Phi}^{(1,2)}(E,x)$ are normalized to unity for any E, we can explicitly demonstrate the orthogonality of the WFs by using

$$\partial_E \int\limits_{-\infty}^{0} \left[\overline{\Phi}^{(1)}(E,x)\right]^2 dx = 0\,,$$

so that

$$\langle \Psi_L | \Psi_R \rangle = 2\Omega_0 \int\limits_{-\infty}^{0} \overline{\Phi}_0^{(1)}(x) \partial_E \overline{\Phi}_0^{(1)}(x)\, dx = 0\,. \tag{2.3.12}$$

Equation (2.3.12) represents the overlap of the orbital $\overline{\Phi}_0^{(1)}(x)$, which is nodeless, with the tail of the WF belonging to the adjacent well; see Eqs. (2.3.11). From Eq. (2.3.12), it clearly follows that the WF tail must change its sign, deeply affecting the amplitudes of the nonstandard Hubbard terms. Finally, we point out that Eqs. (2.3.11) are valid for an arbitrary multiwell system. In the next Section, we exemplify this by comparing the WFs given by Eqs. (2.3.11) with the exact numerical results for a symmetric square triple-well potential.

2.4 Two-potential approach for a triple-well potential

In this Section, we explicitly demonstrate the accuracy of our analytical approach by analyzing the WFs of the symmetric square triple-well potential shown in Fig. 2.2(b). Specifically, we evaluate the WFs by using the TPA and we compare them with the exact WFs given by Eqs. (2.2.9), as well as with the corresponding orbital functions. For simplicity, we consider a square well potential, since its shape allows us to obtain simple analytical expressions for the WFs, which will be used for the evaluation of the nonstandard Hubbard terms, highlighting their explicit dependence on the quantum well parameters.

2.4.1 The triple-well spectrum

The triple-well spectrum, namely the eigenfunctions $\psi_k(x) \equiv \psi_k(\mathcal{E}_k, x)$ and the eigenvalues $\mathcal{E}_k$, is obtained by solving the Schrödinger Eq. (2.2.2) with boundary conditions given by Eq. (2.2.3). We focus on the three lowest-band eigenstates (with $k = 1, 2, 3$) displayed in Fig. 2.2(a). The corresponding exact left-, middle-, and right-well WFs $\Psi_{L,M,R}(x)$ can be obtained from the lowest-band eigenstates through Eqs. (2.2.9). On the other hand, we notice that the energy $\overline{E}_0$ in the tunneling Hamiltonian in Eq. (2.2.8) corresponds to the energy of the lowest orbital $\Phi_0(x)$ given by Eq. (2.3.1) by considering the single-well potential

$$\mathcal{V}(x) = -V_0 \quad \text{for} \quad -\frac{L}{2} < x < \frac{L}{2}\,.$$

Specifically, the lowest single-well orbital can be written as

$$\Phi_0(x) = \mathcal{N}_0 \begin{cases} \sqrt{1-\frac{|E_0|}{V_0}}\,e^{q_0\left(x+\frac{L}{2}\right)} & \text{for } -\infty < x < -\frac{L}{2} \\ \cos\left(p_0 x\right) & \text{for } -\frac{L}{2} < x < \frac{L}{2} \\ \sqrt{1-\frac{|E_0|}{V_0}}\,e^{-q_0\left(x-\frac{L}{2}\right)} & \text{for } \quad \frac{L}{2} < x < \infty \end{cases}\,, \tag{2.4.1}$$

where

$$p_0 = \sqrt{2m(V_0 + E_0)}\,,$$
$$q_0 = \sqrt{-2mE_0}\,,$$

and

$$\mathcal{N}_0 = \sqrt{2q_0/(2 + Lq_0)}$$

is the normalization factor. As a result, the orbital functions for the triple-well system (respectively for the left, middle and right well) read

$$\begin{aligned} \Phi_0^{(1)}(x) &\equiv \Phi_0(x + L + b)\,, \\ \Phi_0^{(2)}(x) &\equiv \Phi_0(x)\,, \\ \Phi_0^{(3)}(x) &\equiv \Phi_0(x - L - b)\,. \end{aligned} \tag{2.4.2}$$

Substituting $\Phi_0\left(\frac{L+b}{2}\right)$ into Eq. (2.3.5), we obtain for the tunneling energy

$$\Omega_0 = -\sqrt{\frac{2|E_0|}{m}}\mathcal{N}_0^2\left(1 - \frac{|E_0|}{V_0}\right)e^{-q_0 b}\,. \tag{2.4.3}$$

For the single-well parameters used in Fig. 2.2, solving Eq. (2.3.1) and Eq. (2.4.3) we obtain $E_0 = -3.8525$ and $\Omega_0 = -0.2216$. These values can be compared with those obtained from the exact numerical solution of the Schrödinger equation for the triple-well potential, namely $\overline{E}_0 = -3.858$ and $\overline{\Omega}_0 = -0.2215$. Their closeness confirms the high accuracy of the TPA for a consistent determination of the tunneling Hamiltonian parameters.

2.4.2 Wannier functions for a triple-well potential

Finally, let us evaluate the corresponding WFs that can be obtained by extending Eqs. (2.3.11) to a triple-well system. By following the same procedure of the square double-well potential case, we construct the eigenstates $\psi_k(x)$ through the modified orbitals, with energy shift

$$\mathcal{E}_k - E_0 \propto \Omega_0 \,.$$

We then obtain the WFs from the eigenstates $\psi_k(x)$ via the unitary transformation in Eq. (2.2.5). By expanding the resulting WFs in powers of Ω_0 up to $\mathcal{O}\left(\Omega_0^2\right)$ terms, we get a simple result representing the straightforward extension of Eqs. (2.3.11), given by

$$\begin{aligned}
\Psi_L(x) &= \overline{\Phi}_0^{(1)}(x) + \Omega_0 \partial_E \overline{\Phi}_0^{(2)}(x)\,, \\
\Psi_M(x) &= \overline{\Phi}_0^{(2)}(x) + \Omega_0 \left[\partial_E \overline{\Phi}_0^{(1)}(x) + \partial_E \overline{\Phi}_0^{(3)}(x)\right]\,, \\
\Psi_R(x) &= \overline{\Phi}_0^{(3)}(x) + \Omega_0 \partial_E \overline{\Phi}_0^{(2)}(x)\,.
\end{aligned} \tag{2.4.4}$$

As in the double-well case, $\overline{\Phi}_0^{(1,2,3)}(x)$ denote the left-, middle-, and right-well modified orbitals, respectively coinciding with $\Phi_0^{(1,2,3)}(x)$ of Eqs. (2.4.2) on the intervals $(-\infty, x_1)$, (x_1, x_2), and (x_2, ∞), and vanishing elsewhere. The separation points $x_{1,2}$ are taken at the center of the interwell barriers, as shown in Fig. 2.2(b).

Looking at Eqs. (2.4.4), we notice that the WFs for the triple-well system are given by the same expressions of the double-well system in Eq. (2.3.11). Indeed, the first term representing the WF inside the respective well is given by the orbital, while the second term (with derivatives) describing the WF tails penetrating to neighboring wells is proportional to Ω_0. Let us remark that the latter represents the energy shift (tunneling energy) for the *double-well* potential. Remarkably, even if the energy shift in the triple-well case is different ($\mathcal{E}_1 - E_0 = \sqrt{2}\Omega_0$), see Eqs. (2.2.9), the $\sqrt{2}$ factor cancels out during the derivation, confirming that the WF tail is always determined by the tunneling coupling to the neighboring well.

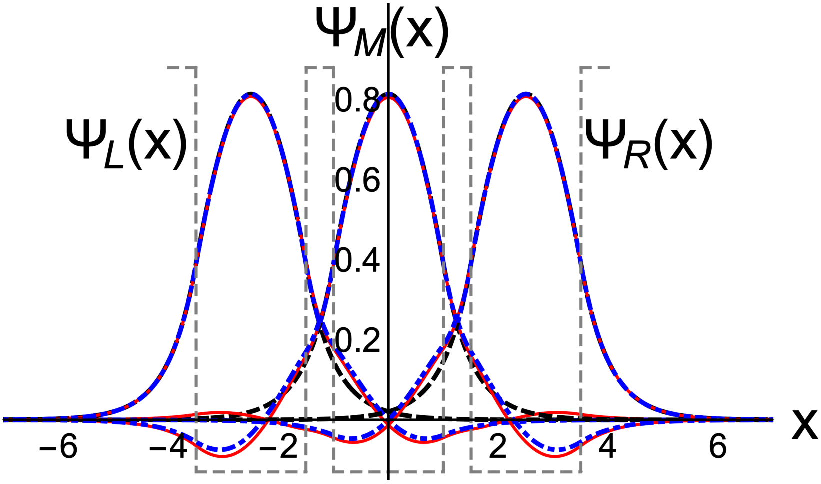

Figure 2.3: Left-, middle-, and right-well WFs for the square triple-well potential shown with dashed gray lines. Red solid curves correspond to exact calculations in Eq. (2.2.9), blue dashed curves show our analytical results obtained with the TPA in Eqs. (2.4.4), and black dashed curves show the orbital functions $\Phi_0^{(1,2,3)}(x)$ in Eqs. (2.4.2). Parameters: $L = 2$, $b = 0.5$ and $V_0 = 5$, in arbitrary units.

In Fig. 2.3, we compare the WFs $\Psi_{L,M,R}(x)$ in Eqs. (2.4.4) obtained with the TPA (blue dashed curves) with the orbital functions $\Phi_0^{(1,2,3)}(x)$ in Eqs. (2.4.2) (black dashed curves) and the exact results in Eq. (2.2.9) obtained via numerical calculations (red solid curves). We observe that the orbitals $\Phi_0^{(1,2,3)}(x)$ provide a close approximation to the corresponding exact WFs $\Psi_{L,M,R}(x)$ within each well, despite notable differences in their tails into neighboring wells. Furthermore, the approximate results closely match the exact ones, even in the regions of the tails (beyond the respective well), underscoring the precision of the TPA. Ultimately, we notice that the tails of the WFs into the neighboring wells are less pronounced for the left and right wells compared to the middle well, due to the slightly different boundary conditions for the modified orbitals of the external wells, as described in Eqs. (2.3.2).

2.5 Nonstandard Hubbard Hamiltonian

In this Section, we derive the nonstandard Hubbard terms using our analytical expression for the double-well WFs in Eqs. (2.3.11) and we show how these nonstandard Hubbard terms can be used to suppress single-particle tunneling in the presence of long-range interparticle interaction.

2.5.1 Distinguishable interacting particles in a symmetric double-well potential

The interaction between two particles in a double-well potential can be described by a two-body *repulsive* potential $V(x-y) > 0$. Since the many-body basis for two distinguishable particles is given by the tensor product of the single-particle WFs, the matrix elements of the interaction term for two distinguishable particles in the tunneling Hamiltonian basis are given by

$$V_{i'j'ij} = \int \Psi_{i'}(x)\Psi_{j'}(y)V(x-y)\Psi_i(x)\Psi_j(y)\,dx\,dy\,. \tag{2.5.1}$$

Here, $\Psi_i(x)$ is the WF at site $i = L, R$ of the symmetric double-well potential in Fig. 2.1(a). The interaction potential in Eq. (2.5.1) can be decomposed into standard and nonstandard Hubbard terms, corresponding respectively to diagonal ($ij = i'j'$) and off-diagonal ($ij \neq i'j'$) matrix elements. The Hubbard terms can be further separated into the standard Hubbard on-site interaction term $V_{iiii} \equiv U$ (for $i = j$) and the *extended* Hubbard term $V_{ijij} \equiv \overline{U}$ (for $i \neq j$) [43], respectively defined as

$$U = \int \Psi_L^2(x)V(x-y)\Psi_L^2(y)\,dx\,dy\,, \tag{2.5.2a}$$

$$\overline{U} = \int \Psi_L^2(x)V(x-y)\Psi_R^2(y)\,dx\,dy\,. \tag{2.5.2b}$$

Similarly, the nonstandard Hubbard terms can be separated into the DT (Ω_1) and PT (Ω_2) terms, with amplitudes respectively given by

$$\Omega_1 = \int \Psi_L^2(x)\Psi_L(y)V(x-y)\Psi_R(y)\,dx\,dy\,, \tag{2.5.3a}$$

$$\Omega_2 = \int \Psi_L(x)\Psi_L(y)V(x-y)\Psi_R(x)\Psi_R(y)\,dx\,dy\,. \tag{2.5.3b}$$

The physical interpretation of these terms is evident: the DT term (Ω_1) represents a single-particle hopping (e.g., $\Psi_{LL} \to \Psi_{LR}$) caused by the interaction with the nontunneling particle, while the PT term (Ω_2) describes the direct (e.g., $\Psi_{LL} \to \Psi_{RR}$) and exchange (e.g., $\Psi_{LR} \to \Psi_{RL}$) two-particle hopping. In a double-well potential, the DT term in Eq. (2.5.3a) can always be added to the single-particle tunneling, resulting in an effective tunneling $\Omega_{eff} \equiv \Omega_0 + \Omega_1$ [43, 45]. Therefore, in principle, the effective tunneling can be suppressed by the interaction when $\Omega_1 = -\Omega_0$.

2.5.2 Contact interaction

For a repulsive *contact* interaction described by

$$V(x-y) = V_\delta\, \delta(x-y) > 0\,, \tag{2.5.4}$$

the DT and PT terms can be evaluated directly by substituting Eqs. (2.3.11) into Eqs. (2.5.3), obtaining

$$\Omega_1 = \Omega_0 V_\delta \int\limits_{-\infty}^{0} \left[\overline{\Phi}_0^{(1)}(x)\right]^3 \partial_E \overline{\Phi}_0^{(1)}(x)\, dx\,, \tag{2.5.5a}$$

$$\Omega_2 = 2\Omega_0^2 V_\delta \int\limits_{-\infty}^{0} \left[\overline{\Phi}_0^{(1)}(x) \partial_E \overline{\Phi}_0^{(1)}(x)\right]^2 dx\,. \tag{2.5.5b}$$

As expected, the DT term is proportional to Ω_0, while the PT term is proportional to Ω_0^2. From Eq. (2.5.5a), we notice that, if $\Omega_1/\Omega_0 < 0$, the effective tunneling coupling Ω_{eff} could be suppressed by a sufficiently large V_δ. However, comparing Eq. (2.3.12) with Eq. (2.5.5a), we can see that this suppression cannot occur for a contact interaction. Although this can be easily checked numerically, in the following we show how these results can be obtained by a careful analysis of Eq. (2.5.5a). First, let us notice that the difference between Eq. (2.5.5a) and the orthogonality expressed in Eq. (2.3.12) lies in the third power of the orbital function $\left[\overline{\Phi}_0^{(1)}(x)\right]^3$. In the latter case, the orbital function $\overline{\Phi}_0^{(1)}(0) > 0$, while the WF tail $\Omega_0 \partial_E \overline{\Phi}_0^{(1)}(x)$ changes its sign inside the integral. Since the integral of their product should be zero, both contributions should cancel each other out. On the other hand, the negative contribution to the integral in Eq. (2.5.5a) is amplified compared to the positive one, because the value of the orbital $\overline{\Phi}_0^{(1)}(x)$ decreases as $x \to 0$, where the WF tail is positive. This implies that $\Omega_1 < 0$, so that the DT term has always the same sign as Ω_0 and consequently it can only increase the effective single-particle tunneling $|\Omega_{eff}|$.

2.5.3 Long-range interaction

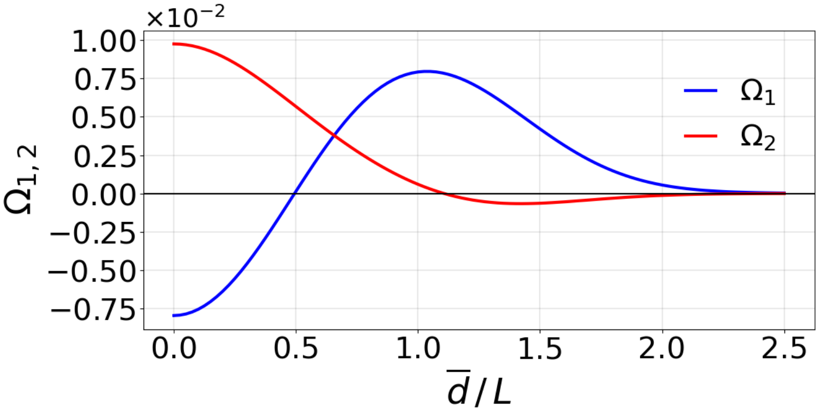

Figure 2.4: DT amplitude Ω_1 (blue curve) and PT amplitude Ω_2 (red curve) as a function of the interaction range $\overline{d}$ for a symmetric square double-well potential. Parameters: $L = 2$, $b = 0.5$, $V_0 = 5$, and $\Omega_0 = -0.22$. Interaction strength $V_\delta = 1$. Energies are given in arbitrary units, where Ω_0 sets the characteristic energy scale.

This outcome undergoes a significant transformation when considering instead of a contact interaction a *long-range* one

$$V(x-y) = \begin{cases} \overline{V} & \text{for} \quad |x-y| < \overline{d} \\ 0 & \text{elsewhere} \end{cases}, \tag{2.5.6}$$

where $\overline{d}$ denotes the interaction range. For simplicity, in the subsequent discussion we exclusively focus on this toy-model interaction, even if similar results can be obtained using a more physically realistic *screened Coulomb* interaction, as in Ref. [109]. Moreover, this toy-model allows us to study the general behavior of the nonstandard Hubbard terms as a function of the system parameters. Indeed, from Eq. (2.5.3a), we notice that Ω_1, as a function of the interaction range, becomes positive for $\overline{d} \simeq L/2$, where L is the well width. Indeed, the main contribution to the integral in Eq. (2.5.3a) comes from $x \simeq -L/2$, at the maximum of the left-orbital function. In this case,

$$\Omega_1 \propto \int_{y_1}^{y_2} \Psi_L(y)\Psi_R(y)\, dy\,,$$

where $y_{1,2} = -L/2 \mp \overline{d}$. As a result, $\Omega_1 \simeq 0$ for $\overline{d} \simeq L/2$ due to orthogonality; see Eq. (2.3.12). Subsequently, Ω_1 starts to increase for $\overline{d} \gtrsim L/2$, as the long-range interaction begins to connect the central regions of the two WFs. This qualitative argument has been tested numerically in Fig. 2.4, where the DT and PT terms (Ω_1 and Ω_2) for two distinguishable particles in a square double-well potential with long-range interaction are shown as a function of the rescaled interaction range $\overline{d}/L$. For the sake of comparison with the contact interaction in Eq. (2.5.4), in the calculations we kept $V_\delta = 2\overline{d}\,\overline{V}$ fixed. It is clear that, in this way the results for the contact interaction are obtained in the limit $\overline{d} \to 0$ and $\overline{V} \to \infty$. The amplitudes are evaluated by substituting the exact WFs of Eq. (2.2.7c) in Eqs. (2.5.3), by using the long-range potential in Eq. (2.5.6). As expected, Ω_1 undergoes a sign change for $\overline{d} \gtrsim L/2$. Given that $\Omega_0 < 0$, see Eq. (2.2.7b), the effective single-particle tunneling Ω_{eff} can be always suppressed for some finite interaction range $\overline{d} \gtrsim L/2$ and a sufficiently large interaction strength V_δ, since $\Omega_1 \propto V_\delta$.

2.5.4 Two interacting electrons with parallel spins in a square triple-well potential

In this Section, we show how PT is still possible even in the case of single-particle tunneling suppression, due to a combined action of the nonstandard Hubbard DT term and the long-range interaction. As we have discussed, the suppression of single-particle tunneling coupling in the nonstandard Hubbard model arises due to the interplay of long-range repulsive electron interaction and lattice potential. In principle, we would expect that this suppression, similarly to what happens in a flat band in twisted bilayer graphene systems [109–112], disrupts the electron transport. However, instead of being suppressed, transport can still occur via PT of localized electron pairs that are not subjected to “decay”through single-electron tunneling processes [69].

One can argue that, even in the context of the standard Hubbard model, single-electron hopping in a double-well potential is suppressed for large on-site interaction (U). For this reason, it could be challenging to distinguish this suppression from the one due to the nonstandard DT term. To avoid this issue, let us consider two electrons with parallel spins so that they cannot occupy the same well due to the Pauli principle. In this case, the contribution of the long-range electron interaction in neighboring sites, $\overline{U} \ll U$, replaces the standard on-site Hubbard term U. As a result, single-electron tunneling is not suppressed by the on-site interaction, while the DT term can still induce the suppression. Even in this scenario, similarly to the double-well case, the DT term and the single-particle tunneling term sum up to give an effective single-particle tunneling term Ω_{eff}. Therefore, if Ω_0 is exactly opposite to the DT term Ω_1, the electron pair occupying two adjacent wells becomes stable and moves coherently due to the PT term.

To show this mechanism explicitly, let us consider two electrons with parallel spins in a triple-well potential, as shown in Fig. 2.5(a). The corresponding lowest-band Hamiltonian can be written as

$$\hat{H} = \hat{H}_3 + \hat{V}\,, \tag{2.5.7}$$

where $\hat{H}_3$ is the noninteracting tight-binding tunneling Hamiltonian, given by Eq. (2.2.8), while $\hat{V}$ represents the interparticle interaction term. The noninteracting Hamiltonian can be rewritten in the second quantization formalism as

$$\hat{H}_3 = E_0 \sum_{j=1}^{3} \hat{n}_j + \Omega_0 \left(\hat{a}_L^\dagger \hat{a}_M + \hat{a}_M^\dagger \hat{a}_R + H.c. \right)\,, \tag{2.5.8}$$

where $\hat{a}_j^{(\dagger)}$ destroys (creates) an electron at site $j = 1, 2, 3 \equiv L, M, R$, $\hat{n}_j = \hat{a}_j^\dagger \hat{a}_j$ is the number operator, E_0 is the site energy, and Ω_0 is the tunneling energy given by Eq. (2.4.3). Since the Hamiltonian does not contain any spin-flip terms, the number operators $\hat{n}_j$ involve only parallel spins, so that the spin indices can be omitted.

In a similar way, the interaction operator $\hat{V}$ can be written in the second quantization formalism as

$$\hat{V} = \frac{1}{2} \sum_{i'j'ij} V_{i'j'ij} \hat{a}_{i'}^\dagger \hat{a}_{j'}^\dagger \hat{a}_j \hat{a}_i\,, \tag{2.5.9}$$

where $V_{i'j'ij}$ is obtained by substituting in Eq. (2.5.1) the triple-well WFs

$$\Psi_j(x) \equiv \langle x | \hat{a}_j^\dagger | 0 \rangle$$

given by Eqs. (2.2.9) and the long-range potential interaction of Eq. (2.5.6). Thus, considering only parallel-spin electron motion, Eq. (2.5.9) can be explicitly written as

$$\begin{aligned} \hat{V} = {} & \overline{U} \left(\hat{n}_L \hat{n}_M + \hat{n}_M \hat{n}_R \right) + \\ & + \Omega_1 \left(\hat{n}_L \hat{a}_M^\dagger \hat{a}_R + \hat{n}_R \hat{a}_M^\dagger \hat{a}_L + H.c. \right) + \\ & - \Omega_2 \left(\hat{n}_M \hat{a}_L^\dagger \hat{a}_R + \hat{n}_M \hat{a}_R^\dagger \hat{a}_L \right)\,, \end{aligned} \tag{2.5.10}$$

where $\overline{U}$ represents the nearest neighbor interaction term, obtained in the triple-well case by replacing $\Psi_R(x)$ with $\Psi_M(x)$ in Eq. (2.5.2b), so that

$$\overline{U} = \int \Psi_L^2(x) V(x-y) \Psi_M^2(y)\, dx\, dy\,, \tag{2.5.11}$$

while the last two terms describe respectively the DT and PT processes, with amplitudes given by

$$\Omega_1 = \int \Psi_L^2(x)\Psi_M(y)V(x-y)\Psi_R(y)\,dx\,dy\,, \tag{2.5.12a}$$

$$\Omega_2 = \int \Psi_L(x)\Psi_M(x)V(x-y)\Psi_M(y)\Psi_R(y)\,dx\,dy\,, \tag{2.5.12b}$$

where

$$\Omega_1 \equiv \Omega_1^{M\to R} = \Omega_1^{M\to L}$$

and

$$\Omega_2 \equiv \Omega_2^{L\to M, M\to R} = \Omega_2^{R\to M, M\to L}\,.$$

Notice that, in our calculations, we have chosen the interaction range $\bar{d}$ in Eq. (2.5.6) so that the contribution from the next-to-nearest neighbor term can be neglected. In this way, the total Hamiltonian in Eq. (2.5.7) represents the *nonstandard* Hubbard model, whereas the *extended* Hubbard model arises simply by setting $\Omega_1 = \Omega_2 = 0$ in Eq. (2.5.10). Finally, we observe that, in the presence of long-range interaction, the DT term Ω_1 changes its sign depending on the interaction range, as illustrated in Fig. 2.4 for the double-well system (for the triple-well case, see Fig. A.1 in Appendix A).

2.5.5 Quantum dynamics of two interacting electrons with parallel spins in a square triple-well potential

The effectiveness of our approach can be tested directly by studying the system's quantum dynamics. In particular, let us consider as initial condition two electrons occupying two neighboring wells $\bar{j}$ and $\bar{j}'$. Their time-dependent wave function can always be written as

$$|\Psi^{(\bar{j}\,\bar{j}')}(t)\rangle = \sum_{j<j'} b_{jj'}^{(\bar{j}\,\bar{j}')}(t)\,\hat{a}_j^\dagger \hat{a}_{j'}^\dagger\,|0\rangle\;, \tag{2.5.13}$$

where $j, j' = L, M, R$, while the upper indices $(\bar{j}\,\bar{j}')$ label the initial state. Specifically, let us choose $\bar{j} = L$ and $\bar{j}' = M$, so that the left and middle wells are initially occupied. Then, Eq. (2.5.13) can be explicitly written as

$$|\Psi^{(LM)}(t)\rangle = \left[b_{LM}^{(LM)}(t)\,\hat{a}_L^\dagger\hat{a}_M^\dagger + b_{LR}^{(LM)}(t)\,\hat{a}_L^\dagger\hat{a}_R^\dagger + b_{MR}^{(LM)}(t)\,\hat{a}_M^\dagger\hat{a}_R^\dagger\right]|0\rangle\;. \tag{2.5.14}$$

By substituting Eq. (2.5.14) into the time-dependent Schrödinger equation

$$i\partial_t\,|\Psi^{(\bar{j}\,\bar{j}')}(t)\rangle = \left(\hat{H}_3 + \hat{V}\right)|\Psi^{(\bar{j}\,\bar{j}')}(t)\rangle\;, \tag{2.5.15}$$

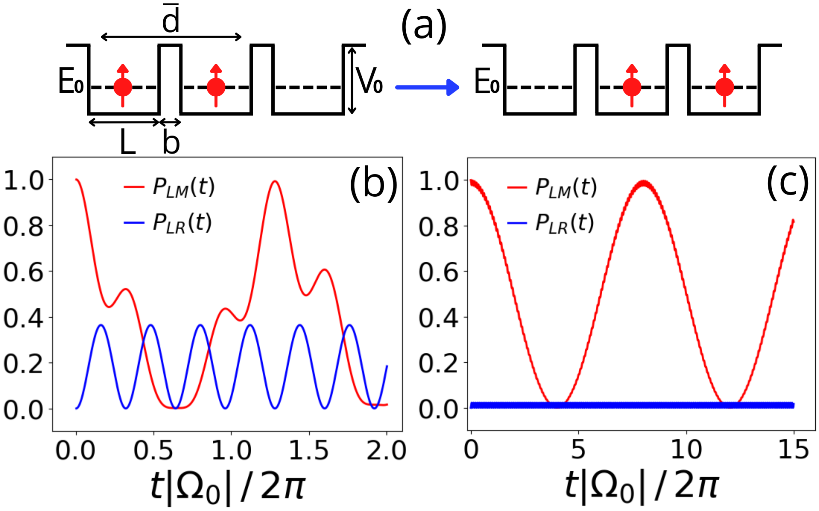

Figure 2.5: (a) Coherent motion of two interacting electrons with parallel spins in a symmetric square triple-well potential, corresponding to the PT process. Black dashed lines correspond to the single-site ground state energy E_0, while $\overline{d}$ is the interaction range. (b) Occupancy probabilities $P_{LM}(t)$ (red curve) and $P_{LR}(t)$ (blue curve) for $L = 2$, $b = 0.5$, $V_0 = 5$, and $\Omega_0 \simeq -0.22$. (c) Occupancy probabilities $P_{LM}(t)$ (red curve) and $P_{LR}(t)$ (blue curve) for $L = 4$, $b = 1$, $V_0 = 5$, and $\Omega_0 \simeq -0.0167$. Interaction strength $V_\delta = 3$ and interaction range $\overline{d}/L = 2$, so that $\overline{U} \simeq 0.35$, $\Omega_1 \simeq 0.0125$, and $\Omega_2 \simeq 0.0012$ in (b) and $\overline{U} \simeq 0.19$, $\Omega_1 \simeq 0.0027$, and $\Omega_2 \simeq -6.4 \cdot 10^{-6}$ in (c). Energies are given in arbitrary units, where Ω_0 sets the characteristic energy scale.

we obtain the following equations of motion:

$$
\begin{aligned}
i\dot{b}_{LM}^{(LM)}(t) &= \left(2E_0 + \overline{U}\right) b_{LM}^{(LM)}(t) + \left(\Omega_0 + \Omega_1\right) b_{LR}^{(LM)}(t) + \Omega_2 b_{MR}^{(LM)}(t)\,,\\
i\dot{b}_{LR}^{(LM)}(t) &= 2E_0 b_{LR}^{(LM)}(t) + \left(\Omega_0 + \Omega_1\right) \left[b_{LM}^{(LM)}(t) + b_{MR}^{(LM)}(t)\right]\,,\\
i\dot{b}_{MR}^{(LM)}(t) &= \left(2E_0 + \overline{U}\right) b_{MR}^{(LM)}(t) + \left(\Omega_0 + \Omega_1\right) b_{LR}^{(LM)}(t) + \Omega_2 b_{LM}^{(LM)}(t)\,.
\end{aligned}
\tag{2.5.16}
$$

Looking at Eqs. (2.5.16), we notice that the DT term Ω_1 appears only together with the single-particle tunneling Ω_0, thus giving rise to an effective single-particle tunneling $\Omega_{eff} = \Omega_0 + \Omega_1$ [43–45]. Equations (2.5.16) can be integrated numerically to obtain the occupancy probabilities for all sites of the triple-well system as a function of time. Specifically, the probability to find the two electrons in the wells j, j' is defined as

$$\begin{aligned} P_{jj'}(t) &= \langle \Psi^{(LM)}(t) | \, \hat{n}_j \hat{n}_{j'} \, | \Psi^{(LM)}(t) \rangle = \\ &= \left| b^{(LM)}_{jj'}(t) - b^{(LM)}_{j'j}(t) \right|^2 , \end{aligned} \tag{2.5.17}$$

while the probability to find one electron occupying the well j is defined as

$$P_j(t) = \sum_{j' \neq j} \left| b^{(LM)}_{jj'}(t) \right|^2 . \tag{2.5.18}$$

In Figs. 2.5(b) and 2.5(c), we show the probabilities $P_{LM}(t)$ and $P_{LR}(t)$, derived from Eq. (2.5.17), for two different geometries of the triple-well system at some fixed interparticle interaction strength. Particularly, in Fig. 2.5(c), we adjust the geometry of the system (by enlarging the well and barrier widths) to produce a significant suppression of $P_{LR}(t)$, if compared with that in Fig. 2.5(b). This suppression suggests the emergence of a propagating correlated electron pair within the system, showing that single-particle tunneling can be suppressed induced by modifying the well parameters. Note that a similar suppression is also observable within the extended Hubbard model framework. Specifically, it is easy to show that the suppression of $P_{LR}(t)$ in the extended Hubbard model occurs when $\overline{U} \gg \Omega_0$ (for further details, see Appendix C).

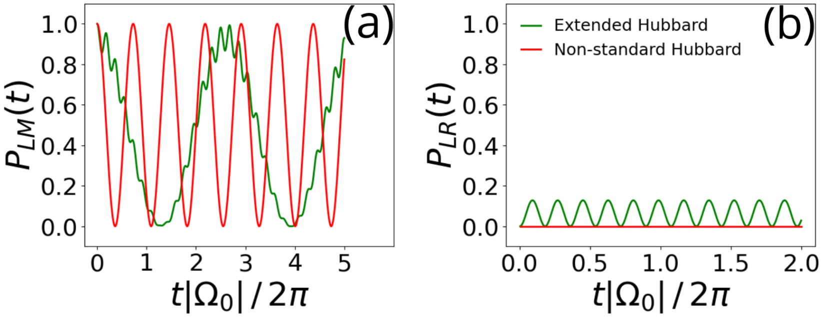

Figure 2.6: (a) Occupancy probabilities $P_{LM}(t)$ and (b) occupancy probabilities $P_{LR}(t)$ obtained with the nonstandard Hubbard model (red curves) and the extended Hubbard model (green curves), for the case of complete single-particle tunneling suppression. Parameters: $L = 2$, $b = 0.1$, $V_0 = 1.1$ and $\Omega_0 \simeq -0.32$. Interaction strength $V_\delta = 22$ and interaction range $\overline{d}/L = 2$, so that $\overline{U} \simeq 1.54$, $\Omega_1 \simeq -\Omega_0$ and $\Omega_2 \simeq 0.22$. Energies are given in arbitrary units, where Ω_0 sets the characteristic energy scale.

Clearly, the nonstandard and extended Hubbard models diverge significantly when complete suppression of single-particle tunneling occurs, i.e., for $\Omega_1 = -\Omega_0$. To show this explicitly, we adjust the geometry of the system and the interaction strength to achieve complete suppression of single-particle tunneling Ω_{eff}. Results are shown in Fig. 2.6 for both nonstandard (red curves) and extended (green curves) Hubbard models. As one can see, notable distinctions between the two models' predictions exist. Specifically, the extended Hubbard model predicts a small, but not zero, amplitude for $P_{LR}(t)$ [see Fig. 2.6(b)], as well as a smaller oscillation frequency of $P_{LM}(t)$ compared to the nonstandard Hubbard model [see Fig. 2.6(a)]. Given that in the nonstandard Hubbard model the single particle tunneling is suppressed, the enhanced transport efficiency, signaled by the high frequency of oscillations of $P_{LM}(t)$, is due to the presence of the PT term.

Finally, one may wonder what is the region of parameters in which the nonstandard and extended Hubbard models give approximately similar outcomes. Within the validity of the SB approximation, a glance at Eq. (2.5.16) reveals that the two Hubbard models are expected to give close results when the Ω_1 and Ω_2 terms become negligible compared to Ω_0, namely for sufficiently weak interaction strength. A detailed comparison between the two Hubbard models, as well as a comparison with our analytical approach, is reported in Appendix C.

2.6 Discussion

In conclusion, we have explored the conditions ruling the suppression of single-particle tunneling coupling in periodic systems, within the framework of a nonstandard Hubbard model, including density-induced tunneling and pair tunneling terms. Our findings demonstrate that such suppression cannot occur with a conventional contact repulsive interaction, but only in the presence of a long-range repulsive interaction. A better understanding of the mechanism underlying the suppression of the single-particle tunneling could be a significant issue in the theory of quantum transport in correlated systems. Indeed, as we have shown here, see Fig. (2.6), in the presence of single-particle tunneling suppression the dynamics is dominated by pair tunneling, which enhances the transport efficiency.

The consequences of these effects are far reaching, since single-particle tunneling suppression and pair tunneling dominated dynamics may lead to transport regimes characterized by efficient and robust electron pair transport. Indeed, within the nonstandard Hubbard model considered here, increasing the interaction strength not only suppresses single-particle tunneling but also enhances pair tunneling, introducing a competition between these two effects. Such interplay may lead to nontrivial transport regimes that could potentially expand the paradigm of Mott-insulator transitions [113] beyond the standard Hubbard model. In the future, we plan to investigate the impact of the effects shown in this manuscript in lattice models of different dimensions.

Chapter 3

Many-body tunneling in a double-well potential

This chapter is an adaptation of the article [51], accepted for publication.

In this Chapter, we present a novel approach for evaluating Wannier functions (WFs), offering a new perspective on their role in many-body systems. Unlike traditional methods, such as the maximally localized Wannier functions (MLWFs) approach, which focuses on minimizing the function tails, our approach emphasizes these tails.

Using perturbative analytical approximations and extensive numerical simulations on an exactly solvable model, we address nonstandard Hubbard terms and demonstrate their critical influence on many-body dynamics. Specifically, we study tunneling dynamics in arbitrary double-well potentials, moving beyond the standard Hubbard model to include nonstandard terms such as density-induced tunneling (DT) and pair tunneling (PT). Our results reveal that these terms significantly modify the dynamics predicted by the standard Hubbard model: DT modifies the single-particle tunneling parameter Ω_0, while PT enables coherent propagation not captured by the standard model.

We show that the discrepancies between the standard and nonstandard Hubbard models grow with increasing interaction strength, potentially leading to novel transport behaviors. However, at lower interaction strengths, both models converge, as nonstandard terms become negligible. These findings have important implications for phenomena like superconductivity in twisted bilayer graphene and metal-insulator transitions.

Our model aligns well with numerical simulations of lowest-band parameters and is strongly supported by experimental observations of second-order atom tunneling in optical double-well potentials. This strong agreement with experimental data highlights the accuracy and potential of our approach in providing a more comprehensive framework for describing complex many-body systems than the standard Hubbard model.

After recalling the two-potential approach (TPA) as discussed in Ch. 2, we accurately define the WFs of a double-well potential in Sec. 3.3. In Sec. 3.4, we analyse the nonstandard Hubbard model, evaluating the corresponding nonstandard Hubbard terms through the TPA for a contact interaction in Sec. 3.5. We compare the results with existing theoretical literature in Sec. 3.6. Finally, in Sec. 3.7, we examine the effects of DT and PT terms on the dynamics of two distinguishable particles in a square double-well potential. Our findings are compared with experimental observations in Sec. 3.8, highlighting the regimes where nonstandard DT and PT terms are particularly relevant.

3.1 Nonstandard Hubbard models

3.1.1 Nonstandard Hubbard terms and the Wannier functions

In the field of condensed matter physics, the Hubbard model [39–42] serves as a foundational paradigm, crucial for understanding the behavior of various solid-state systems, especially those exhibiting strong electron correlations [43]. This model is characterized by a tight-binding Hamiltonian featuring single-particle tunneling energy (Ω_0) allowing for hopping between neighboring sites, and an on-site two-particle interaction energy (U), which can be either attractive ($U < 0$) or repulsive ($U > 0$). Despite its apparent simplicity, the Hubbard model is widely believed to be instrumental in addressing the unresolved issues of high-T_C superconductivity [12–29] and strongly correlated electron systems [3–11]. However, questions have emerged regarding the model's effectiveness and empirical validation, especially in the context of interacting particles ($U \neq 0$). In fact, in the noninteracting limit, the tunneling energy Ω_0 accurately describes single-particle and noninteracting many-body dynamics. However, in interacting systems, the standard Hubbard model often fails to fully capture the effects induced by interparticle interactions [43–47]. Specifically, crucial additional terms such as *density-induced tunneling* and *pair tunneling* are often neglected, limiting the model's accuracy in describing real-world systems [43, 50, 52–57].

Recent research has therefore focused on extending the Hubbard model to include these additional interaction terms, leading to what are known as nonstandard

Hubbard models [43, 45, 70, 96–101]. Specifically, when interactions between different sites of a lattice are incorporated, we refer to the *extended* Hubbard model. Besides this, the DT term accounts for modifications of single-particle tunneling energy Ω_0 due to the effective mean field created by other particles in the system, often referred to as *bond-charge interaction* [43–45, 58–67]. On the other hand, the PT term, analogous to Cooper pair tunneling, plays a crucial role in the two-particle elastic tunneling, representing a coherent process [54, 68].

Previous studies typically describe *cotunneling* within the framework of the standard Hubbard Hamiltonian [2, 48, 49], where it manifests as a second-order process in Ω_0, generated by two virtual sequential single-particle tunnelings. Each tunneling step is characterized by a large interaction energy $|U| \gg \Omega_0$, resulting in an $\mathcal{O}(\Omega_0^2/|U|)$ cotunneling frequency [2]. However, the standard Hubbard model does not fully capture all relevant physical processes in interacting many-body systems. To address these limitations, different extensions to the standard Hubbard model have been investigated in Refs. [70–83], incorporating DT and PT as nonstandard processes. These studies have highlighted the crucial influence of these nonstandard Hubbard terms on the behavior of strongly correlated systems. However, it is only in recent years that nonstandard Hubbard models have attracted significant attention, particularly in the context of ultracold atoms in optical lattices, where the DT phenomenon has been experimentally observed [43, 45, 82, 86–95].

Despite these advances, fully understanding the impact of nonstandard terms on the dynamics of correlated systems remains challenging [1, 43, 70]. In particular, the magnitude of these terms is intricately linked to the overlap of WFs between neighboring wells [50, 52, 84]. Current approximations often fail to account for the tails of these functions, which are crucial for determining the value and sign of nonstandard interaction matrix elements. State-of-the-art approaches to WF construction, such as the theory of MLWFs [85], involve an iterative procedure to minimize the spread of WFs, making them as localized as possible in real space. While highly effective for many applications, such as the study of electronic structure in crystalline solids, transport properties, and entanglement in condensed matter systems, MLWFs' approach often neglects the long tails of the WFs, which are essential for accurately capturing the nonstandard Hubbard terms. Therefore, a consistent approximation for the WFs spanning the entire double-well region is essential for a deeper understanding of the intricate interplay between interaction and tunneling dynamics in quantum systems.

To address these limitations, we propose a novel method for evaluating WFs that spans the entire double-well region, offering a more consistent approximation. This method includes the nonstandard terms in the standard

Hubbard Hamiltonian, thus reconsidering the two-particle tunneling process. Our analysis suggests that the coherent PT amplitude remains significant even when U is large, potentially dominating the cotunneling process under specific system's parameters and interaction strengths [53]. Therefore, in addition to the standard Hubbard model, we introduce a single-band (SB) nonstandard model that exactly accounts for all interaction effects, still neglecting the effects of higher energy bands. Furthermore, we evaluate the system's dynamics using a multiband (MB) nonstandard model, which includes both the nonstandard Hubbard terms and the effects of higher energy bands in the Hubbard Hamiltonian.

3.2 Theoretical and experimental double-well potentials

After proposing our novel method for the evaluation of the WFs, it is essential to discuss the specific systems and models where this approach is applied. Our analysis mainly focuses on two different potentials: a square double-well potential and a sinusoidal potential. These models provide valuable insights into the dynamics of strongly correlated systems, with each model serving a different role in theoretical and experimental analysis.

Specifically, the square double-well potential is a toy-model, providing a simplified yet effective framework for understanding the main aspects of tunneling interacting dynamics, see Ch. 2. This model allows us also to explore the basic principles without the complexities introduced by more realistic potentials. Our analytical approximated results for this model exhibit excellent agreement with our numerical simulations, demonstrating the consistency, validity and reliability of our approach.

On the other hand, the sinusoidal potential represents a more realistic model that closely mimics experimental conditions, particularly in systems such as optical lattices. Our model's predictions for the sinusoidal potential show excellent agreement with experimental data in Ref. [2]. Specifically, compared to the standard Hubbard model and the SB nonstandard model, the MB nonstandard model, which incorporates the nonstandard Hubbard terms and the effects of higher energy bands in the Hubbard Hamiltonian, provides a more accurate alignment with experimental results. The MB nonstandard model effectively describes the two-particle tunneling process, both for weakly and strongly interacting regimes, emerging as the most accurate representation of experimental observations.

In general, the nonstandard Hubbard model diverges significantly from the standard Hubbard model as the interaction strength increases, leading to different transport regimes. In the nonstandard model, strong interactions modify single-particle tunneling while enhancing PT, creating an interplay between these effects and potentially leading to new transport phenomena beyond the metal-insulator transitions [102–104]. However, at lower interaction strengths, both models yield similar results, particularly when DT and PT terms are negligible compared to Ω_0.

Finally, our approach allows for further modifications to the potential shape, enhancing its flexibility and applicability. Specifically, we adapt our method to obtain analytical approximated results for a squared cosine potential, that exhibit excellent agreement with established theoretical results available in the literature, see Ref. [1].

In summary, our model's ability to consistently approximate WFs across the entire double-well region and its successful application to both toy and realistic potentials underscore its robustness and versatility. The strong correlation between our analytical approximated, numerical, and experimental results confirms that our method provides a comprehensive and accurate description of tunneling dynamics and interactions in quantum systems.

3.3 Two-potential approach and Wannier functions for a double-well potential

In this Section, we employ an analytical approach, see Ch. 2, for the evaluation of the WFs within the framework of a symmetric square double-well potential. It is based on the modification of the orbital wave functions (hereinafter orbitals), by incorporating their extensions into neighboring sites. It derives from the two-potential approach (TPA) to tunneling problems, initially developed for tunneling to the continuum [105–107, 114], and it has been adapted to compute the discrete eigenspectrum of a multiwell system. The corresponding set of eigenstates, obtained from the modified orbitals, is used to determine the WFs through a proper unitary transformation. Consequently, this approach avoids the ambiguities associated with approaches based on the continuous Bloch-function spectrum [85].

3.3.1 Generic symmetric double-well potential

For simplicity, we start presenting our method for a generic symmetric double-well potential, although the method can straightforwardly be extended to multiwell systems to validate its accuracy. We then compare our results for the WFs with the orbitals and the exact solutions of the Schrödinger equation for the case of two distinguishable particles. Finally, the resulting WFs can be exploited to correctly evaluate the DT and PT terms of the nonstandard Hubbard Hamiltonian.

Initially, consider a particle placed in a generic 1D double-well potential formed by two single-well potentials $\mathcal{V}_{1,2}(x)$, separated by a potential barrier. To simplify the analytical treatment, we assume a symmetric double-well potential, even if the procedure can be easily extended to generic asymmetric potentials. The single-well potentials are defined such that

$$\mathcal{V}_1(x) = \mathcal{V}_2(-x)$$

for $x > x_0$, and

$$\mathcal{V}_{1,2}(x_0) = const\,.$$

It is important to note that this procedure differs significantly from the widely used Wigner R-matrix theory (see Ref. [115]), in which the single-well potential is truncated, and an infinite potential barrier is placed beyond the separation point.

By choosing the energy scale such that $\mathcal{V}(x_0) = 0$, we can express the potential as

$$\mathcal{V}(x) = \mathcal{V}_1(x) + \mathcal{V}_2(x)\,, \tag{3.3.1}$$

as shown in Fig. 3.1 for $x_0 = 0$. If $\mathcal{V}(x_0) \neq 0$, then $\mathcal{V}(x_0)$ must be subtracted in Eq. (3.3.1) (see Ref. [106]). Importantly, the final result is independent on the chosen energy scale. A similar construction for single-well potentials can be applied to the extension of the TPA to the multidimensional case, see Ref. [114], where the separation point is replaced by a separation surface, beyond which the corresponding single-well potential becomes constant.

To simplify our analysis and in close analogy with the Hubbard model, we employ the SB approximation, by focusing on the lowest energy band and neglecting all the others, as well as the continuous spectrum ($E \geq 0$). We then assume that the two lowest bound states of the system (with energy $\mathcal{E}_{1,2} < 0$) create a band, well separated from the others. The eigenstates belonging to this band, namely

$$\psi_{1,2}(x) = \langle x|\psi_{1,2}\rangle\ ,$$

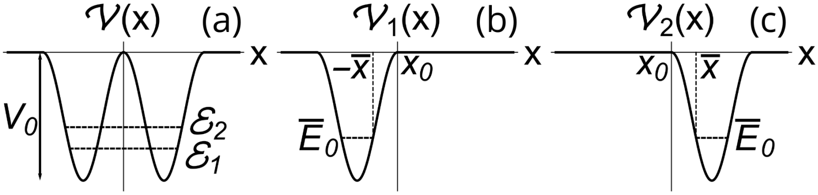

Figure 3.1: (a) Symmetric double-well potential $\mathcal{V}(x)$, given by the sum of two single-well potentials, with lattice depth V_0. Dashed lines represent the two lowest-band eigenstates of the system $\mathcal{E}_{1,2}$. (b), (c) Left and right single-well potentials $\mathcal{V}_{1,2}(x)$, where $\mp\overline{x}$ are the classical turning points, so that $\mathcal{V}_{1,2}(\mp\overline{x}) = \overline{E}_0$, and x_0 is the separation point. Each of the single-well potentials vanishes beyond the separation point ($x_0 = 0$), defined so that $\mathcal{V}_1(x_0) = \mathcal{V}_2(x_0) = 0$. Each of the single-well potentials contains one bound state with energy $\overline{E}_0 < 0$.

are obtained from the exact solution of the Schrödinger equation

$$\mathcal{H}\,|\psi_{1,2}\rangle \equiv (\mathcal{K} + \mathcal{V}(x))\,|\psi_{1,2}\rangle = \mathcal{E}_{1,2}\,|\psi_{1,2}\rangle\ , \tag{3.3.2}$$

where

$$\mathcal{K} = -\nabla_x^2$$

is the kinetic term, and $\mathcal{V}(x)$ the double-well potential in Eq. (3.3.1) (to simplify the notation, we use dimensionless units, i.e. $\hbar = 2m = 1$, unless otherwise specified).

The tight-binding tunneling Hamiltonian H describing this lowest band is given by

$$H = \overline{E}_0 \sum_{j=1}^{2} |\Psi_j\rangle\langle\Psi_j| + \overline{\Omega}_0\left(|\Psi_1\rangle\langle\Psi_2| + H.c.\right)\ , \tag{3.3.3}$$

where $\overline{E}_0$ is the single-well energy, see Fig. 3.1, $\overline{\Omega}_0$ is the nearest neighbor tunneling coupling, while

$$\Psi_j(x) = \langle x|\Psi_j\rangle$$

is the j-th well WF. The site energies $\overline{E}_0$ and the WFs $\Psi_j(x)$ can be obtained by diagonalizing the tunneling Hamiltonian in Eq. (3.3.3). By identifying the eigenvalues and the eigenstates of the tunneling Hamiltonian in Eq. (3.3.3) respectively with the exact energies $\mathcal{E}_{1,2}$ and wave functions $|\psi_{1,2}\rangle$ of the double-well system obtained from Eqs. (3.3.2), we can write

$$\overline{E}_0 = (\mathcal{E}_1 + \mathcal{E}_2)/2\,, \tag{3.3.4a}$$

$$\overline{\Omega}_0 = (\mathcal{E}_1 - \mathcal{E}_2)/2\,, \tag{3.3.4b}$$

$$\Psi_{L,R}(x) = \frac{1}{\sqrt{2}}\left[\psi_1(x) \pm \psi_2(x)\right]\,, \tag{3.3.4c}$$

where $\overline{E}_0$ and $\overline{\Omega}_0$ are the tunneling Hamiltonian parameters, while

$$\Psi_{L,R}(x) = \langle x|\hat{a}^\dagger_{1,2}|0\rangle$$

are the WFs, where $\hat{a}^\dagger_{L,R}$ are the creation operators for the left and right well, respectively.

In the multiwell limit, the previous procedure resembles the standard one for constructing WFs from the continuous spectrum of Bloch functions under periodic boundary conditions. In that case, due to the phase indeterminacy [85], the resulting WFs are not uniquely defined. In contrast, we impose the boundary conditions

$$\psi_{1,2}(x) \sim e^{-\sqrt{-\mathcal{E}_{1,2}}|x|}$$

for $x \to \pm\infty$ on the eigenstates $\psi_{1,2}(x)$ belonging to the first band. This ensures that the solution to the Schrödinger equation (3.3.2) is uniquely defined for both the energies $\mathcal{E}_{1,2}$.

3.3.2 The modified orbitals

Typically, determining the spectrum of an arbitrary double-well potential system involves exact numerical diagonalization. Consequently, many studies use an approximate form for the WFs $\Psi_{L,R}(x)$. In contrast, we evaluate the WFs by modifying in a perturbative way the single-well orbitals. To do so, we define the left- and right-well orbitals as

$$\Phi_0^{(1,2)}(x) \equiv \Phi_0^{(1,2)}(E_0, x)\,,$$

where E_0 is the ground state energy of the single-well potential. Therefore, the orbitals $\Phi_0^{(1,2)}(x)$ are respectively the ground states of the left- and right-well Hamiltonian

$$H_{1,2}\Phi_0^{(1,2)}(x) = E_0\Phi_0^{(1,2)}(x)\,, \tag{3.3.5}$$

where

$$H_{1,2} = \mathcal{K} + \mathcal{V}_{1,2}(x)$$

are the Hamiltonians of the left and right well, respectively. Note that

$$\Phi_0^{(2)}(x) = \Phi_0^{(1)}(-x)$$

due to the symmetry of the double-well system. Since each potential $\mathcal{V}_{1,2}(x)$ exactly vanishes beyond the separation point $x_0 = 0$ (see Fig. 3.1), the orbitals can be written as

$$\Phi_0^{(1)}(x) = \Phi_0^{(1)}(0)e^{-q_0 x} \qquad \text{for } x \geq 0\,, \tag{3.3.6a}$$

$$\Phi_0^{(2)}(x) = \Phi_0^{(2)}(0)e^{q_0 x} \qquad \text{for } x \leq 0\,, \tag{3.3.6b}$$

where

$$q_0 = \sqrt{-E_0}\,.$$

Since $\mathcal{V}_{1,2}(x) \to 0$ in the limit $x \to \pm\infty$, the solution of the Schrödinger equation within the potential barrier ($E < 0$) is a combination of two functions $\sim e^{\pm q_0 x}$. Disregarding the growing solution as unphysical, the decreasing one uniquely establishes the allowed discrete energy levels. Conversely, beyond the potential barrier ($E \geq 0$), the exponential factor q_0 becomes imaginary, indicating the presence of both the solutions and a resulting continuous spectrum.

As said, our approach consists in using the orbitals $\Phi_0^{(1,2)}(x)$ as a basis for constructing the eigenstates and the corresponding WFs in a perturbative way. A possible approach would be to consider the left-well orbital $\Phi_0^{(1)}(x)$ as an unperturbed eigenstate of the Hamiltonian H_1, and the right-well potential $\mathcal{V}_2(x)$ as the perturbation (or vice versa). However, this approach would lack a perturbative expansion parameter. In contrast, the problem can be solved using the TPA method, by employing the overlap

$$\beta \equiv \langle \Phi_0^{(1)} | \Phi_0^{(2)} \rangle$$

as a perturbative expansion parameter. We note that β can be considered as a small parameter, since it is of the order of the barrier penetration coefficient

$$T_0 = \exp\left(- \int_{-\overline{x}}^{\overline{x}} |q(x')|\, dx' \right) \ll 1,$$

where $q(x)$ is the (imaginary) momentum under the barrier and $\pm\,\overline{x}$ are the classical turning points, indicated in Fig. 3.1. Using this approach, we obtain for the tunneling Hamiltonian parameters in Eq. (3.3.4a) and Eq. (3.3.4b):

$$\overline{E}_0 = E_0 + \mathcal{O}(\beta^2)\,, \tag{3.3.7a}$$

$$\overline{\Omega}_0 = \Omega_0 + \mathcal{O}(\beta^2)\,, \tag{3.3.7b}$$

where the site energy E_0 is given by Eqs. (3.3.5). Similarly,

$$\mathcal{E}_{1,2} = E_\pm + \mathcal{O}(\beta^2)\,,$$

where

$$E_\pm = E_0 \pm \Omega_0\,.$$

Thus, the parameters of the tunneling Hamiltonian in Eq. (3.3.3) are completely determined by the single-well orbitals in Eqs. (3.3.5). Specifically, the tunneling coupling Ω_0 is defined as

$$\Omega_0 = \langle \Phi_0^{(1)} | \mathcal{V}_2 | \Phi_0^{(2)} \rangle = \langle \Phi_0^{(1)} | \mathcal{V}_1 | \Phi_0^{(2)} \rangle\ . \tag{3.3.8}$$

Note that Ω_0 is proportional to the barrier tunneling penetration coefficient T_0, making it a small parameter in the corresponding perturbative expansion of the eigenenergies. From Eq. (3.3.8), it follows that Ω_0 is always negative, since the orbitals $\Phi_0^{(1,2)}(x)$ correspond to the ground states of the respective wells (and their product is positive), while the potentials $\mathcal{V}_{1,2}(x) < 0$, as shown in Fig. 3.1. From the Schrödinger equation, Eq. (3.3.8) can be rewritten as

$$\Omega_0 = \Phi_0^{(1)\prime}(0)\Phi_0^{(2)}(0) - \Phi_0^{(1)}(0)\Phi_0^{(2)\prime}(0)\,. \tag{3.3.9}$$

From Eqs. (3.3.6), we can evaluate the derivative of the orbitals at the separation point $x_0 = 0$:

$$\Phi_0^{(1)\prime}(0) = -\sqrt{|E_0|}\Phi_0^{(1)}(0)\,, \tag{3.3.10a}$$

$$\Phi_0^{(2)\prime}(0) = \sqrt{|E_0|}\Phi_0^{(2)}(0)\,. \tag{3.3.10b}$$

By substituting Eqs. (3.3.10) into Eq. (3.3.9), we derive the tunneling energy Ω_0, given by

$$\Omega_0 = -2\sqrt{|E_0|}\Phi_0^{(1)}(0)\Phi_0^{(2)}(0)\,, \tag{3.3.11}$$

which represents a product of neighboring orbitals evaluated at the separation point. Examining Eq. (3.3.11), we observe that $\Omega_0 \propto T_0$ serves as a simplified (1D) version of the well-known Bardeen formula [108].

As discussed in Ch. 2, the eigenstates

$$\psi_\pm(x) \equiv \psi_{1,2}(E_\pm, x)$$

cannot be obtained from Eq. (3.3.4c) by replacing the WFs $\Psi_{L,R}(x)$ with the corresponding orbitals $\Phi_0^{(1,2)}(x)$ in Eqs. (3.3.5). In fact, by doing that, an inconsistency between the energy arguments of the double-well wave functions $\psi_\pm(x)$ and the single-well orbitals $\Phi_0^{(1,2)}(x)$ arises. To overcome this problem, we introduce an energy shift $(E_\pm - E_0)$ in the orbitals by replacing the ground state energy E_0 with a free parameter $E < 0$. The resulting modified orbitals

$$\overline{\Phi}^{(1,2)}(E,x) \equiv \Phi_0^{(1,2)}(E_0 \to E, x)$$

(normalized to unity) are obtained from Eqs. (3.3.5) by imposing the boundary conditions

$$\overline{\Phi}^{(1,2)}(E, x \to \mp\infty) \propto e^{\pm qx} \,,$$

where $q = \sqrt{-E}$ (compare with Eqs. (3.3.6)). These boundary conditions uniquely define the modified orbitals for any energy value E. Unlike $\Phi_0^{(1,2)}(x)$, the modified orbitals $\overline{\Phi}^{(1,2)}(E,x)$ asymptotically diverge for any $E \neq E_0$. Thus, we define them on two different segments, respectively $\mathcal{X}_1 = (-\infty, 0)$ and $\mathcal{X}_2 = (0, \infty)$, vanishing elsewhere. As a result, they are *nonoverlapping*, and therefore *orthogonal*. The eigenenergies $E = E_\pm$ are determined by enforcing continuity conditions at the separation point $(x_0 = 0)$. The corresponding eigenstates, $\psi_\pm(x)$, are expressed in terms of the modified orbitals $\overline{\Phi}^{(1,2)}(E,x)$, which are defined within the segment of the j-th well $(j = 1, 2)$, as follows:

$$\psi_\pm(x) = \frac{1}{\sqrt{2}} \left[\overline{\Phi}^{(1)}(E_\pm, x) \pm \overline{\Phi}^{(2)}(E_\pm, x) \right] . \tag{3.3.12}$$

This approach constructs the exact eigenspectrum, $\mathcal{E}_{1,2} \equiv E_\pm$ and $\psi_{1,2}(x) \equiv \psi_\pm(E_\pm, x)$, by using the modified orbitals for different segments and imposing continuity at the separation point $(x_0 = 0)$. This method represents the standard procedure for solving the Schrödinger equation (3.3.2). The resulting WFs, given by Eqs. (3.3.4c), are expressed as

$$\begin{aligned} \Psi_{L,R}(x) &= \frac{1}{\sqrt{2}} \left[\psi_+(E_+, x) \pm \psi_-(E_-, x) \right] = \\ &= \frac{1}{2} \left[\overline{\Phi}^{(1)}(E_+, x) + \overline{\Phi}^{(2)}(E_+, x) \right] + \\ &\pm \frac{1}{2} \left[\overline{\Phi}^{(1)}(E_-, x) - \overline{\Phi}^{(2)}(E_-, x) \right] . \end{aligned} \tag{3.3.13}$$

These WFs are uniquely defined by the modified orbitals $\overline{\Phi}^{(1,2)}(E,x)$, thereby avoiding the phase indeterminacy present in standard approaches (see Ref. [85]). Furthermore, the electron dynamics described by the tunneling Hamiltonian H in Eq. (3.3.3) using these WFs is equivalent to that derived from the original Schrödinger Hamiltonian (3.3.2) in the single-band approximation. This equivalence represents a crucial criterion for defining WFs.

It is noteworthy that $\Psi_{L,R}(x)$ in Eq. (3.3.13) and their derivatives are continuous over the entire interval $-\infty < x < \infty$ due to continuity of the eigenfunctions

$\psi_\pm(E_\pm,x)$ and their derivatives. Consequently, the representation of the WFs in terms of the modified orbitals $\overline{\Phi}^{(1,2)}$ must also be continuous, even though each orbital may exhibit discontinuities at the separation point $x=0$.

Eqs. (3.3.13) can be significantly simplified by employing a perturbative expansion within the TPA framework to approximate the energy spectrum in terms of the tunneling coupling Ω_0, since $\Omega_0 \propto \beta \propto T_0$. By neglecting terms involving Ω_0^2, the eigenenergies can be expressed using single-well orbitals, exploiting

$$\mathcal{E}_{1,2} \simeq E_0 \pm \Omega_0\,,$$

where E_0 is derived from Eqs. (3.3.5) and the energy shift Ω_0 is determined by the Bardeen formula in Eq. (3.3.11). Expanding the modified orbitals $\overline{\Phi}^{(1,2)}(E,x)$ in Eqs. (3.3.13) in powers of $E_\pm - E_0 = \pm\Omega_0$, and neglecting $\mathcal{O}(\Omega_0^2)$ terms, the WFs can be approximated as:

$$\Psi_L(x) = \overline{\Phi}_0^{(1)}(x) + \Omega_0 \partial_E \overline{\Phi}_0^{(2)}(x)\,, \tag{3.3.14a}$$

$$\Psi_R(x) = \overline{\Phi}_0^{(2)}(x) + \Omega_0 \partial_E \overline{\Phi}_0^{(1)}(x)\,. \tag{3.3.14b}$$

This result, first derived in Ref. [50] for a triple-well potential, can be further extended to multi-well systems. Here,

$$\overline{\Phi}_0^{(1,2)}(x) \equiv \Phi_0^{(1,2)}(E_0,x)$$

for $x \in \mathcal{X}_{1,2}$ (up to negligible corrections to the normalization) and vanish elsewhere, while

$$\partial_E \overline{\Phi}_0^{(1,2)}(x) \equiv [\partial \overline{\Phi}^{(1,2)}(E,x)/\partial E]_{E\to E_0}\,.$$

Note that, due to symmetry, $\overline{\Phi}_0^{(2)}(x) = \overline{\Phi}_0^{(1)}(-x)$. The resulting WFs $\Psi_{L,R}(x)$ in Eqs. (3.3.14) are already orthogonal, so that no more orthogonalization of the orbitals is needed. Eqs. (3.3.14) are composed of two *nonoverlapping* terms, that describe the WFs within their respective wells and their tails extending into adjacent wells. The second term, which is the contribution related to the WFs's tails, is proportional to Ω_0, and it is significantly smaller than the first one. This distinction highlights the close relation between the WFs' tails and the tunneling to neighboring sites, making them clearly different from corresponding orbitals. We emphasize that the WFs $\Psi_{L,R}(x)$ and their derivatives remain continuous at $x=0$, up to $\mathcal{O}(\Omega_0^2)$ terms, as implied by Eqs. (3.3.13). In fact, unlike the nodeless orbitals, the WFs' tails change sign, aligning with the orthogonality of $\Psi_{L,R}(x)$.

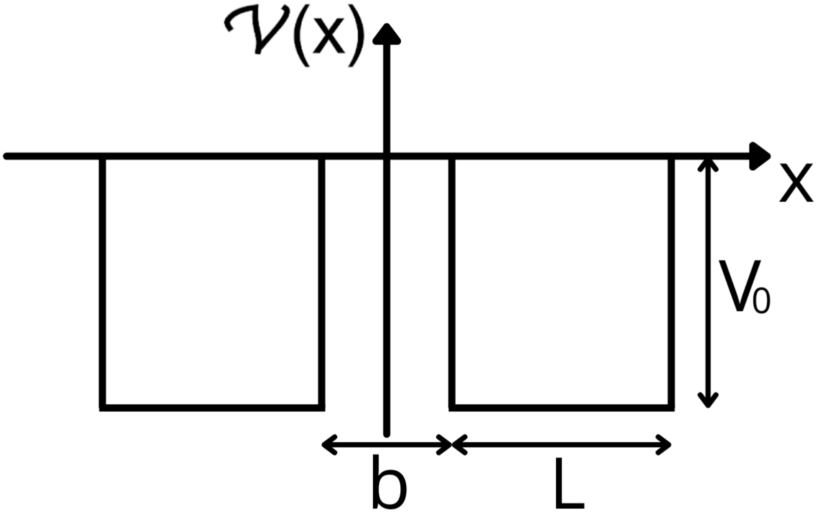

Figure 3.2: Symmetric square double-well potential, consisting of two rectangular wells of width L separated by a barrier of width b, with lattice depth $V_0 > 0$. Unless otherwise specified, we consider only one energy level per each well (SB nonstandard model), discarding all the other bound states, as well as the continuous spectrum.

3.3.3 Analytical approximated and exact Wannier functions for a double-well potential: a comparison

We exactly evaluate the WFs $\Psi_j(x)$ of the square double-well potential, shown in Fig. 3.2, comparing the results with those obtained with the TPA, and with the corresponding orbitals. The potential $\mathcal{V}(x)$ consists of two coupled rectangular potential wells, labeled by $j = 1, 2 \equiv L, R$, respectively denoting left and right well, given by

$$\mathcal{V}(x) = -V_0 \quad \text{for} \quad \frac{b}{2} < |x| < L + \frac{b}{2} \,. \tag{3.3.15}$$

From Eqs. (3.3.12), we obtain the exact eigenstates in terms of the modified orbitals $\overline{\Phi}^{(1,2)}(E_\pm, x)$, where $E_\pm$ correspond to the ground state and excited state, respectively. Since the modified orbitals $\overline{\Phi}^{(1,2)}(E, x)$ are normalized to unity for any energy E, we can demonstrate the orthogonality of the WFs in Eqs. (3.3.14) explicitly. Since the normalization factor of the modified orbitals $\overline{\Phi}^{(1,2)}(E, x)$ is energy dependent, it is useful to highlight it by introducing the following reduced orbitals

$$\overline{\Phi}^{(1,2)}(E_\pm, x) \equiv \mathcal{N}_\pm \overline{\phi}^{(1,2)}(E_\pm, x)\,, \tag{3.3.16}$$

where $\mathcal{N}_\pm$ is the normalization factor, defined as

$$\mathcal{N}_\pm \equiv \mathcal{N}(E_\pm) = \left(\int_{-\infty}^{0} \left[\overline{\phi}^{(1)}(E_\pm, x)\right]^2 dx \right)^{-1/2}\,, \tag{3.3.17}$$

while

$$\overline{\phi}^{(1)}(E, x) = \begin{cases} \frac{p}{\sqrt{V_0}} e^{q\left(x+L+\frac{b}{2}\right)} & \text{for } -\infty < x < -L - \frac{b}{2} \\ \cos\left[p\left(x + \frac{L+b}{2}\right) + \varphi\right] & \text{for } -L - \frac{b}{2} < x < -\frac{b}{2} \\ \mathcal{F}_1(E) e^{-q\left(x+\frac{b}{2}\right)} + \mathcal{F}_2(E) e^{q\left(x+\frac{b}{2}\right)} & \text{for } \quad -\frac{b}{2} < x < \infty \end{cases}\,, \tag{3.3.18a}$$

$$\overline{\phi}^{(2)}(E, x) = \overline{\phi}^{(1)}(E, -x)\,, \tag{3.3.18b}$$

where

$$p \equiv p(E) = \sqrt{V_0 + E}$$

and

$$q \equiv q(E) = \sqrt{-E}\,.$$

Here,

$$\mathcal{F}_1(E) = \frac{p}{\sqrt{V_0}} \cos(2\varphi) + \frac{p^2 - q^2}{2q\sqrt{V_0}} \sin(2\varphi)\,, \tag{3.3.19a}$$

$$\mathcal{F}_2(E) = -\frac{\sqrt{V_0}}{2q} \sin(2\varphi)\,, \tag{3.3.19b}$$

$$\varphi \equiv \varphi(E) = \frac{pL}{2} - \arccos\frac{p}{\sqrt{V_0}}\,, \tag{3.3.19c}$$

with the phase φ obtained from the matching conditions at $x = -L - b/2$. The eigenenergies are obtained by matching the logarithmic derivatives of $\overline{\phi}^{(1)}(E, x)$ and $\overline{\phi}^{(2)}(E, x)$ at $x = 0$. From Eqs. (3.3.18), we derive

$$\mathcal{F}_1(E) = \pm \mathcal{F}_2(E) e^{qb}\,. \tag{3.3.20}$$

Solving Eq. (3.3.20) for E, we find the first two eigenenergies $E_\pm$ of the double-well system. Then, substituting

$$\overline{\Phi}^{(1,2)}(E_\pm, x) \equiv \overline{\Phi}^{(1,2)}_\pm(x)$$

into Eqs. (3.3.12), we find the exact eigenstates for the double-well potential.

From Eqs. (3.3.16), it follows

$$\overline{\Phi}_0^{(1,2)}(x) = \mathcal{N}_0 \overline{\phi}_0^{(1,2)}(x)\,,$$

where

$$\overline{\phi}_0^{(1,2)}(x) \equiv \overline{\phi}_0^{(1,2)}(E_0, x)$$

and $\mathcal{N}_0 \equiv \mathcal{N}(E_0)$ is the normalization factor, defined as:

$$\mathcal{N}_0 = \left(\frac{L}{2} + \frac{1}{q_0}\right)^{-1/2}\,. \tag{3.3.21}$$

Expanding the term $\mathcal{N}_\pm$ in Eq. (3.3.17) up to $\mathcal{O}(\Omega_0)$ terms, we obtain

$$\mathcal{N}_\pm \simeq \mathcal{N}_0 \pm \Omega_0(\partial_E \mathcal{N}_0)\,,$$

where

$$\begin{aligned} \partial_E \mathcal{N}_0 = &\left.\frac{\partial \mathcal{N}(E)}{\partial E}\right|_{E\to E_0} = \\ = &-\mathcal{N}_0^3 \int\limits_{-\infty}^{0} \overline{\phi}^{(1)}(E,x)\, \frac{\partial}{\partial E}\overline{\phi}^{(1)}(E,x)\Big|_{E\to E_0}\, dx\,. \end{aligned} \tag{3.3.22}$$

Substituting $\overline{\Phi}_0^{(1,2)}(x)$ into Eqs. (3.3.14), we obtain (up to $\mathcal{O}(\Omega_0^2)$ terms)

$$\Psi_{L,R}(x) = \mathcal{N}_0 \overline{\phi}_0^{(1,2)}(x) + \Omega_0 \left[\mathcal{N}_0 \partial_E \overline{\phi}_0^{(2,1)}(x) + \overline{\phi}_0^{(2,1)}(x)\,(\partial_E \mathcal{N}_0)\right]\,, \tag{3.3.23}$$

where

$$\partial_E \overline{\phi}_0(x) \equiv [\partial \overline{\phi}(E,x)/\partial E]_{E\to E_0}\,.$$

From Eqs. (3.3.17) and Eq. (3.3.22), we can verify that the WFs $\Psi_{L,R}(x)$ in Eqs. (3.3.23) are orthogonal (up to $\mathcal{O}(\Omega_0^2)$ terms):

$$\begin{aligned} &\int\limits_{-\infty}^{0} \Psi_L(x)\Psi_R(x)\, dx = \Omega_0 \mathcal{N}_0^2 \left(1 - \mathcal{N}_0^2 \int\limits_{-\infty}^{0} \left[\overline{\phi}_0^{(1)}(x)\right]^2 dx\right) = \\ &= \int\limits_{-\infty}^{0} \overline{\phi}_0^{(1)}(x) \partial_E \overline{\phi}_0^{(1)}(x)\, dx = \mathcal{O}(\Omega_0^2)\,. \end{aligned} \tag{3.3.24}$$

Eqs. (3.3.14), or equivalently Eqs. (3.3.23), represent our main result regarding the WFs, that can be relevant for a broad range of multiwell systems (for further

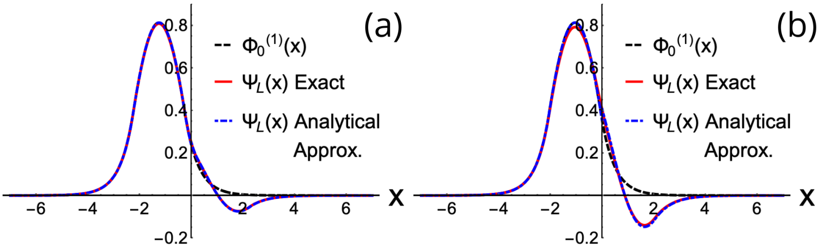

Figure 3.3: Comparison between the left-well orbital $\Phi_0^{(1)}(x)$ (black dashed curve), the exact (red solid curve) and our analytical approximated (blue dot-dashed curve) left-well WF $\Psi_L(x)$. The results are obtained considering the double-well potential in Fig. 3.2 for $V_0 = 5$, $L = 2$, and two different barrier widths: $b = 0.5$ in panel (a) and $b = 0.1$ in panel (b). The exact ground-state energy E_0 of the single-well and the tunneling coupling Ω_0 are $\overline{E}_0 = \frac{E_+ + E_-}{2} \simeq -3.866, -3.940$ and $\overline{\Omega}_0 = \frac{E_+ - E_-}{2} \simeq -0.223, -0.489$, respectively. The corresponding parameters given by the TPA (single-well) are $E_0 \simeq -3.867, -3.932$ and $\Omega_0 \simeq -0.224, -0.490$, respectively.

details about the application of our method to different types of multiwell systems, see Appendix D and Appendix E). In the following, we will assess these WFs predictions by comparing them with the orbitals and the results obtained from the exact solutions of the Schrödinger equation, considering the symmetric double-well potential in Eq. (3.3.15). For the TPA results, the eigenenergies are evaluated via single-well orbitals, using Eqs. (3.3.5). To make this comparison, we consider

$$E = E_0 \pm \Omega_0$$

in Eqs. (3.3.19) and Eq. (3.3.20), together with

$$E_0 = (E_+ + E_-)/2\,,$$

$$\Omega_0 = (E_+ - E_-)/2\,.$$

We solve Eq. (3.3.20) by taking into account that the barrier penetration coefficient $e^{-qb} \propto \Omega_0$, and by using

$$\varphi(E_0 \pm \Omega_0) = \pm\left(1 + q_0\frac{L}{2}\right)\frac{\Omega_0}{2p_0q_0} \equiv \pm\frac{\Omega_0}{2p_0\mathcal{N}_0^2}\,. \tag{3.3.25}$$

By expanding Eq. (3.3.19a) and Eq. (3.3.19b) in powers of Ω_0, we obtain

$$\mathcal{F}_1(E) \approx \frac{p_0}{\sqrt{V_0}} + \mathcal{O}(\Omega_0^2)\,, \tag{3.3.26a}$$

$$\mathcal{F}_2(E) \approx -\frac{\sqrt{V_0}}{q}\varphi + \mathcal{O}(\Omega_0^2)\,. \tag{3.3.26b}$$

Substituting Eqs. (3.3.26) in Eq. (3.3.20), we obtain

$$\Omega_0 = -2\mathcal{N}_0^2\frac{q_0 p_0^2}{V_0}e^{-q_0 b}\,, \tag{3.3.27}$$

that corresponds to the Bardeen formula in Eq. (3.3.11) obtained with the TPA.

The exact WFs $\Psi_{L,R}(x)$ are obtained expanding the modified orbitals in Eqs. (3.3.23) up to $\mathcal{O}(\Omega_0)$ terms, where

$$\partial_E\overline{\phi}_0^{(1)}(x) = \begin{cases} \frac{1}{2\sqrt{V_0}}\mathcal{D}_1(x)e^{q_0\left(x+L+\frac{b}{2}\right)} & \text{for } -\infty < x < -L-\frac{b}{2} \\ -\frac{1}{2p_0}\mathcal{D}_2(x)\sin\left[p_0\left(x+\frac{L+b}{2}\right)\right] & \text{for } -L-\frac{b}{2} < x < -\frac{b}{2} \\ \frac{1}{2\sqrt{V_0}}\mathcal{D}_3(x) & \text{for } \quad -\frac{b}{2} < x < \infty \end{cases}\,, \tag{3.3.28a}$$

$$\partial_E\overline{\phi}_0^{(2)}(x) = -\partial_E\overline{\phi}_0^{(1)}(x)\,, \tag{3.3.28b}$$

where

$$\mathcal{D}_1(x) \equiv \frac{1}{p_0} - \frac{p_0}{q_0}\left(x+L+\frac{b}{2}\right)\,,$$

$$\mathcal{D}_2(x) \equiv \frac{1}{q_0} + x + L + \frac{b}{2}\,,$$

$$\mathcal{D}_3(x) \equiv \left[\frac{p_0}{q_0}\left(x+\frac{L+b}{2}\right) + \frac{p_0}{q_0^2} - \frac{q_0 L}{2p_0}\right]e^{-q_0\left(x+\frac{b}{2}\right)} - \frac{V_0\left(1+\frac{q_0 L}{2}\right)}{p_0 q_0^2}e^{q_0\left(x+\frac{b}{2}\right)}$$

and

$$\partial_E\mathcal{N}_0 = -\mathcal{N}_0^3\,\frac{p_0^2 - \left[q_0^2 - p_0^2\left(1-q_0 b\right)\right]\left(1+q_0\frac{L}{2}\right)}{4p_0^2 q_0^3}\,. \tag{3.3.29}$$

In Fig. 3.3, we compare the left-well WF $\Psi_L(x)$ obtained from our analytical approximated results in Eq. (3.3.14a) with the orbital $\Phi_0^{(1)}(x)$ from Eqs. (3.3.5) and the exact solution obtained from the Schrödinger equation, for different values of barrier width b. Looking at Fig. 3.3, we observe that the left-well orbital $\Phi_0^{(1)}(x)$ approximates very well the corresponding WF in the left well region, confirming the high accuracy of the TPA for the evaluation of the tunneling Hamiltonian parameters. However, we note that $\Phi_0^{(1)}(x)$ has a very different tail into the neighboring well compared to the exact WF's one. In particular, the latter changes its sign in the right well, in agreement with Eq. (3.3.24) and our general arguments. This effect has deep implications for the evaluation of tunneling transition amplitudes in the presence of interparticle interaction. Finally, comparing Fig. 3.3(a) with Fig. 3.3(b), we note that in the case of narrow barrier, see Fig. 3.3(b), the tunneling energy increases (and consequently the WF's tail becomes more evident), so that the neglected higher order terms become more important, and the analytical approximated results deviate from the exact solution.

Overall, the analytical approximated solution demonstrates high accuracy in modeling the exact WF, both in the well's and in the tail's regions. The exact solution, derived from the Schrödinger equation, describes the behavior of the system, including the modification in the WF's tail and its behavior across the barrier. On the other hand, the analytical approximated approach provides a robust and efficient alternative. This analytical method works very well across a broad range of conditions, effectively capturing the essential physics with significantly reduced computational effort. Thus, while the exact approach is essential for detailed studies, the analytical approximation is a powerful tool for theoretical explorations, especially in scenarios where computational resources are limited.

3.4 Nonstandard Hubbard terms in a double-well potential

So far, we have considered one particle placed in a double-well potential, deriving the corresponding WFs and comparing the analytical approximated results with the exact results and the orbitals.

In this Section, we consider two particles placed in the same double-well system, analysing the implications of the interparticle interaction on the total Hamiltonian of the system. Specifically, we use the results obtained in Sec. 3.3 to derive simple analytical approximated expressions for the nonstandard DT and PT terms, as well as the standard on-site two-particle interaction energy U, in order to establish their magnitude as a function of the system's parameters.

3.4.1 Standard and nonstandard Hubbard terms

Let us consider two distinguishable particles, hereinafter referred to with the labels (1) and (2) (e.g. two fermions with opposite spin projections), occupying the symmetric double-well potential of Fig. 3.2, interacting through a two-body *repulsive* potential $V(x-y) > 0$, where x, y are the spatial coordinates of the two particles. In the site basis, the corresponding tunneling Hamiltonian, see Eq. (3.3.3) and Ch. 2, can be written as

$$\begin{aligned} \hat{H} = E_0 \left(\hat{n}_L^{(1)} + \hat{n}_L^{(2)} + \hat{n}_R^{(1)} + \hat{n}_R^{(2)} \right) + \\ + \Omega_0 \left(\hat{a}_L^{\dagger(1)} \hat{a}_R^{(1)} + \hat{a}_L^{\dagger(2)} \hat{a}_R^{(2)} + H.c. \right) + \hat{V} \,, \end{aligned} \tag{3.4.1}$$

where

$$\hat{n}_{L,R}^{(1,2)} = \hat{a}_{L,R}^{\dagger(1,2)} \hat{a}_{L,R}^{(1,2)}$$

are the number operators for the left and right well, E_0 is the site energy and Ω_0 is the single-particle tunneling coupling. The interaction potential $\hat{V}$ in Eq. (3.4.1) is a sum of terms of form

$$\hat{a}_{i'}^{\dagger(1)} \hat{a}_{j'}^{\dagger(2)} V_{i'j',ij} \hat{a}_i^{(1)} \hat{a}_j^{(2)} \,.$$

In the tunneling Hamiltonian basis, its matrix elements are:

$$V_{i'j',ij} = \int \Psi_{i'}(x) \Psi_{j'}(y) V(x-y) \Psi_i(x) \Psi_j(y) \, dx \, dy \,, \tag{3.4.2}$$

where $\Psi_i(x)$ is the i-th site WF, and $i = L, R$.

The Hubbard interaction potential in second quantization formalism can be written as

$$\begin{aligned} \hat{V}_H \equiv U \left(\hat{n}_L^{(1)} \hat{n}_L^{(2)} + \hat{n}_R^{(1)} \hat{n}_R^{(2)} \right) + \\ + \overline{U} \left(\hat{n}_L^{(1)} \hat{n}_R^{(2)} + \hat{n}_L^{(2)} \hat{n}_R^{(1)} \right) \,, \end{aligned} \tag{3.4.3}$$

with

$$U = \int n_L(x) n_L(y) V(x-y) \, dx \, dy \,, \tag{3.4.4}$$

and

$$\overline{U} = \int n_L(x) n_R(y) V(x-y) \, dx \, dy \,, \tag{3.4.5}$$

being the standard and the extended Hubbard terms, representing on-site and nearest neighbor interaction, respectively, and

$$n_{L,R}(x) = \Psi_{L,R}^2(x) \,.$$

The second term in Eq. (3.4.3), proportional to $\overline{U}$, is not present in the standard Hubbard model Hamiltonian, and gives rise to the *extended* Hubbard model

[43]. Similarly to the standard Hubbard term, the latter does not generate tunneling transitions, rather it gives an extra contribution to the total energy of the system.

In contrast, nonstandard Hubbard terms generate tunneling transitions between left and right well. The DT and PT terms can be respectively written as

$$\begin{aligned}\hat{V}_{DT} = \Omega_1 \Big[& \left(\hat{n}_L^{(1)} + \hat{n}_R^{(1)}\right)\left(\hat{a}_L^{\dagger(2)}\hat{a}_R^{(2)} + H.c.\right) + \\ & + \left(\hat{n}_L^{(2)} + \hat{n}_R^{(2)}\right)\left(\hat{a}_L^{\dagger(1)}\hat{a}_R^{(1)} + H.c.\right)\Big] ,\end{aligned} \tag{3.4.6a}$$

$$\hat{V}_{PT} = \Omega_2 \left[\hat{a}_R^{\dagger(1)}\hat{a}_R^{\dagger(2)}\hat{a}_L^{(1)}\hat{a}_L^{(2)} + \hat{a}_R^{\dagger(1)}\hat{a}_L^{\dagger(2)}\hat{a}_L^{(1)}\hat{a}_R^{(2)} + H.c.\right] , \tag{3.4.6b}$$

with corresponding transition amplitudes given respectively by:

$$\Omega_1 = \int \Psi_L^2(x)\Psi_L(y)V(x-y)\Psi_R(y)\,dx\,dy\,, \tag{3.4.7a}$$

$$\Omega_2 = \int \Psi_L(x)\Psi_L(y)V(x-y)\Psi_R(x)\Psi_R(y)\,dx\,dy\,. \tag{3.4.7b}$$

The first nonstandard Hubbard term DT, given by Eq. (3.4.6a), consists of a single-particle hopping process (e.g. $\Psi_{LL} \rightarrow \Psi_{LR}$) between the two wells resulting from the interaction of the tunneling particle with the nontunneling one (also known as bond-charge interaction, see Ref. [1]). Its tunneling amplitude (Ω_1) sums up with the free single-particle tunneling amplitude, given by the tunneling energy Ω_0 in the Hamiltonian in Eq. (3.4.1), resulting in an interaction-dependent effective single-particle tunneling [43, 45], expressed as

$$\Omega_0\left(\hat{a}_R^{\dagger(1)}\hat{a}_L^{(1)} + H.c.\right) \rightarrow \hat{\Omega}_{eff}\left(\hat{a}_R^{\dagger(1)}\hat{a}_L^{(1)} + H.c.\right) , \tag{3.4.8}$$

where

$$\hat{\Omega}_{eff} = \Omega_0 + \Omega_1\left(\hat{n}_L^{(2)} + \hat{n}_R^{(2)}\right) \tag{3.4.9}$$

represents the effective single-particle tunneling operator, explicitly dependent on the occupation numbers of the two wells, through the factor $\hat{n}_L^{(2)} + \hat{n}_R^{(2)}$. Particularly, in a double-well potential with constant total density, the DT amplitude in Eq. (3.4.7a) can always be incorporated into the single-particle tunneling amplitude, see Refs. [43, 45], yielding an effective tunneling

$$\Omega_{eff} \equiv \Omega_0 + \Omega_1\,.$$

Looking at Eq. (3.4.9), it is then clear that the interaction strength can be tuned in such a way to modify Ω_1, and in turn Ω_{eff}.

The second nonstandard Hubbard term, given by Eq. (3.4.6b), describes a simultaneous two-particle PT coherent hopping process, that can be both direct (e.g. $\Psi_{LL} \to \Psi_{RR}$) or exchange (e.g. $\Psi_{LR} \to \Psi_{RL}$). This term, with amplitude Ω_2, arises when the interaction matrix is connecting two states where both particles switch their site location, representing an additional nonstandard physical process not present in the standard Hubbard Hamiltonian. Note that both nonstandard Hubbard amplitudes in Eqs. (3.4.7) contain the overlap between the WFs belonging to neighboring wells. For this reason, they strongly depend not only on the shape of the interacting potential $V(x-y)$, but also on the WFs' tails in the neighboring wells. Therefore, an accurate evaluation and an analytical estimate of the WFs' tails are crucial in the determination of the nonstandard Hubbard terms.

3.5 Analytical approximated results with contact interaction

3.5.1 Contact interaction

Let us consider two distinguishable particles interacting through a δ-shaped (*contact*) interaction potential [116, 117]. Contrary to the results obtained in Ch. 2, our focus here is on the analytical evaluation of all terms included in the Hamiltonian. In fact, by employing δ-shaped interaction, we simplify the mathematical treatment of Eq. (3.4.2), enabling a more precise and manageable analysis of the dynamic behavior of the system. At first, we consider a *repulsive* δ-shaped interaction potential between particles, defined as

$$V(x-y) = V_\delta \delta(x-y)\,, \tag{3.5.1}$$

where $V_\delta > 0$ is the interaction strength. From Eq. (3.5.1), we can exactly evaluate the interaction potential matrix elements in Eq. (3.4.2). Specifically, we focus on the standard Hubbard term in Eq. (3.4.4) and the DT and PT terms in Eqs. (3.4.7), and we compare the exact results with the analytical approximated ones.

We start our analysis with the on-site standard Hubbard term U, given by Eq. (3.4.4). Using Eqs. (3.3.14), and neglecting $\mathcal{O}(\Omega_0^2)$ terms, we find

$$U = V_\delta \mathcal{N}_0^4 \int\limits_{-\infty}^{0} \left[\overline{\phi}_0^{(1)}(x)\right]^4 dx = \frac{3}{4}\mathcal{N}_0^2 V_\delta \left(1-\eta\right)\,, \tag{3.5.2}$$

where $\mathcal{N}_0$ is the normalization factor, see Eq. (3.3.21), and

$$\eta = \frac{p_0^2}{3V_0\left(1+\frac{q_0 L}{2}\right)} \, .$$

We then evaluate the DT amplitude Ω_1, given by Eq. (3.4.7a). Considering the symmetry of the WFs, namely $\Psi_R(x) = \Psi_L(-x)$, combined with Eqs. (3.3.14), and neglecting $\mathcal{O}(\Omega_0^2)$ terms, we find

$$\Omega_1 = V_\delta \int\limits_{-\infty}^{\infty} \Psi_L(x)^3 \Psi_R(x)\, dx = \Omega_0 V_\delta \int\limits_{-\infty}^{0} \left(\overline{\Phi}_0^{(1)}(x)\right)^3 \partial_E \overline{\Phi}_0^{(1)}(x)\, dx \, , \tag{3.5.3}$$

From Eqs. (3.3.23), we can rewrite Ω_1 as the sum of two components, namely

$$\Omega_1 = \Omega_1^{(1)} + \Omega_1^{(2)} \, ,$$

given by

$$\Omega_1^{(1)} = \Omega_0 V_\delta \mathcal{N}_0^4 \int\limits_{-\infty}^{0} \left(\overline{\phi}_0^{(1)}(x)\right)^3 \partial_E \overline{\phi}_0^{(1)}(x)\, dx \, , \tag{3.5.4a}$$

$$\Omega_1^{(2)} = \Omega_0 V_\delta \mathcal{N}_0^3 \left(\partial_E \mathcal{N}_0\right) \int\limits_{-\infty}^{0} \left[\overline{\phi}_0^{(1)}(x)\right]^4 dx = \Omega_0 U \frac{\partial_E \mathcal{N}_0}{\mathcal{N}_0} \, . \tag{3.5.4b}$$

These two components come from the dimensionless reduced orbital and the energy dependent normalization factor, respectively, see Eq. (3.3.16).

3.5.2 Single-particle tunneling amplitude renormalization due to density-induced tunneling

Since, for *contact* interaction, the DT term Ω_1 is proportional to Ω_0, it effectively renormalizes the tunneling coupling, see Eq. (3.4.9), so that

$$\Omega_0 \to \Omega_{eff} = \Omega_0 + \Omega_1 \equiv \Omega_0\left(1 + gV_\delta\right) \, . \tag{3.5.5}$$

Note that, according to Eq. (3.5.5), if the ratio Ω_1/Ω_0 is negative, the effective tunneling coupling Ω_{eff} can be reduced by the interaction strength V_δ. In other words, the DT term can either increase or decrease the single-particle tunneling coupling Ω_0, depending on the sign of the coefficient g. Specifically, in the case of repulsive interaction ($V_\delta > 0$) and a negative coefficient ($g < 0$), the DT term decreases the magnitude of the effective single-particle tunneling coupling Ω_{eff}. With a sufficiently large interaction strength V_δ, the single-particle tunneling can eventually be completely suppressed.

Hence, the sign of the coefficient g becomes crucial to understand how the DT term affects the system's dynamics. At present, there is no general agreement on the sign of the coefficient g (or even on its magnitude) [1, 43, 70]. This problem has been investigated analytically in the framework of our simple toy-model, that allows a precise evaluation of the WFs' tails, in Ref. [50]. In that work, by analysing Eq. (3.3.24) and Eq. (3.5.3), it was shown that $\Omega_1 < 0$ for contact interaction, so that the DT term can never match Ω_0 and therefore suppress the effective single-particle tunneling Ω_{eff}. On the other hand, only in presence of long-range interaction, it is possible to arrange the parameters of the well and the interparticle interaction in such a way to have $\Omega_{eff} = 0$.

As said, the square double-well potential system allows us to obtain a simple analytical approximated expression for Ω_1, which clearly shows the sign and the magnitude of the DT amplitude as a function of the system's parameters. Indeed, by using Eq. (3.3.21), Eqs. (3.3.28), Eq. (3.3.29), Eq. (3.5.2) and Eq. (3.5.3), we find two analytical approximated expressions for $\Omega_1 = \Omega_1^{(1)} + \Omega_1^{(2)}$, that read:

$$\begin{aligned}\Omega_1^{(1)} &= V_\delta \Omega_0 \mathcal{N}_0^4 \frac{\left(4p_0^4 - 3q_0^2 V_0\right)\left(1 + q_0 \frac{L}{2}\right) + p_0^2\left(p_0^2 + V_0\right)}{32 p_0^2 q_0^3 V_0} = \\ &= -\frac{3 V_\delta \Omega_0 \mathcal{N}_0^2}{32 p_0^2}\left[1 + \mathcal{O}\left(\frac{p_0^2}{V_0}\right)\right] ,\end{aligned} \tag{3.5.6a}$$

$$\begin{aligned}\Omega_1^{(2)} &= -3 V_\delta \Omega_0 \mathcal{N}_0^2 \frac{\mathcal{N}_0^2 p_0^2 - \left[q_0^3 - p_0^2 q_0 \left(1 - 2 q_0 b\right)\right]}{16 p_0^2 q_0^3}(1 - \eta) = \\ &= \frac{6 V_\delta \Omega_0 \mathcal{N}_0^2}{32 p_0^2}\left[1 + \mathcal{O}\left(\frac{p_0^2}{V_0}\right)\right] .\end{aligned} \tag{3.5.6b}$$

In Eqs. (3.5.6), we neglect $\mathcal{O}(p_0^2/V_0)$ terms, since we deal with the SB approximation, which considers only the lowest-band, where $p_0 \ll \sqrt{V_0}$. Note that the previous condition means $|E_0| \simeq V_0$, which implies $q_0 \simeq \sqrt{V_0}$. The expansion holds assuming also the condition $1 + q_0 L \gg 1$, corresponding to the Bohr quantization rule. Looking at Eqs. (3.5.6), we find that the first component $\Omega_1^{(1)}$ of the DT term, coming from the energy-dependence of the orbital, is always positive, while the second component $\Omega_1^{(2)}$, arising from a variation of the normalization factor with energy, is twice larger and of opposite sign ($\Omega_1^{(2)} \simeq -2\Omega_1^{(1)}$). As a result, the coefficient g is always positive for contact interaction. This clearly shows the necessity of an accurate evaluation of the WFs' tails to determine the sign of DT term, which is hard to determine from general arguments, since the energy dependence of the normalization factors plays a crucial role.

3.5.3 Pair tunneling

Finally, we analyze the PT amplitude Ω_2, given by Eq. (3.4.7b). Cotunneling refers to a general phenomenon that arises from second-order terms in the standard Hubbard model, as well as from the nonstandard PT term in the exact model. By applying Eqs. (3.3.23) and exploiting the symmetry property $\Psi_R(x) = \Psi_L(-x)$ of the WFs, we can write

$$\begin{aligned}
\Omega_2 &= V_\delta \int_{-\infty}^{+\infty} \Psi_L^2(x)\Psi_R^2(x)\, dx = \\
&= 2V_\delta \Omega_0^2 \mathcal{N}_0^2 \int_{-\infty}^{0} \left(\overline{\phi}_0^{(1)}(x)\right)^2 \left[\mathcal{N}_0 \partial_E \overline{\phi}_0^{(1)}(x) + \overline{\phi}_0^{(1)}(x)(\partial_E \mathcal{N}_0)\right]^2 dx = \\
&= \Omega_2^{(1)} + 2\Omega_0 \frac{\partial_E \mathcal{N}_0}{\mathcal{N}_0}\left[2\Omega_1^{(1)} + \Omega_1^{(2)}\right],
\end{aligned} \tag{3.5.7}$$

where

$$\Omega_2^{(1)} = 2V_\delta \Omega_0^2 \mathcal{N}_0^4 \int_{-\infty}^{0} \left[\overline{\phi}_0^{(1)}(x)\right]^2 \left(\partial_E \overline{\phi}_0^{(1)}(x)\right)^2 dx\,. \tag{3.5.8}$$

Since $\Omega_1^{(1,2)}$ are the two components of the DT term obtained in Eqs. (3.5.6), we only need to evaluate $\Omega_2^{(1)}$ in Eq. (3.5.8). By substituting Eqs. (3.3.14), Eqs. (3.3.28) and Eq. (3.3.29) into Eq. (3.5.8), the calculation can be performed analytically. By neglecting $\mathcal{O}(\Omega_0^3)$ terms, we find

$$\Omega_2^{(1)} = \frac{\mathcal{N}_0^4 V_\delta \Omega_0^2}{2p_0^2 q_0^3}\left[\frac{\mathcal{A}_0 + \mathcal{A}_1\left(q_0\frac{L}{2}\right)}{32 p_0^2 V_0 q_0^2} + \frac{\mathcal{A}_2\left(q_0\frac{L}{2}\right)^2}{4V_0 q_0^2} + \frac{\left(q_0\frac{L}{2}\right)^3}{3}\right], \tag{3.5.9}$$

where

$$\begin{aligned}
\mathcal{A}_0 &= 43p_0^6 - p_0^4 V_0(65 - 16q_0 b) + 13p_0^2 V_0^2 - V_0^3\,, \\
\mathcal{A}_1 &= 92p_0^6 - p_0^4 V_0(161 - 32q_0 b) + 34p_0^2 V_0^2 - V_0^3\,, \\
\mathcal{A}_2 &= 6p_0^4 - p_0^2 V_0(13 - 2q_0 b) + 4V_0^2\,.
\end{aligned}$$

In the limit $|E_0| \ll V_0$, corresponding to the SB condition, the relation

$$2\Omega_1^{(1)} + \Omega_1^{(2)} \to 0$$

holds. Therefore, Eq. (3.5.7) becomes $\Omega_2 = \Omega_2^{(1)}$, which is given by a simple analytical approximated expression:

$$\Omega_2 = \frac{2\mathcal{N}_0^4 V_\delta \Omega_0^2}{4p_0^2 q_0^3} \left[\frac{\left(q_0 \frac{L}{2}\right)^3}{3} + \frac{V_0 \left(q_0 \frac{L}{2}\right)^2}{q_0^2} - \frac{V_0^2 \left(1 + q_0 \frac{L}{2}\right)}{32 p_0^2 q_0^2} \right] . \tag{3.5.10}$$

This result implies that the two-particle coherent tunneling amplitude Ω_2 is proportional to the interaction strength V_δ. Therefore, for large enough V_δ, the PT amplitude Ω_2 dominates over the corresponding cotunneling hopping amplitude of the standard Hubbard model, given by

$$\omega \equiv \frac{2\Omega_0^2}{U} ,$$

that decreases with the interaction strength V_δ, as pointed out in the Introduction and since $U \propto V_\delta$, see Eq. (3.5.2) and also Ref. [53]. As expected, the DT term is $\propto \Omega_0$, see Eq. (3.5.3), while the PT term is $\propto \Omega_0^2$, see Eq. (3.5.10).

3.5.4 Exact and analytical approximated results: a comparison

A comparison between exact and analytical approximated results for these terms is presented in Fig. 3.4. Specifically, we evaluate the on-site standard Hubbard term U, the noninteracting single-particle tunneling Ω_0, the DT term Ω_1, the PT term Ω_2 and the second-order cotunneling $\omega = 2\Omega_0^2/U$ as a function of the lattice depth V_0 in Fig. 3.4(a) and of the well width L in Fig. 3.4(b). The exact results for U, Ω_0, Ω_1 and Ω_2 are given by Eq. (3.4.4), Eq. (3.3.4b), Eq. (3.4.7a) and Eq. (3.4.7b), respectively. In the same way, the analytical approximated results are given by Eq. (3.5.2), Eq. (3.3.11), Eq. (3.5.6) and Eq. (3.5.7), respectively. Looking at Fig. 3.4, our analytical approximated results show an excellent match with numerical simulations across various parameters, including the lattice depth V_0 and the well width L. This strong agreement between the analytical approximated and numerical results confirms the validity and robustness of our method. In fact, it demonstrates that our analytical approach is capable of accurately capturing the essential physics of the system, providing a reliable alternative to computationally intensive simulations. However, we observe that this agreement fails for low values of V_0 and L. Specifically, for such low values of these parameters, the tunneling energy Ω_0 increases. A low lattice depth V_0 results in a higher Ω_0, while

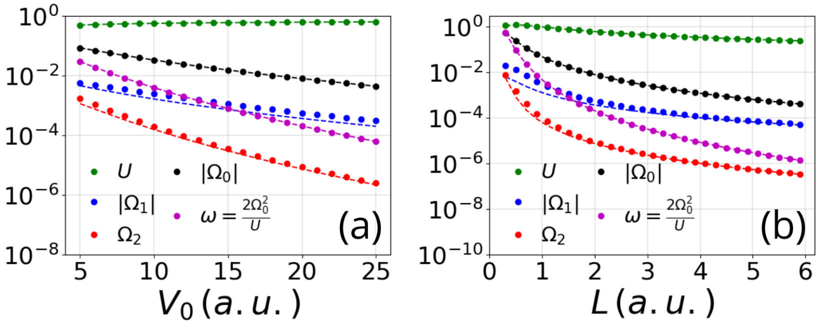

Figure 3.4: Comparison of exact results (dots) and analytical approximated results (dashed curves) for the Hubbard term U (green curve), DT amplitude $|\Omega_1|$ (blue curve), PT amplitude Ω_2 (red curve), single-particle tunneling $|\Omega_0|$ (black curve) and standard Hubbard second-order cotunneling ω (purple curve). The results are obtained considering two distinguishable particles placed in a square double-well potential, interacting via δ-shaped interaction with $V_\delta = 1$, as a function of the lattice depth V_0 (with $L = 2$ and $b = 1$) in panel (a) and of the well width L (with $b = 1$ and $V_0 = 20$) in panel (b).

a low well width L leads to higher energy levels and, consequently, a larger tunneling amplitude, see Eq. (3.3.4b). For these high values of Ω_0, our analytical approximated approach fails, as the perturbation parameter is proportional to Ω_0 itself, and it cannot be used as an expansion parameter.

3.6 Comparison with existing literature

In this Section, we extend our numerical results to different shapes of double-well potential, demonstrating the versatility of our numerical method. This expanded analysis shows the robustness of our approach across different configurations, underscoring its adaptability and the broader applicability of our findings beyond the initial setup. To do so, we compare our theoretical predictions with the results obtained in Ref. [1], where the authors focus on the DT process of bosons in optical lattices and on how their density affects this process. Specifically, we adapt the shape of the double-well potential, considering a 1D double-well potential defined as

$$\mathcal{V}(x) = V_0 \cos^2\left(\frac{\pi x}{\lambda}\right), \qquad (3.6.1)$$

where V_0 is the lattice depth and λ is the periodicity of the lattice. We perform our numerical simulations by considering two bosons interacting via δ-shaped interaction. Note that our exact results obtained with distinguishable particles can be straightforwardly generalized for bosonic particles (as well as for fermionic particles, see Ch. 2). It is important to highlight that our approach differs significantly in the choice of WFs used. While Ref. [1] employs the MLWFs, we adopt our new method for generating WFs.

Specifically, in Ref. [1], the authors claim that the DT process can be relevant for the system's dynamics, since it can modify the free single-particle tunneling. In general, they demonstrate how nonstandard Hubbard models can describe more precisely the physics of bosonic atoms in lattice systems, including nonstandard terms not accounted for in the Hubbard model. In this work, the full lowest-band interaction Hamiltonian is defined as

$$\hat{H}_{int} = \frac{1}{2}\sum_{ijkl} V_{ijkl}\hat{b}_i^\dagger \hat{b}_j^\dagger \hat{b}_k \hat{b}_l \,, \tag{3.6.2}$$

where $\hat{b}_i^{(\dagger)}$ is the annihilation (creation) operator for a bosonic particle in the ground state of the i-th site and

$$V_{ijkl} = 8\pi a_s \int \Psi_i(x)\Psi_j(x)\Psi_k(x)\Psi_l(y)\, d^3x \tag{3.6.3}$$

are the interaction matrix elements, where a_s is the free space s-wave scattering length, m is the mass of the bosonic particle and $\Psi_i(x)$ is the lowest-band i-th site WF. Note that Eq. (3.6.3) can be traced back to Eq. (3.4.2), considering that the interaction strength V_δ between two particles interacting via s-wave scattering is given by $V_\delta = 8\pi a_s$ (see Ref. [118]). Eq. (3.6.2) introduces also an off-site interaction between neighboring sites, which leads to different physical processes compared to the standard Hubbard model. Specifically, we focus on the DT and PT terms.

In Fig. 3.5, we compare results presented in Ref. [1] with our model predictions. Specifically, we analyse the on-site standard Hubbard term U, the noninteracting single-particle tunneling Ω_0, the DT term Ω_1, the PT term Ω_2 and the second-order cotunneling $\omega = 2\Omega_0^2/U$ as a function of the lattice depth V_0. All the quantities are expressed in units of the recoil energy

$$E_r = \frac{h^2}{2m\lambda^2} \,,$$

where m is the mass of the atoms, h is the Planck's constant and $\lambda = 765\ nm$ represents the periodicity of the lattice. Our results highlight the effectiveness of our numerical method in accurately capturing the essential dynamics of bosonic systems in optical lattices. The analytical predictions from our method show a remarkable agreement with the theoretical results found in the literature,

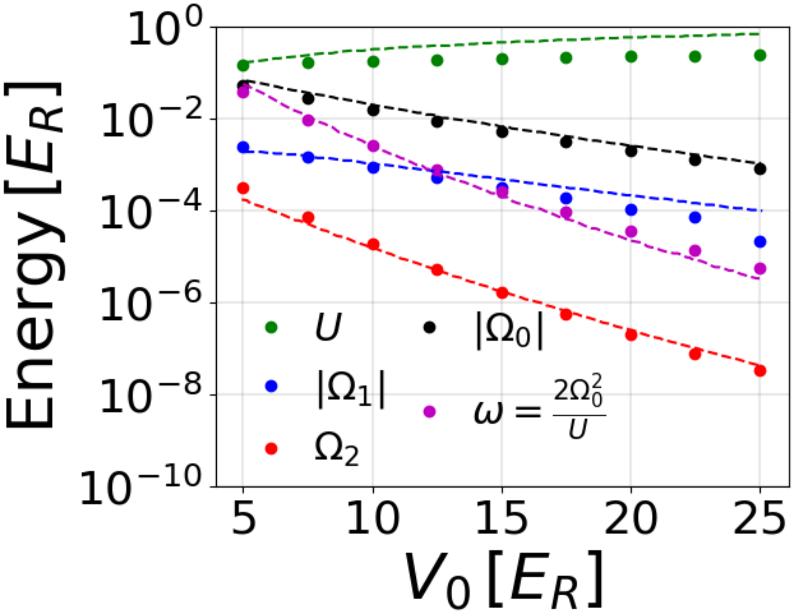

Figure 3.5: Comparison of exact results obtained with the SB nonstandard model (dots) and results from Ref. [1] (dashed curves) for the Hubbard term U (green curve), DT amplitude $|\Omega_1|$ (blue curve), PT amplitude Ω_2 (red curve), single-particle tunneling $|\Omega_0|$ (black curve) and standard Hubbard model second-order cotunneling $\omega = 2\Omega_0^2/U$ (purple curve). The results are obtained considering two bosons placed in the double-well potential of Eq. (3.6.1), interacting via δ-shaped interaction with $V_\delta = 1$, as a function of the lattice depth V_0.

particularly those presented in Ref. [1]. This demonstrates not only the validity but also the versatility and robustness of our approach. By using our novel method for generating WFs, we are able to handle various potential shapes and lattice configurations with high precision. This flexibility makes our method a powerful tool for studying complex lattice systems and their interactions, offering a reliable alternative to more traditional approaches.

3.7 Dynamics of two distinguishable particles in a square double-well potential

As discussed in the previous Sections, the presence of nonstandard Hubbard terms can introduce novel effects in the dynamics of a many-body system, totally non accounted for in the standard Hubbard model description. To analyse these effects further, we consider here the influence of the nonstandard Hubbard terms on the dynamics of two distinguishable particles in the symmetric square double-well potential shown in Fig. 3.2.

3.7.1 Equations of motion and oscillation frequencies of a pair of distinguishable particles

As a figure of merit of the system's dynamics, we consider the oscillation frequency of the time-dependent probability $P_{LL}(t)$, defined as the occupation probability to find both particles in the left well at time t. To evaluate it, let us consider the Hamiltonian given in Eq. (3.4.1), and the δ-shaped two-particle interaction given in Eq. (3.5.1). The two-particle wave function, at time t, can be written as

$$\begin{aligned} |\Psi(t)\rangle = \Big[& b_{LL}(t)\hat{a}_L^{\dagger(1)}\hat{a}_L^{\dagger(2)} + b_{LR}(t)\hat{a}_L^{\dagger(1)}\hat{a}_R^{\dagger(2)} + \\ & + b_{RL}(t)\hat{a}_R^{\dagger(1)}\hat{a}_L^{\dagger(2)} + b_{RR}(t)\hat{a}_R^{\dagger(1)}\hat{a}_R^{\dagger(2)}\Big] |0\rangle \ , \end{aligned} \tag{3.7.1}$$

where $\hat{a}_{L,R}^{(\dagger)(1,2)}$ are the annihilation (creation) operators for the first/second particle in the left/right well, respectively, and $|0\rangle$ is the single-well vacuum state. The time-evolution of the two-particle wave function in Eq. (3.7.1) is given by the Schrödinger equation

$$i\partial_t |\Psi(t)\rangle = \hat{H} |\Psi(t)\rangle \ .$$

Considering $b_{LR}(t) = b_{RL}(t)$ (due to the potential symmetry), we can derive the equations of motion for the so called *SB nonstandard model*, which include all the nonstandard interaction terms, which read

$$\begin{cases} i\dot{b}_{LL}(t) = (2E_0 + U)\, b_{LL}(t) + \Omega_{eff} b_{LR}(t) + \Omega_2 b_{RR}(t) \\ i\dot{b}_{RR}(t) = (2E_0 + U)\, b_{RR}(t) + \Omega_{eff} b_{LR}(t) + \Omega_2 b_{LL}(t) \\ i\dot{b}_{LR}(t) = 2E_0 b_{LR}(t) + \Omega_{eff}\left[b_{LL}(t) + b_{RR}(t)\right] \end{cases} , \tag{3.7.2}$$

where E_0 is the single-well ground state energy, U is the on-site standard Hubbard term given by Eq. (3.4.4),

$$\Omega_{eff} = \Omega_0 + \Omega_1$$

is the effective tunneling coupling given by Eq. (3.5.5) and Ω_2 is the PT amplitude given by Eq. (3.4.7b). The equations of motion for the standard Hubbard model can be straightforwardly obtained from Eqs. (3.7.2) by simply setting $\Omega_1 = \Omega_2 = 0$:

$$\begin{cases} i\dot{b}_{LL}(t) = (2E_0 + U)\, b_{LL}(t) + \Omega_0 b_{LR}(t) \\ i\dot{b}_{RR}(t) = (2E_0 + U)\, b_{RR}(t) + \Omega_0 b_{LR}(t) \\ i\dot{b}_{LR}(t) = 2E_0 b_{LR}(t) + \Omega_0 \left[b_{LL}(t) + b_{RR}(t) \right] \end{cases} . \tag{3.7.3}$$

As initial state for the dynamics, we consider both particles placed in the infinite left-well state

$$\langle x|\Phi(x)\rangle_L = \sqrt{\frac{2}{L}} sin \left[\frac{\pi\,(x + L + b/2)}{L} \right] .$$

Therefore, the initial conditions for the equations of motion of Eqs. (3.7.2) and Eqs. (3.7.3) are $b_{LL}(0) = 1$ and $b_{LR}(0) = b_{RL}(0) = b_{RR}(0) = 0$. Finally, we can compute the time-dependent occupation probability $P_{LL}(t)$ for the state

$$|LL\rangle \equiv \hat{a}_L^{\dagger(1)} \hat{a}_L^{\dagger(2)} |00\rangle .$$

The system's parameters have been chosen in such a way to have four bound energies in the double-well system (for further details, see Appendix F).

3.7.2 Frequencies of dynamics processes and discussion

In Fig. 3.6, we show the probability $P_{LL}(t)$ to find the two particles in the left well, for two different attractive interaction strengths, respectively in the weakly interacting regime (Fig. 3.6(a)) and in the strongly interacting regime (Fig. 3.6(b)). Similar results can be obtained for the case of repulsive interaction strength and are reported in Appendix F. Specifically, we compute the occupation probability $P_{LL}(t)$ by employing four different models: the standard Hubbard model, the SB nonstandard model, the MB nonstandard model and the *no-PT* model. While the standard Hubbard model serves as a reference, the other three models include novel effects given by the exact treatment of the interaction. In particular, the SB nonstandard model considers only the effect of the lowest energy band, neglecting contributions from higher energy bands. On the other hand, the MB nonstandard model fully accounts for the influence of all energy bands, see Ch. 2. Moreover, we introduce the *no-PT* model, to highlight the importance of the PT process itself, by artificially excluding its contribution from the dynamics of the SB nonstandard model.

We note that, for both weakly and strongly interacting regimes, the expected frequency of oscillation of $P_{LL}(t)$ from the standard Hubbard model (yellow

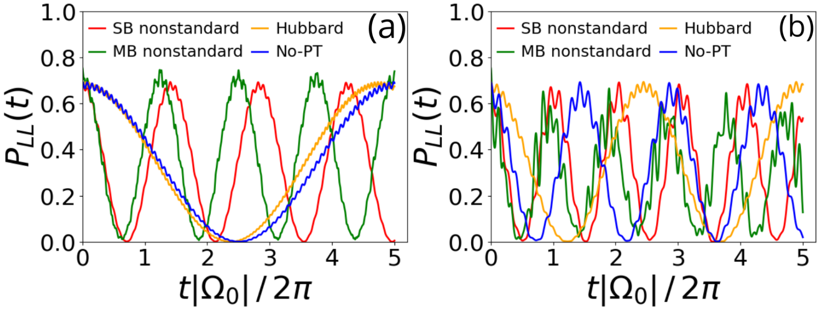

Figure 3.6: Time-evolution of the probability $P_{LL}(t)$ of finding at time t two distinguishable particles together in the left well of the symmetric square double-well potential of Fig. 3.2. The particles are interacting via δ-shaped interaction potential. The different models are: Hubbard model (orange curve), MB nonstandard model (green curve), SB nonstandard model (red curve) and no-PT model (blue curve). The double-well parameters are $L = 2$, $b = 0.5$ and $V_0 = 5$. The attractive interaction strengths are: $U/|\Omega_0| \simeq -6$ (weakly interacting regime) in panel (a) and $U/|\Omega_0| \simeq -12$ (strongly interacting regime) in panel (b).

curve) is smaller than the one obtained from the SB and MB nonstandard models (respectively red and green curves). This highlights the role of the exact treatment of interaction in the system's dynamics, justifying the inclusion of the nonstandard terms in the system's Hamiltonian. Specifically, we note that for weakly interacting regime, the frequency is closer to the SB nonstandard model one, being the nonstandard term less relevant in the dynamics, compared to the strongly interacting regime. We also note that, for the strongly interacting regime, see Fig. 3.6(b), the no-PT model matches quite well the Hubbard model predictions. This puts in evidence the role (and the importance) of PT in the strongly interacting regime. Finally, we appreciate the difference between SB and MB nonstandard models, given by the different number of energy levels included in the dynamics, especially in the strongly interacting regime (the excitation probability for the higher levels is increased).

To understand how the different tunneling processes affect the global system's dynamics, and how the two frequencies Ω_{eff} and Ω_2 (interaction-dependent) act on the dynamics, we extracted the dominant frequency of the probability $P_{LL}(t)$ for different values of interaction strengths, both attractive and repulsive. Specifically, this has been obtained by taking the frequency corresponding to the largest amplitude in the Fourier spectrum of $P_{LL}(t)$. In Fig. 3.7, we represent the dominant frequency of $P_{LL}(t)$ as a function of the interaction strength

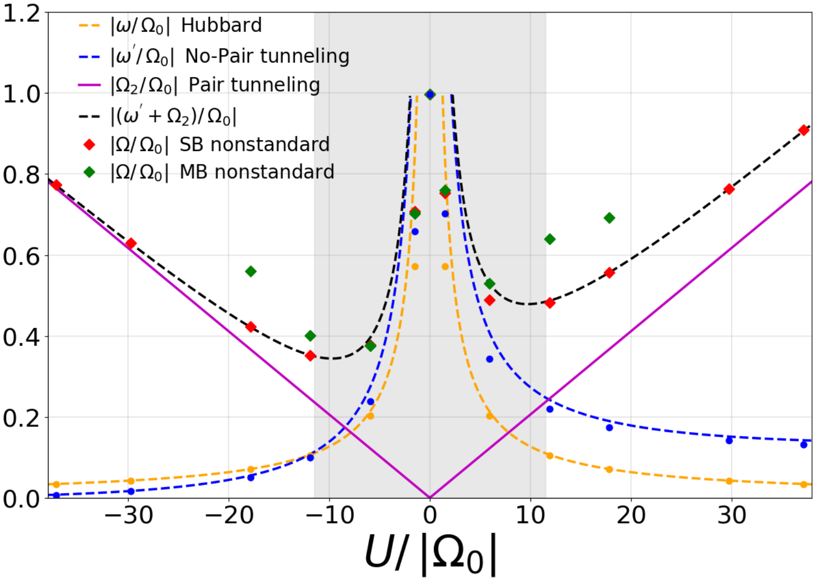

Figure 3.7: Frequencies of the different processes involved in the system's dynamics. Standard Hubbard model cotunneling $\omega = 2\Omega_0^2/|U|$ (orange dashed curve), no-PT model $\omega' = 2\Omega_{eff}^2/|U|$ (blue dashed curve), PT Ω_2 (purple curve). Orange and blue dots stand for the Hubbard model and no-PT model, respectively, extracted from our simulations. Frequency of the SB nonstandard model for $P_{LL}(t)$, computed via Fourier transform (red diamonds). Frequency of the MB nonstandard model (four energy levels in total) for $P_{LL}(t)$, computed via Fourier transform (green diamonds). Black dashed curve: $\Omega = \omega' + \Omega_2$. The parameters of the double-well system are: $L = 2$, $b = 0.5$, $V_0 = 5$. With these parameters, $\Omega_0 \simeq 0.22$, $|\Omega_1/U| \simeq 0.017$, $|\Omega_2/U| \simeq 0.02$ (DT and PT result both relevant in the dynamics).

$U/|\Omega_0|$. Looking at Fig. 3.7, we clearly distinguish three different regimes: for a strongly enough interacting regime $|U| \gg \Omega_0$, both attractive and repulsive, the dynamics is completely dominated by the PT process (purple line). Indeed, while the frequency $\omega = 2\Omega_0^2/U$ predicted by the standard Hubbard model (orange curve) decreases linearly with the on-site standard Hubbard interaction U (and consequently with V_δ), the frequency Ω_2 increases linearly with it. For this reason, in the strongly interacting regime the PT process becomes predominant. By contrast, in the weakly interacting regime $|U| \ll \Omega_0$, the SB nonstandard (and MB nonstandard) model dynamics is very well approximated by the standard Hubbard model, which takes into account only single-particle tunneling processes. In this weakly interacting regime, the Hubbard model proves to be a good approximation for the system's dynamics.

Finally, we can distinguish an intermediate regime of interaction where both processes (cotunneling and PT) are equally involved in the dynamics. We note that the expected frequency of the SB nonstandard model corresponds to the sum of the two contributions: $\Omega = \omega' + \Omega_2$ (black dashed curve), where

$$\omega' = \frac{2\left(\Omega_{eff}\right)^2}{|U|}\,.$$

Finally, the vertical gray band in Fig. 3.7 corresponds to the case $|U|= \Delta E$, where the Hubbard term U matches the mean level spacing ΔE of the double-well potential (taken as the distance in energy between the second excited state and the average of the ground state and first excited state of the double-well system). In this particular case, the interparticle interaction is strong enough to excite the higher energy levels, making them play a relevant role in the system's dynamics. Therefore, the SB approximation is no more valid, and the contribution given by the higher energy levels must be included in the physical description through the MB nonstandard model. As clearly visible in Fig. 3.7, near the edges of this gray band, the results obtained with the SB nonstandard model start to deviate from the exact ones, obtained via the MB nonstandard model. Indeed, in this case the interaction between particles is sufficiently strong to excite the upper levels of the spectrum that cannot be neglected in the study of the dynamics. Finally, when δ-shaped interaction is adopted in higher dimensions, regularization is necessary, and multiband effects must be included in the scattering process (see Refs. [119, 120].)

3.8 Comparison with experiments: two bosons in a double-well potential

In this Section, our numerical results are compared with the experimental results reported in Ref. [2]. In that work, second-order atom tunneling processes were observed in an interacting ultracold bosonic gas of rubidium atoms placed in an optical double-well potential. It was observed that, under certain conditions, atoms undergo second-order tunneling processes in addition to the usual first-order tunneling expected from the standard Hubbard model. The authors identify a regime where single-particle tunneling is promoted by the presence of other particles (via the DT mechanism) and a PT process also affects the system's dynamics.

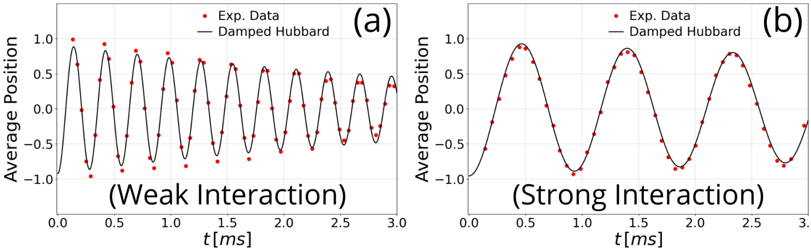

Figure 3.8: Comparison between experimental results of Ref. [2] (red dots), and damped Hubbard model (black curve) for a single boson initially localized in the left well. The parameters used are $A_{long} = 9.5E_R$, $B_{short} = 5.40E_R$, $\Delta \simeq 0.17E_R$ in panel (a) and $A_{long} = 9.5E_R$, $B_{short} = 7.92E_R$, $\Delta \simeq 0.07E_R$ in panel (b). All the energies are expressed in units of the recoil energy $E_R = h^2/2m\lambda^2$, where h is the Planck's constant, $m \simeq 86.9u$ is the mass of the ^{87}Rb atoms and $\lambda = 765\ nm$ is the long-lattice wavelength. The decay times of the damped Hubbard model are: $\tau \simeq 4.38\,ms$ in panel (a) and $\tau \simeq 13\,ms$ in panel (b).

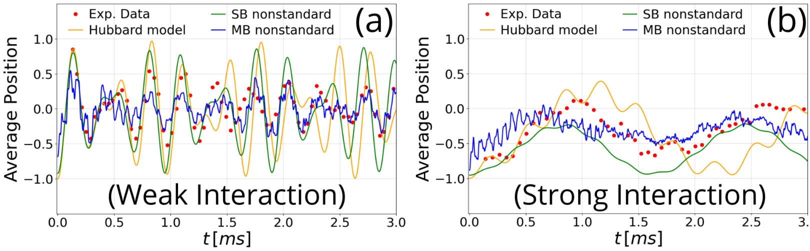

Figure 3.9: Comparison between experimental results of Ref. [2] (red dots), Hubbard model (orange curve), SB nonstandard model (green curve) and MB nonstandard model (blue curve) for two bosons in the weakly interacting regime ($U/J = 0.67$ in panel (a)) and strongly interacting regime ($U/J = 5$ in panel (b)), after initially preparing the system with both particles localized in the left well of the double-well system. The system's parameters are: $V_0 \simeq 22.4E_R$, $\Omega_0 \simeq -0.45E_R$, $\mathcal{E}_1 \simeq -20.3E_R$, $\mathcal{E}_2 \simeq -19.4E_R$ in panel (a) and $V_0 \simeq 26.8E_R$, $\Omega_0 \simeq -0.14E_R$, $\mathcal{E}_1 \simeq -23.5E_R$, $\mathcal{E}_2 \simeq -23.2E_R$ in panel (b).

To compare the experimental outcomes with the results obtained from our approach, we exploit its versatility and robustness, taking advantage of its ability to handle any potential shape, and not just square potentials. This flexibility is crucial for accurately modeling real systems, where, in general, the potential is given by a superposition of two or more optical potentials. From now on, if not stated otherwise, all the energies will be expressed in units of the recoil energy

$$E_R = \frac{h^2}{2m\lambda^2} \,,$$

where λ represents the with of the double-well system. Here, our unit of length $a = \lambda/2 = L + b$ represents the distance between two particles placed in neighboring lattice sites.

In Ref. [2], the authors consider the Bose-Hubbard model as the most simple description of a set of N bosonic atoms in an optical lattice with tunneling coupling $J \equiv \Omega_0$ between nearest neighbor sites and two-body interaction U between particles at the same site. The Hamiltonian that describes this model, considering a bias Δ between neighboring wells, is given by

$$\hat{H}_{BH} = -J \sum_{\langle i,j \rangle} \hat{b}_i^\dagger \hat{b}_j + \frac{U}{2} \sum_i \hat{n}_i \left(\hat{n}_i - 1\right) - \frac{\Delta}{2} \sum_{\langle i,j \rangle} \left(\hat{n}_i - \hat{n}_j\right) \,. \tag{3.8.1}$$

Restricting our considerations to a double-well potential, the bosonic atoms in a double-well potential are described in Ref. [2] by the standard Bose-Hubbard Hamiltonian

$$\begin{aligned} \hat{H}_{BH} = &- J \left(\hat{b}_L^\dagger \hat{b}_R + \hat{b}_R^\dagger \hat{b}_L\right) - \frac{\Delta}{2} \left(\hat{n}_L - \hat{n}_R\right) + \\ &+ \frac{U}{2} \left[\hat{n}_L \left(\hat{n}_L - 1\right) + \hat{n}_R \left(\hat{n}_R - 1\right)\right] \,, \end{aligned} \tag{3.8.2}$$

where J is the single-particle tunneling, $\hat{b}_{L,R}^{(\dagger)}$ are the annihilation (creation) operators for a bosonic particle in the ground state of the left and right well, U is the interaction energy of two particles placed in the same well and Δ is the bias between the potential wells. The double-well potential in Ref. [2] is realized by superimposing two optical periodic potentials, respectively long-lattice and short-lattice periodic potentials, with amplitudes A_{long} and B_{short}, and corresponding wavelengths given by 765.0 nm and 382.5 nm, respectively. The initial state for the dynamics is realized by placing one (or more) atoms in the left well. The sudden lowering of the potential barrier depth gives rise to the dynamics of the particle(s). As a figure of merit for the system's dynamics, the average position is considered:

$$\langle x(t) \rangle = \frac{\langle \hat{n}_R(t) \rangle - \langle \hat{n}_L(t) \rangle}{\langle \hat{n}_R(t) \rangle + \langle \hat{n}_L(t) \rangle} \,, \tag{3.8.3}$$

where $\hat{n}_{L,R}$ is the number of bosons placed in the left (L) and right (R) well, respectively. Moreover, the dynamics of a single boson (single-particle signal) and of a pair of bosons (double-particle signal), for different interaction regimes, have been experimentally measured. Specifically, weakly ($U/J = 0.67$) and strongly ($U/J = 5$) interacting regimes have been considered. Note that, even in the single-particle case, the ratio U/J can be defined, since the single-particle signal is obtained by subtracting the double-particle signal from the total signal (for further details, see Ref. [2]). One may wonder what occurs in the parameter range between the weakly and strongly interacting regimes considered in Fig. 3.9. According to the experimental conditions outlined in Ref. [2], increasing the Hubbard interaction term U also increases the lattice depth V_0, which in turn reduces the relative influence of the PT term. This issue is discussed in detail in Appendix G, where it is also shown that the DT term becomes relevant in determining the parameter value at which the metal-insulator transition occurs.

In addition, our numerical model can be defined as a generalized lowest-band Hubbard Hamiltonian, which reads

$$\begin{aligned}\hat{H} = &- J\left(\hat{b}_L^\dagger \hat{b}_R + \hat{b}_R^\dagger \hat{b}_L\right) - \frac{\Delta}{2}\left(\hat{n}_L - \hat{n}_R\right) + \\ &+ \frac{U}{2}\left[\hat{n}_L\left(\hat{n}_L - 1\right) + \hat{n}_R\left(\hat{n}_R - 1\right)\right] + \overline{U}\left(\hat{n}_L \hat{n}_R\right) + \\ &+ \Omega_1\left(\hat{b}_L^\dagger\left(\hat{n}_L + \hat{n}_R\right)\hat{b}_R + \hat{b}_R^\dagger\left(\hat{n}_R + \hat{n}_L\right)\hat{b}_L\right) + \\ &+ \Omega_2\left(\hat{b}_L^{\dagger 2}\hat{b}_R^2 + \hat{b}_R^{\dagger 2}\hat{b}_L^2\right) ,\end{aligned} \tag{3.8.4}$$

where $\overline{U}$ represents the nearest neighbor interaction, Ω_1 is the DT term and Ω_2 is the PT term. For the case of single-particle dynamics, we modify both the amplitude B_{short} of the short-lattice periodic potential and the bias Δ between the wells, in order to adjust the single-particle tunneling Ω_0. We also introduce a phenomenological exponential damping in our model, to fit the experimental conditions. Specifically, we fit the bare model $M(t)$ with the function

$$D(t) = M(t)e^{-\gamma t} ,$$

where γ represents the inverse decay time, and it is used as a free fitting parameter. The results for the dynamics of a single boson are presented in Fig. 3.8, both for weakly and strongly interacting regime. Here, the damped Hubbard model (black curve) fits very well the experimental data (red dots), matching the single-particle oscillation frequency. Specifically, in Fig. 3.8(a), we obtain a parameter $\gamma = 0.2285\, ms^{-1}$, which corresponds to a decay time $\tau \simeq 4.38\, ms$ close to the decay time $\tau = 3.5\, ms$ obtained in Ref. [2].

The average position of two interacting bosons, initially placed in the infinite left-well state, respectively in the case of weakly ($U/J = 0.67$) and strongly

$(U/J = 5)$ interacting regime, is shown in Fig. 3.9. Here, we represent the experimental data (red dots), the Hubbard model (orange curve), the SB nonstandard model (green curve) and the MB nonstandard model (blue curve). We note that the Hubbard model does not reproduce exactly the experimental results, both in terms of amplitude and frequency of oscillation, for weakly and strongly interacting regimes. Moreover, for the parameters chosen in the experiments, also the SB nonstandard model does not agree completely with the experimental results. On the contrary, the MB nonstandard model is able to fit better the experimental data, both in the weakly and strongly interacting regimes, since it considers all the possible energy levels involved in the system's dynamics. Comparing Fig. 3.9(a) with Fig. 3.9(b), we note that SB nonstandard and MB nonstandard models approximate better the experimental data for the weakly interacting regime, with respect to the strongly interacting one. This highlights the importance of including higher energy levels for the case of strongly interacting regime, to accurately capture the complex dynamics of strongly interacting bosonic systems. Even if our results do not exactly match the experimental data, they still highlight a significant improvement in the description of the system's dynamics compared to the standard Hubbard model.

3.9 Discussion

In conclusion, our comprehensive study of many-body tunneling dynamics in arbitrary double-well potentials significantly advances the understanding of interacting many-body systems beyond the conventional approximations of the standard Hubbard model. By incorporating nonstandard Hubbard terms in the Hamiltonian, specifically DT and PT terms, we identify crucial modifications to the system's behavior that are not captured by the standard Hubbard model. Specifically, in the presence of a δ-shaped repulsive interparticle interaction, our perturbative analytical approximations, corroborated by extensive numerical simulations, reveal that these additional terms fundamentally modify the single-particle tunneling parameter Ω_0 and introduce new coherent propagation mechanisms, given by the PT process. These findings may have important implications for a broad range of physical phenomena, including high-T_C superconductivity [13–18, 109–112, 121] and metal-insulator transitions [54, 102, 103, 113, 122].

We show that the nonstandard Hubbard model significantly deviates from the standard Hubbard model with increasing interaction strength, resulting in different transport behaviors. In the nonstandard model, strong interactions modify single-particle tunneling and enhancing PT, generating an interplay that may give rise to novel transport phenomena. However, at lower interaction strengths, the two models produce similar outcomes, particularly when DY and PT terms are minimal compared to Ω_0.

Our theoretical framework has been also validated by experimental observations of second-order atom tunneling in optical double-well arrays, demonstrating the practical relevance and applicability of our model. The excellent agreement between our numerical simulations and the computed lowest-band parameters further underscores the robustness and accuracy of our approach. Overall, this work not only highlights the necessity of considering nonstandard Hubbard terms in the study of many-body systems, but also provides insights into the complex interplay between interaction and tunneling processes in quantum systems. These findings pave the way for future investigations into complex quantum behaviour and emergent phenomena in controlled experimental setups.

From a broader perspective, the results of this study open new paths for exploring exotic quantum states and novel phases of matter in various physical systems. By challenging and extending the boundaries of the Hubbard model, our work suggests a re-evaluation of theoretical frameworks that describe strongly correlated materials. This can potentially lead to the discovery of new materials with unique properties, thereby impacting the fields of condensed matter physics. Additionally, the methods developed here could inspire advancements in quantum simulation and computation, where precise control and understanding of tunneling dynamics are crucial. As such, our findings not only improve the theoretical understanding of many-body quantum systems, but also have far-reaching implications for future experimental and technological developments.

Chapter 4

Conclusions and outlook

The journey through this thesis has been a rigorous and comprehensive exploration of both the limitations and extensions of the Hubbard model in describing strongly correlated electron systems. Our primary focus was to develop a comprehensive framework that addresses the shortcomings of the standard Hubbard model, particularly its inability to account for certain interaction-induced phenomena observed in experiments, such as those in ultracold atom systems and condensed matter systems like twisted bilayer graphene.

To this end, we extended the traditional Hubbard model by incorporating crucial interaction terms, resulting in both single-band (SB) and multiband (MB) nonstandard Hubbard models. These models include essential terms such as density-induced tunneling (DT) and pair tunneling (PT), offering a significant improvement in the theoretical understanding of strongly correlated systems.

A major innovation in our approach was the development of a novel method for evaluating Wannier functions (WFs). Unlike traditional approaches that often overlook the tails of WFs, our method accounts for their full spatial extent, significantly improing the accuracy of interaction matrix elements. This was achieved through a perturbative approach, using the barrier penetration coefficient as a perturbation parameter, overcoming the limitations of the widely used maximally localized Wannier functions (MLWFs). Our method allows a more precise determination of the nonstandard interaction terms in the Hubbard Hamiltonian.

Applying this improved evaluation of WFs, we derived a nonstandard Hubbard Hamiltonian that includes not only the standard kinetic and on-site interaction terms, but also the additional DT and PT terms. Our analysis revealed that these nonstandard terms lead to significant deviations from the predictions of the standard Hubbard model. For example, long-range interparticle interactions can suppress single-particle tunneling, countering the insulating behavior predicted by the standard model. This suppression allows for the coherent motion of particle pairs, even in the absence of attractive interactions, suggesting a mechanism for repulsive particle pairing that resists decay from single-electron tunneling transitions.

We tested our theoretical model using potential profiles like square double-well and sinusoidal potentials, which reflect experimental conditions in optical lattices. The predictions of our nonstandard Hubbard model matched well with experimental data, confirming the model's accuracy and robustness.

The insights gained from this work have far-reaching implications for understanding and controlling complex quantum materials with unique electronic properties. DT and PT mechanisms could play critical roles in developing superconducting materials, particularly in unconventional systems like twisted bilayer graphene. The nonstandard Hubbard model, incorporating DT and PT, provides a powerful tool for investigating new material properties and electronic behaviors, shedding light on phenomena like superconductivity and metal-insulator transitions. These findings also suggest new pathways for manipulating metal-insulator transitions in correlated systems, with potential technological applications.

Beyond the systems analyzed here, our work has broader implications in the field of quantum transport. Many-body tunneling processes, such as those governed by DT and PT, could significantly improve quantum transport of electrons, especially in one-dimensional systems like atomic chains or quantum wires. In these low-dimensional systems, where interactions are amplified, many-body tunneling can promote more coherent charge transport by reducing dissipation and suppressing single-electron tunneling. This could lead to controlled electron flow with unprecedented precision, paving the way for developing materials with tailored electronic properties for high-performance quantum transport applications.

In summary, this thesis has advanced the understanding of many-body systems by addressing the limitations of the standard Hubbard model and proposing an extended and robust framework. The development of the nonstandard Hubbard model, supported by our novel WFs evaluation method, provides a more accurate description of interacting many-body systems. This work offers a solid foundation for future research into complex quantum phenomena and serves as a useful tool for both theoretical and experimental investigations in condensed matter physics. The successful alignment of theoretical predictions with experimental data highlights the robustness of this approach, marking a significant contribution to the field.

Looking beyond the systems studied here, this thesis opens new pathways for exploring and controlling quantum materials. By bridging the gap between theory and experiment, it contributes to a more unified understanding of condensed matter systems, with potential applications in materials science, quantum computing, and beyond.

Appendix A

Exact equations of motion of two electrons in a symmetric triple-well potential

A.1 Wannier functions of a symmetric triple-well potential

In this Appendix, we consider the triple-well potential $\mathcal{V}(x)$ depicted in Fig. 2.2(b), where the lowest band is composed of three eigenstates $\psi_k(x)$, indexed by $k = 1, 2, 3$ as described in Eq. (2.2.2). These eigenstates correspond to energies $\mathcal{E}_k$, with $\mathcal{E}_1 < \mathcal{E}_2 < \mathcal{E}_3 < 0$. We derive the tunneling Hamiltonian $\hat{H}_3$ for this band, expressed in the basis of Wannier functions $|\Psi_j\rangle$, with $j = 1, 2, 3$ denoting the left, middle, and right wells, respectively. Accounting for the symmetry of $\mathcal{V}(x)$, the tunneling Hamiltonian is given by

$$\begin{aligned}\hat{H}_3 = \overline{E}_0 \left(\hat{a}_L^\dagger \hat{a}_L + \hat{a}_M^\dagger \hat{a}_M + \hat{a}_R^\dagger \hat{a}_R\right) + \\ + \overline{\Omega}_0 \left(\hat{a}_L^\dagger \hat{a}_M + \hat{a}_M^\dagger \hat{a}_R + H.c.\right) + \\ + \overline{\Omega}_0' \left(\hat{a}_L^\dagger \hat{a}_R + H.c.\right) ,\end{aligned} \tag{A.1.1}$$

where $\overline{E}_0$ represents the single-site energy, $\overline{\Omega}_0$ denotes nearest neighbor hopping, and $\overline{\Omega}_0'$ accounts for next-to-nearest neighbor hopping (which is usually disregarded, since it is a higher-order term in the penetration coefficient). In particular, Eq. (A.1.1) constitutes a more general form than the nearest-neighbor Hamiltonian discussed in Eq. (2.2.8). The unitary matrix R, defined up to $\mathcal{O}\left(\overline{\Omega}_0'/\overline{\Omega}_0\right)^2$ terms as

$$R = \begin{pmatrix} \frac{1}{2} & \left(\frac{1}{\sqrt{2}} - \frac{\overline{\Omega}_0'}{4\overline{\Omega}_0}\right) & \frac{1}{2} \\ \frac{1}{\sqrt{2}} & 0 & -\frac{1}{\sqrt{2}} \\ \frac{1}{2} & -\left(\frac{1}{\sqrt{2}} + \frac{\overline{\Omega}_0'}{4\overline{\Omega}_0}\right) & \frac{1}{2} \end{pmatrix}, \tag{A.1.2}$$

diagonalizes $\hat{H}_3$, yielding eigenstates that can be identified with the exact solutions of the Schrödinger equation described in Eq. (2.2.2). Expressing the energies $\mathcal{E}_k$ in terms of $\overline{E}_0$, $\overline{\Omega}_0$ and $\overline{\Omega}_0'$, we get

$$\begin{aligned} \mathcal{E}_{1,3} &= \overline{E}_0 \mp \sqrt{2\overline{\Omega}_0^2 + \left(\frac{\overline{\Omega}_0'}{2}\right)^2} + \frac{\overline{\Omega}_0'}{2}, \\ \mathcal{E}_2 &= \overline{E}_0 - \overline{\Omega}_0'. \end{aligned} \tag{A.1.3}$$

From Eqs. (A.1.3), up to $\mathcal{O}\left(\overline{\Omega}_0'/\overline{\Omega}_0\right)^2$ terms, we get

$$\begin{aligned} \overline{E}_0 &= \frac{\mathcal{E}_1 + \mathcal{E}_2 + \mathcal{E}_3}{3}, \\ \overline{\Omega}_0 &= \frac{\mathcal{E}_1 - \mathcal{E}_3}{2\sqrt{2}}, \\ \overline{\Omega}_0' &= \frac{\mathcal{E}_1 - 2\mathcal{E}_2 + \mathcal{E}_3}{3}. \end{aligned} \tag{A.1.4}$$

Furthermore, the corresponding WFs $\Psi_j(x)$, expressed in terms of the lowest-band eigenstates $\psi_k(x)$ through the unitary transformation detailed in Eq. (A.1.2), are explicitly given by

$$\begin{aligned} \Psi_L(x) &= \frac{1}{2}\psi_1(x) + \left(\frac{1}{\sqrt{2}} - \frac{\overline{\Omega}_0'}{4\overline{\Omega}_0}\right)\psi_2(x) + \frac{1}{2}\psi_3(x), \\ \Psi_M(x) &= \frac{1}{\sqrt{2}}\left[\psi_1(x) - \psi_3(x)\right], \\ \Psi_R(x) &= \frac{1}{2}\psi_1(x) - \left(\frac{1}{\sqrt{2}} + \frac{\overline{\Omega}_0'}{4\overline{\Omega}_0}\right)\psi_2(x) + \frac{1}{2}\psi_3(x). \end{aligned} \tag{A.1.5}$$

By neglecting $\mathcal{O}\left(\overline{\Omega}_0'/\overline{\Omega}_0\right)$ terms, Eqs. (A.1.4) and (A.1.5) coincide with Eqs. (2.2.9).

A.2 Two electrons with parallel spins in a triple-well potential

Moving on, the two-electron interacting term $\hat{V}$, described in Eq. (2.5.1), is expressed in second quantization formalism as

$$\begin{aligned}\hat{V} = \overline{U}\left(\hat{n}_L\hat{n}_M + \hat{n}_M\hat{n}_R\right) + \overline{U}'\hat{n}_L\hat{n}_R + \\ + \Omega_1\left(\hat{n}_L\hat{a}_M^\dagger\hat{a}_R + \hat{n}_R\hat{a}_M^\dagger\hat{a}_L + H.c.\right) + \\ - \Omega_2\left(\hat{n}_M\hat{a}_L^\dagger\hat{a}_R + H.c.\right)\,,\end{aligned} \tag{A.2.1}$$

where $\overline{U}$ denotes interaction between nearest neighbor sites, see Eq. (2.5.11), $\overline{U}'$ represents interaction between next-to-nearest neighbor sites, defined as

$$\overline{U}' = \int \Psi_L^2(x)V(x-y)\Psi_R^2(y)\,dx\,dy\,, \tag{A.2.2}$$

and Ω_1 and Ω_2 characterize the DT and PT processes, respectively, see Eqs. (2.5.12).

Now, considering two electrons with parallel spins in the triple-well system, the total time-dependent wave function $|\Psi^{(\bar{j}\bar{j}')}(t)\rangle$ can be written as

$$|\Psi\rangle = \left[b_{LM}\hat{a}_L^\dagger\hat{a}_M^\dagger + b_{LR}\hat{a}_L^\dagger\hat{a}_R^\dagger + b_{MR}\hat{a}_M^\dagger\hat{a}_R^\dagger\right]|0\rangle\,, \tag{A.2.3}$$

omitting both the upper indices (LM), which denote the initial occupation of the system, and the time dependency. Substituting Eq. (A.2.3) into the time-dependent Schrödinger Eq. (2.5.15), considering $\hat{H}_3$ and $\hat{V}$ as described in Eqs. (A.1.1) and (A.2.1), and applying the anti-commutation relations for the Fermi operators

$$\{\hat{a}_j^\dagger\hat{a}_{j'}\} = \delta_{jj'}\,, \quad \{\hat{a}_j^\dagger\hat{a}_{j'}^\dagger\} = \{\hat{a}_j\hat{a}_{j'}\} = 0\,,$$

we derive

$$\begin{aligned}\hat{H}_3\left|\Psi\right\rangle &= \hat{H}_3\left[b_{LM}\hat{a}^\dagger_L\hat{a}^\dagger_M + b_{LR}\hat{a}^\dagger_L\hat{a}^\dagger_R + b_{MR}\hat{a}^\dagger_M\hat{a}^\dagger_R\right]\left|0\right\rangle = \\ &= 2\overline{E}_0\left[b_{LM}\hat{a}^\dagger_L\hat{a}^\dagger_M + b_{LR}\hat{a}^\dagger_L\hat{a}^\dagger_R + b_{MR}\hat{a}^\dagger_M\hat{a}^\dagger_R\right]\left|0\right\rangle + \\ &+ \overline{\Omega}_0\left[b_{LM}\hat{a}^\dagger_L\hat{a}^\dagger_R + b_{LR}\left(\hat{a}^\dagger_L\hat{a}^\dagger_M + \hat{a}^\dagger_M\hat{a}^\dagger_R\right) + b_{MR}\hat{a}^\dagger_L\hat{a}^\dagger_R\right]\left|0\right\rangle + \\ &- \overline{\Omega}'_0\left[b_{LM}\hat{a}^\dagger_M\hat{a}^\dagger_R + b_{MR}\hat{a}^\dagger_L\hat{a}^\dagger_M\right]\left|0\right\rangle\,,\end{aligned} \tag{A.2.4}$$

as well as

$$\begin{aligned}\hat{V}\left|\Psi\right\rangle &= \hat{V}\left[b_{LM}\hat{a}^\dagger_L\hat{a}^\dagger_M + b_{LR}\hat{a}^\dagger_L\hat{a}^\dagger_R + b_{MR}\hat{a}^\dagger_M\hat{a}^\dagger_R\right]\left|0\right\rangle = \\ &= \overline{U}\left[b_{LM}\hat{a}^\dagger_L\hat{a}^\dagger_M + b^{(LR)}_{MR}\hat{a}^\dagger_M\hat{a}^\dagger_R\right]\left|0\right\rangle + \overline{U}'\left[b_{LR}\hat{a}^\dagger_L\hat{a}^\dagger_R\right]\left|0\right\rangle + \\ &+ \Omega_1\left[b_{LM}\hat{a}^\dagger_L\hat{a}^\dagger_R + b_{LR}\left(\hat{a}^\dagger_L\hat{a}^\dagger_M + \hat{a}^\dagger_M\hat{a}^\dagger_R\right) + \right. \\ &\left. + b_{MR}\hat{a}^\dagger_L\hat{a}^\dagger_R\right]\left|0\right\rangle + \Omega_2\left[b_{LM}\hat{a}^\dagger_M\hat{a}^\dagger_R + b_{MR}\hat{a}^\dagger_L\hat{a}^\dagger_M\right]\left|0\right\rangle\,.\end{aligned} \tag{A.2.5}$$

Therefore, the resulting equations of motion are:

$$\begin{aligned}i\dot{b}_{LM}(t) &= \left(2E_0 + \overline{U}\right)b_{LM}(t) + \\ &\quad + \left(\overline{\Omega}_0 + \Omega_1\right)b_{LR}(t) + \left(-\overline{\Omega}'_0 + \Omega_2\right)b_{MR}(t)\,, \\ i\dot{b}_{LR}(t) &= \left(2E_0 + \overline{U}'\right)b_{LR}(t) + \\ &\quad + \left(\overline{\Omega}_0 + \Omega_1\right)\left[b_{LM}(t) + b_{MR}(t)\right]\,, \\ i\dot{b}_{MR}(t) &= \left(2E_0 + \overline{U}\right)b_{MR}(t) + \\ &\quad + \left(\overline{\Omega}_0 + \Omega_1\right)b_{LR}(t) + \left(-\overline{\Omega}'_0 + \Omega_2\right)b_{LM}(t)\,.\end{aligned} \tag{A.2.6}$$

Notably, neglecting $\mathcal{O}\left(\overline{\Omega}'_0/\overline{\Omega}_0\right)$ and $\mathcal{O}\left(\overline{U}'/\overline{U}\right)$ terms, which are respectively next-to-nearest neighbor contributions to free and interacting dynamics, Eqs. (A.2.6) coincide with Eqs. (2.5.16). Finally, we investigate the effect of the interaction range $\overline{d}$ on the three terms $\overline{U}'$, Ω_1, and Ω_2 in Fig. A.1. Here, we keep the same geometries and interactions of Figs. 2.5(b) and 2.5(c)

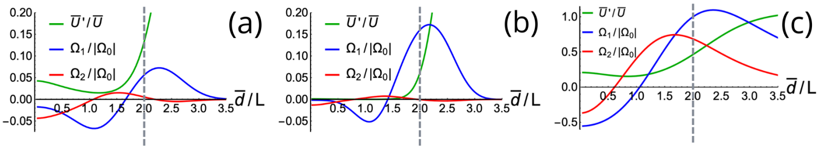

Figure A.1: Next-to-nearest neighbor interaction normalized by the nearest neighbor interaction $\overline{U}'/\overline{U}$ (green curves), DT amplitude normalized by the single-particle tunneling $\Omega_1/|\Omega_0|$ (blue curves) and PT amplitude normalized by the single-particle tunneling $\Omega_2/|\Omega_0|$ (red curves) as a function of the interaction range $\overline{d}$, for the three different geometries of the square triple-well potential presented in Figs. 2.5(b) and 2.5(c) and Fig. 2.6, respectively. (a) Parameters: $L = 2$, $b = 0.5$, $V_0 = 5$ and $\Omega_0 \simeq -0.22$. Interaction strength $V_\delta = 3$. (b) Parameters: $L = 4$, $b = 1$, $V_0 = 5$ and $\Omega_0 \simeq -0.0167$. Interaction strength $V_\delta = 3$. (c) Parameters: $L = 2$, $b = 0.1$, $V_0 = 1.1$ and $\Omega_0 \simeq -0.32$. Interaction strength $V_\delta = 22$. Energies are given in arbitrary units, where Ω_0 sets the characteristic energy scale. Vertical dashed lines represent the interaction range $\overline{d}/L = 2$, common to all panels.

and Fig. 2.6, respectively. It is evident that in Figs. A.1(a) and A.1(b) the term $\overline{U}'/U$ is negligible, while in Fig. A.1(c) it starts to be relevant for the chosen interaction range. Despite that, it does not qualitatively affects the dynamics of the probabilities, confirming the validity of our approximation for the parameters considered in Fig. (2.6). Finally, the behavior of the DT and PT amplitudes, denoted as Ω_1 and Ω_2 respectively, mirrors that observed in the double-well scenario illustrated in Fig. 2.4. Specifically, the DT term becomes positive for a sufficiently large interaction range, such that the chosen interaction strength makes $\Omega_1 \simeq -\Omega_0$, confirming our hypothesis of single-particle tunneling suppression.

Appendix B

Two-potential approach to the bound-state spectrum and the Bardeen formula

B.1 The two-potential approach

The standard perturbation approach consists in separating the total Hamiltonian $\mathcal{H}$ of an entire system into an "unperturbed"Hamiltonian and a "perturbation". In this Appendix, we consider the symmetric double-well potential in Fig. 2.1(a), choosing

$$\mathcal{H} = H_1 + \mathcal{V}_2 \,,$$

where

$$H_1 = \mathcal{K} + \mathcal{V}_1$$

is the left-well Hamiltonian and

$$\mathcal{V}_2(x) = \mathcal{V}_1(-x)$$

is the right-well potential ($\mathcal{K} = -\nabla^2/2m$ is the kinetic part). Such a separation implies that the spectrum of the unperturbed left-well Hamiltonian,

$$H_1 \left|\Phi_n^{(1)}\right\rangle = E_n^{(1)} \left|\Phi_n^{(1)}\right\rangle \,, \tag{B.1.1}$$

must be known (here $E_n^{(1)}$ denotes discrete and continuum spectrum states). The total Hamiltonian spectrum

$$\mathcal{H} \left|\psi_n\right\rangle = E_n \left|\psi_n\right\rangle$$

can be obtained by solving the following equations [123]

$$E_n = E_n^{(1)} + \langle\Phi_n^{(1)}|\mathcal{V}_2|\Phi_n^{(1)}\rangle + \langle\Phi_n^{(1)}|\mathcal{V}_2\,\widetilde{G}(E_n)\,\mathcal{V}_2|\Phi_n^{(1)}\rangle\ , \tag{B.1.2a}$$

$$|\psi_n\rangle = |\Phi_n^{(1)}\rangle + \widetilde{G}(E_n)\,\mathcal{V}_2\,|\Phi_n^{(1)}\rangle\ , \tag{B.1.2b}$$

where

$$\widetilde{G}(E_n) = \left(1 - \Lambda_n^{(1)}\right)(E_n - \mathcal{H})^{-1}$$

represents the total Green's function and

$$\Lambda_n^{(1)} = |\Phi_n^{(1)}\rangle\,\langle\Phi_n^{(1)}|$$

is a projection operator on the state E_n of the Hamiltonian H_1. For simplicity, in the following we will consider the ground state ($n = 0$) of the potential $\mathcal{V}_1$.

The Green's function $\widetilde{G}(E)$ can be obtained directly from the Lippmann-Schwinger equation

$$\widetilde{G}(E) = \left[1 + \widetilde{G}(E)\,\mathcal{V}_2\right]\widetilde{G}_1(E)\,, \tag{B.1.3}$$

where

$$\widetilde{G}_1(E) = \left(1 - \Lambda_0^{(1)}\right)\frac{1}{E - H_1} = \sum_{n\neq 0}\frac{|\Phi_n^{(1)}\rangle\,\langle\Phi_n^{(1)}|}{E - E_n^{(1)}}\,. \tag{B.1.4}$$

By solving Eq. (B.1.2a) with respect to E_n, we find the energy spectrum of the system, while the corresponding eigenstates $|\psi_n\rangle$ are obtained from Eq. (B.1.2b). For the treatment of Eqs. (B.1.2), we use the perturbative expansion obtained by iterating the Lippmann-Schwinger equation in Eq. (B.1.3), namely

$$\widetilde{G}(E) = \widetilde{G}_1 + \widetilde{G}_1\,\mathcal{V}_2\,\widetilde{G}_1 + \widetilde{G}_1\,\mathcal{V}_2\,\widetilde{G}_1\,\mathcal{V}_2\,\widetilde{G}_1 + \dots\,. \tag{B.1.5}$$

Substituting Eq. (B.1.5) into Eqs. (B.1.2), we find the Brillouin-Wigner perturbation series [123] for the energy spectrum of the Hamiltonian $\mathcal{H}$ in powers of the perturbation $\mathcal{V}_2$. In particular, Eq. (B.1.2a) at the second order in $\mathcal{V}_2$, is given by

$$E = E_0^{(1)} + \langle\Phi_0^{(1)}|\mathcal{V}_2|\Phi_0^{(1)}\rangle + \langle\Phi_0^{(1)}|\sum_{n\neq 0}\mathcal{V}_2\frac{|\Phi_n^{(1)}\rangle\,\langle\Phi_n^{(1)}|}{E - E_n^{(1)}}\mathcal{V}_2|\Phi_0^{(1)}\rangle + \mathcal{O}\left(\mathcal{V}_2^3\right)\,. \tag{B.1.6}$$

Looking at Eqs. (B.1.2) and (B.1.5), we notice that the main problem with the perturbative treatment is the absence of a small parameter in the corresponding expansions. At first sight, we could consider the second order perturbation term in $\mathcal{V}_2$, see Eq. (B.1.6), as a small parameter. This term is suppressed because the wave function $\Phi_0^{(1)}(x)$ decreases exponentially for $x > 0$, where $\mathcal{V}_2(x)$ is large, see Fig. 2.1(c). However, the higher order terms of the expansion include an overlap of the potential $\mathcal{V}_2(x)$ with the wave functions $\Phi_n^{(1)}(x)$ of the continuum spectrum, which are not suppressed at all for large $|x|$. This makes the expansion in Eq. (B.1.6) not applicable for evaluating the eigenspectrum of the double-well potential. In general, this is not surprising, since any problem related to tunneling is usually a nonperturbative one.

However, we can use a different treatment of the Green's function $\widetilde{G}(E)$, which leads to a perturbative series in powers of an effectively small expansion parameter. Such a two potential approach was originally developed for tunneling to the continuum in [53, 105–107], and we have extended it to bound-state problems.

Consider the total Green's function $G(E)$ of the double-well system in Fig. 2.1(a). It contains two poles for $E = \mathcal{E}_{1,2}$, corresponding to the two eigenstates of the system with energies close to E_0. Comparing $G(E)$ with

$$\widetilde{G}(E) = \left(1 - \Lambda_0^{(1)}\right) G(E) \,,$$

we observe that the two Green's functions are indeed very similar. The only difference is related to the projection operator $\left(1 - \Lambda_0^{(1)}\right)$, which excludes the ground state $|\Phi_0^{(1)}\rangle$ from the spectral representation. However, the ground state $|\Phi_0^{(2)}\rangle$ of the right well is not excluded by the projection operator. This state would dominate the Green's function behavior at $E \simeq E_0$, making it close to the Green's function

$$G_2(E) = (E - H_2)^{-1}$$

of the second well, which is given by

$$G_2(E) = \frac{|\Phi_0^{(2)}\rangle\,\langle\Phi_0^{(2)}|}{E - E_0} + \sum_{n\neq 0} \frac{|\Phi_n^{(2)}\rangle\,\langle\Phi_n^{(2)}|}{E - E_n^{(2)}} \,. \tag{B.1.7}$$

This suggests a new expansion of the Green's function $\widetilde{G}(E)$ in terms of $G_2(E)$. To find it, we multiply the Lippmann-Schwinger equation (B.1.3) by $(E - H_1)$, thus obtaining

$$\widetilde{G}(E)(E - H_1) = \left[1 + \widetilde{G}(E)\,\mathcal{V}_2\right]\left(1 - \Lambda_0^{(1)}\right) \,.$$

Using

$$E - H_1 \equiv E - H_2 + \mathcal{V}_2 - \mathcal{V}_1 \,,$$

we can write

$$\widetilde{G}(E)(E-H_2)=\widetilde{G}(E)\,(\mathcal{V}_1-\mathcal{V}_2)+\left[1+\widetilde{G}(E)\,\mathcal{V}_2\right]\left(1-\Lambda_0^{(1)}\right)\,. \tag{B.1.8}$$

Multiplying Eq. (B.1.8) by $G_2(E)$, we obtain

$$\widetilde{G}(E)=\left[1+\widetilde{G}(E)\,\mathcal{V}_1\right]G_2(E)-\left[1+\widetilde{G}(E)\,\mathcal{V}_2\right]\Lambda_0^{(1)}G_2(E)\,. \tag{B.1.9}$$

Eq. (B.1.9) shows the exact relation between the Green's function $\widetilde{G}(E)$ and the Green's function of the second well $G_2(E)$ of Eq. (B.1.7). Notice that, in the limit $E \to E_0$,

$$\Lambda_0^{(1)}G_2(E)\overset{E\to E_0}{\Longrightarrow}\beta\,\frac{|\Phi_0^{(1)}\rangle\,\langle\Phi_0^{(2)}|}{E-E_0}\,, \tag{B.1.10}$$

where

$$\beta=\langle\Phi_0^{(1)}|\Phi_0^{(2)}\rangle$$

represents the overlap of the two (nonorthogonal) wave functions of neighboring sites. Since the site wave functions are mainly localized in the respective wells, their overlap $\beta \ll 1$, as can be explicitly shown in the semi-classical limit. Indeed, the left-well orbital function can be written as

$$\Phi_0^{(1)}(x)=\begin{cases}\Phi_0^{(1)}(-\overline{x})\,e^{-\int\limits_{-\overline{x}}^{x}p(x')\,dx'} & \text{for}-\overline{x}<x\leq 0\\ \Phi_0^{(1)}(0)\,e^{-p(0)x} & \text{for}\quad x>0\end{cases}\,, \tag{B.1.11}$$

where

$$p(x)=\sqrt{2m\left(\mathcal{V}_1(x)-E_0\right)}$$

is the (imaginary) momentum under the barrier, so that

$$p(0)=\sqrt{-2mE_0}\,,$$

and $-\overline{x}$ is the classical turning point, with $\mathcal{V}_{1,2}(\mp\overline{x})=E_0$, see Figs. 2.1(b) and 2.1(c). We obtain the same expression for the right-well orbital function $\Phi_0^{(2)}(x)$, under the substitution $x\to -x$ and $\overline{x}\to-\overline{x}$. Therefore, we obtain

$$\begin{aligned}\beta&=2\int\limits_{-\infty}^{0}\Phi_0^{(1)}(x)\Phi_0^{(2)}(x)\,dx\simeq\\ &\simeq\left[\Phi_0^{(1)}(-\overline{x})\right]^2 e^{-\int\limits_{0}^{\overline{x}}p(x')\,dx'}\int\limits_{-\overline{x}}^{0}e^{-\int\limits_{-\overline{x}}^{x}p(x')\,dx'+p(0)x}\,dx\,,\end{aligned} \tag{B.1.12}$$

where we have neglected the integration region $(-\infty, -\overline{x})$, whose contribution is exponentially small. To perform the integration in Eq. (B.1.12), we apply the stationary phase approximation. The stationary point of the variable x is obtained by differentiating the exponential factor, so that

$$-p(x) + p(0) = 0.$$

Solving this equation, we find that the stationary point corresponds to $x = 0$. As a result, the integral over x in Eq. (B.1.12) is given by

$$C \exp\left(-\int\limits_{-\overline{x}}^{0} p(x')\, dx'\right) ,$$

where C is a pre-exponential factor of the stationary phase approximation. Finally, we obtain from Eq. (B.1.12):

$$\beta \simeq 2C \left[\Phi_0^{(1)}(-\overline{x})\right]^2 e^{-\int\limits_{-\overline{x}}^{\overline{x}} p(x')\, dx'} \propto T_0\, , \tag{B.1.13}$$

where T_0 is the barrier penetration coefficient in Eq. (2.3.4). Considering Eq. (B.1.9) in the limit $E \to E_0$, and using Eq. (B.1.7), $\widetilde{G}(E)$ can be written as

$$\begin{aligned} \widetilde{G}(E) = \Big(1 + \widetilde{G}(E)\, \mathcal{V}_1\Big)\, \frac{|\Phi_0^{(2)}\rangle\, \langle\Phi_0^{(2)}|}{E - E_0} + \\ - \beta \Big(1 + \widetilde{G}(E) \mathcal{V}_2\Big)\, \frac{|\Phi_0^{(1)}\rangle\, \langle\Phi_0^{(2)}|}{E - E_0}\, . \end{aligned} \tag{B.1.14}$$

Eq. (B.1.14) can be easily solved for the zero-order term in β, obtaining

$$\widetilde{G}(E) \simeq \frac{|\Phi_0^{(2)}\rangle\, \langle\Phi_0^{(2)}|}{E - E_0 - \overline{\Omega}} + \mathcal{O}\left(\beta\right) , \tag{B.1.15}$$

where

$$\overline{\Omega} = \langle\Phi_0^{(1)}|\mathcal{V}_2|\Phi_0^{(1)}\rangle = \langle\Phi_0^{(2)}|\mathcal{V}_1|\Phi_0^{(2)}\rangle = \int\limits_{-\infty}^{\infty} \left[\Phi_0^{(1)}(x)\right]^2\, \mathcal{V}_2(x)\, dx \tag{B.1.16}$$

is the diagonal energy shift. Since the potential $\mathcal{V}_2(x)$ overlaps with the orbital function tail, see Eq. (B.1.11), $\overline{\Omega} \propto T_0^2 \propto \beta^2$ (c.f. with Eqs. (B.1.12) and (B.1.13)) and therefore it can be neglected.

B.2 The Bardeen formula

Substituting Eq. (B.1.15) into Eq. (B.1.2a), we find that the eigenstate energies of the system $E_\pm$ (up to the $\mathcal{O}\left(\beta^2\right)$ terms) are obtained from the equation

$$E - E_0 = \Omega_0^2/(E - E_0)\,,$$

giving $E_\pm = E_0 \pm \Omega_0$, where

$$\Omega_0 = \langle \Phi_0^{(1)} |\, \mathcal{V}_2 \,| \Phi_0^{(2)} \rangle = \int\limits_0^\infty \Phi_0^{(1)}(x)\, \mathcal{V}_2(x)\, \Phi_0^{(2)}(x)\, dx \tag{B.2.1}$$

is the off-diagonal energy shift, corresponding to the energy split between the two lowest eigenstates,

$$\Omega_0 = (E_+ - E_-)/2\,,$$

and represents the tunneling coupling energy. Notice that $\Omega_0 < 0$, since $\mathcal{V}_2(x) < 0$, see Fig. 2.1. Using the Schrödinger equation

$$\mathcal{V}_2 \,| \Phi_0^{(2)} \rangle = (E_0 - \mathcal{K})\, | \Phi_0^{(2)} \rangle\ ,$$

and

$$\Phi_0^{(1)}(x) = \Phi_0^{(1)}(0) e^{-\sqrt{-2mE_0}x}$$

for $x \geq 0$, we can evaluate the integral in Eq. (B.2.1) by integrating by parts, obtaining

$$\begin{aligned} \Omega_0 &= \int\limits_0^\infty \Phi_0^{(1)}(x) \left(E_0 + \frac{1}{2m} \frac{d^2}{dx^2} \right) \Phi_0^{(2)}(x) = \\ &= \frac{1}{2m} \left[\Phi_0^{(1)\prime}(0) \Phi_0^{(2)}(0) - \Phi_0^{(1)}(0) \Phi_0^{(2)\prime}(0) \right]\,, \end{aligned} \tag{B.2.2}$$

where

$$\Phi_0^{(1,2)\prime}(0) = \frac{d}{dx} \Phi_0^{(1,2)}(x) \bigg|_{x \to 0}\,.$$

This equation represents the Bardeen formula [108], although we use different orbital potentials, namely $\mathcal{V}_{1,2}(x) = 0$ beyond the separation point, see Figs. 2.1(b) and 2.1(c) (c.f. [105–107]). The latter gives us

$$\Phi_0^{(1,2)}(x) = \Phi_0^{(1,2)}(0)\, e^{\mp\sqrt{-2mE_0}x}$$

for $x \gtrless 0$, so that

$$\Phi_0^{(1,2)\prime}(0) = \mp\sqrt{-2mE_0} \Phi_0^{(1,2)}(0)\,.$$

Substituting this result into Eq. (B.2.2), we obtain the following simple expression for the tunneling energy:

$$\Omega_0 = -\sqrt{\frac{2|E_0|}{m}}\Phi_0^{(1)}(0)\Phi_0^{(2)}(0)\,. \tag{B.2.3}$$

Evaluating Eq. (B.2.3) in the semiclassical limit, using Eq. (B.1.11) for the orbital functions, we obtain (c.f. with Eq. (B.1.13))

$$\Omega_0 \simeq -\sqrt{\frac{2|E_0|}{m}}\left[\Phi_0^{(1)}(-\overline{x})\right]^2 e^{-\int\limits_{-\overline{x}}^{\overline{x}} p(x')\,dx'} \propto \beta \propto T_0\,. \tag{B.2.4}$$

Therefore, similarly to the overlap integral β, the tunneling coupling Ω_0 is also proportional to the penetration coefficient T_0. Notice that Eq. (B.2.4) for the tunneling energy Ω_0 was obtained by keeping the first (zero order) term in the expansion of $\widetilde{G}(E)$ in powers of β. The accuracy of Eqs. (B.2.2) and (B.2.3) is therefore up to the terms $\mathcal{O}\left(\beta^2\right)$.

Appendix C

Comparison between the extended and the single-band nonstandard Hubbard model

C.1 Analytical calculations

In this Appendix, we compare the coherent dynamics of two interacting electrons with parallel spins within the symmetric square triple-well potential $\mathcal{V}(x)$ shown in Fig. 2.2(b), using both the extended and the single-band (SB) nonstandard Hubbard model.

For the extended Hubbard model, an analytical expression for the probability $P_{LR}(t)$ can be easily derived. Indeed, from Eqs. (2.5.16) and (2.5.17), setting $\Omega_1 = \Omega_2 = 0$, we obtain:

$$P_{LR}(t) = \frac{4\Omega_0^2}{8\Omega_0^2 + \overline{U}^2} \sin^2 \left[\frac{\sqrt{8\Omega_0^2 + \overline{U}^2}}{2} t \right] . \tag{C.1.1}$$

In Fig. C.1, we illustrate the occupancy probabilities $P_{LM}(t)$ and $P_{LR}(t)$ for the same data as Figs. 2.5(b) and 2.5(c). Each panel in Fig. C.1 shows the dynamics obtained from the SB nonstandard Hubbard model (red curves), the extended Hubbard model (green curves), alongside the analytical results from the TPA (blue curves).

It is evident from Eq. C.1.1 that when $\overline{U} \gg |\Omega_0|$, single-particle tunneling suppression occurs, as shown in Fig. C.1(d). Conversely, for $\overline{U} \sim \Omega_0$, as clearly shown in Fig. C.1(b), no suppression is observed. Actually, the SB nonstandard model and extended Hubbard model display significant discrepancies. For instance, analyzing the corresponding probability $P_{LM}(t)$ reveals that while they provide comparable results for the first geometry, see Fig. C.1(a), a significant frequency shift arises for the second one, see Fig. C.1(c), due to the presence of the term Ω_1, which becomes comparable with Ω_0. More precisely, $\Omega_1/|\Omega_0|= 0.06$ for the first geometry in Figs. C.1(a) and C.1(b), while $\Omega_1/|\Omega_0|= 0.16$ for the second one in Figs. C.1(c) and C.1(d).

C.2 Discussion

Looking at Figs. C.1(b) and C.1(d), one may have the impression that the predictions concerning the $P_{LR}(t)$ for the two Hubbard models are quite similar. To show that this is not always the case, let us consider the scenario where there is exact cancellation ($\Omega_1 = -\Omega_0$), as shown in Figs. C.2(c) and C.2(d) and Fig. 2.6. Looking at Fig. C.2(d), one can see that the extended Hubbard model produces oscillations with a significant amplitude of ≈ 0.13, while the SB nonstandard Hubbard model yields exactly $P_{LR}(t) = 0$. Moreover, the frequency of oscillations of $P_{LM}(t)$ differ notably between the two models, see Fig. C.2(c). Specifically, in the extended Hubbard model, the frequency is approximately given by $\Omega_0^2/\overline{U}$ when $\overline{U} \gg \Omega_0$, whereas in the SB nonstandard Hubbard model, the frequency of oscillations is given by Ω_2.

As the interaction strength decreases, the similarity between the SB nonstandard model and extended Hubbard model is recovered, as shown in Figs. C.2(a) and C.2(b). In such cases, there is no more single-particle tunneling cancellation, and the ratio $\Omega_1/|\Omega_0|$ diminishes significantly (from 1 to 0.02).

Finally, comparing the results obtained with the SB nonstandard Hubbard model to our analytical predictions, we find agreement only when $\Omega_0 \propto \beta \ll 1$, where β represents the orbital overlap, see Figs. C.2(a) and C.2(b). Vice versa, discrepancies between the results arise for large Ω_0, due to the neglected terms of order Ω_0^2 in our analytical approximation, see Figs. C.2(c) and C.2(d).

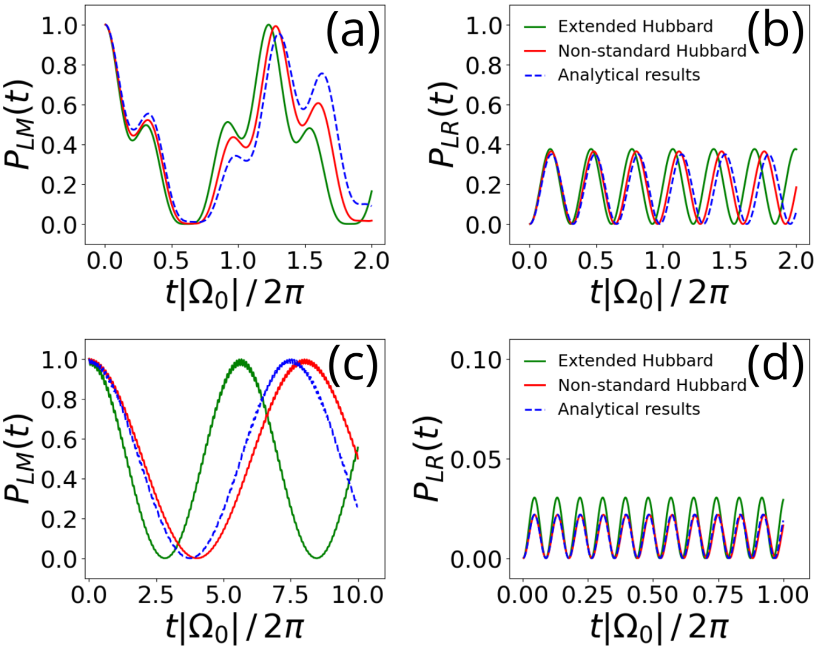

Figure C.1: Occupancy probabilities $P_{LM}(t)$ (left panels) and $P_{LR}(t)$ (right panels) for two electrons with parallel spins in a triple-well potential, when the left and middle well are initially occupied. The different Hamiltonian models are: extended Hubbard model (green curves), SB nonstandard Hubbard model (red curves), analytical results from TPA (blue curves). (a), (b) Same geometry of Fig. 2.5(b), i.e., $L = 2$, $b = 0.5$, $V_0 = 5$ and $\Omega_0 \simeq -0.22$. (c), (d) Same geometry of Fig. 2.5(c), i.e., $L = 4$, $b = 1$, $V_0 = 5$ and $\Omega_0 \simeq -0.0167$. Interaction strength $V_\delta = 3$ and interaction range $\overline{d}/L = 2$, so that $\overline{U} \simeq 0.35$, $\Omega_1 \simeq 0.0125$ and $\Omega_2 \simeq 0.0012$ in (a), (b) and $\overline{U} \simeq 0.19$, $\Omega_1 \simeq 0.0027$ and $\Omega_2 \simeq -6.4 \cdot 10^{-6}$ in (c), (d). Energies are given in arbitrary units, where Ω_0 sets the characteristic energy scale.

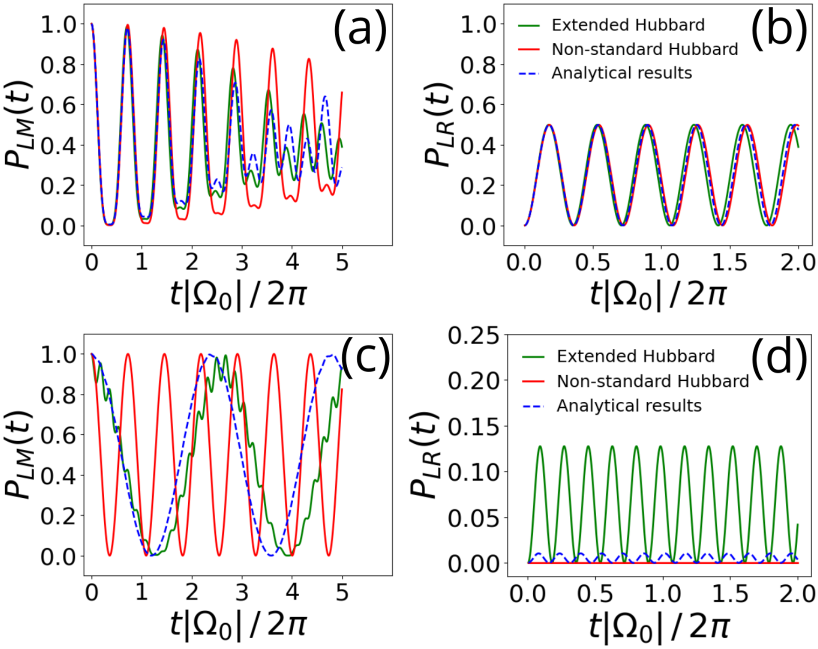

Figure C.2: Occupancy probabilities $P_{LM}(t)$ (left panels) and $P_{LR}(t)$ (right panels) for two electrons with parallel spins in a triple-well potential, when the left and middle well are initially occupied. The different Hamiltonian models are: extended Hubbard model (green curves), SB nonstandard Hubbard model (red curves), analytical results from TPA (blue curves). Same geometry of Fig. 2.6, i.e., $L = 2$, $b = 0.1$, $V_0 = 1.1$ and $\Omega_0 \simeq -0.32$. (a), (b) Interaction strength $V_\delta = 0.5$ and interaction range $\overline{d}/L = 2$, so that $\overline{U} \simeq 0.035$, $\Omega_1 \simeq 0.007$ and $\Omega_2 \simeq 0.005$. (c), (d) Interaction strength $V_\delta = 22$ and interaction range $\overline{d}/L = 2$, so that $\overline{U} \simeq 1.54$, $\Omega_1 \simeq -\Omega_0$ and $\Omega_2 \simeq 0.22$ (complete single-particle tunneling suppression case), in arbitrary units.

Appendix D

Squared sine double-well potential

In this Appendix, we compare the results of our analytical approximated approach (TPA) with the exact numerical evaluation of the WFs $\Psi_j(x)$ for the following squared sine double-well potential, shown in Fig. D.1(a):

$$\mathcal{V}(x) = \begin{cases} -V_0 \sin^2(x) & \text{for} \quad |x| \leq \pi \\ 0 & \text{for} \quad |x| > \pi \end{cases}, \tag{D.0.1}$$

where $V_0 > 0$ is the potential depth. The potential in Eq. (D.0.1) can be seen as a sum of two single-well potentials, namely

$$\mathcal{V}(x) = \mathcal{V}_1(x) + \mathcal{V}_2(x)\,,$$

where

$$\mathcal{V}_1(x) = \begin{cases} -V_0 \sin^2(x) & \text{for} \quad -\pi \leq x \leq 0 \\ 0 & \text{for} \quad x < -\pi \vee x > 0 \end{cases}, \tag{D.0.2}$$

while

$$\mathcal{V}_2(x) = \mathcal{V}_1(-x)\,.$$

To simplify the notation, in the following we will use dimensionless units, i.e. $\hbar = 2m = 1$, unless otherwise specified. First, we consider the exact numerical solution for $E_\pm$ and the wave functions $\psi_\pm(E_\pm, x)$, given by Eqs. (2.3.7), where

$\overline{\Phi}^{(1)}(E,x)$ is obtained from the numerical solution of the Schrödinger equation

$$\begin{aligned} -\overline{\Phi}^{(1)\prime\prime}(E,x) &= \big(E - \big(V_0\cos^2(x) - V_0\big)\big)\,\overline{\Phi}^{(1)}(E,x) \quad \text{for} \quad -\pi \le x \le 0\,, \\ \overline{\Phi}^{(1)}(E,x) &= e^{q(x+\pi)} \quad \text{for} \quad x \le -\pi\,, \end{aligned} \tag{D.0.3}$$

where $q = \sqrt{-E}$. The eigenenergies are obtained from the matching conditions, namely $\overline{\Phi}^{(1)\prime}(E_+,0) = 0$ for the symmetric state $\psi_+(E_+,x)$ and $\overline{\Phi}^{(1)}(E_-,0) = 0$ for the antisymmetric state $\psi_-(E_-,x)$. Using Eqs. (2.3.11), we then obtain the exact WFs $\Psi_{L,R}(x)$. The eigenenergy levels

$$E_\pm = \mathcal{E}_{1,2} + \mathcal{O}(\beta^2)$$

are denoted by dashed black lines in Fig. D.1(a), while the exact left-well WF $\Psi_L(x)$ is displayed in Fig. D.1(b) (red solid curve) for lattice depth $V_0 = 4.5$. The corresponding left-well orbital $\Phi_0^{(1)}(x)$, defined in Eqs. (3.3.5), is also shown (black dashed curve). We note that the WF almost corresponds to the respective orbital inside the respective well, while its tail in the other well differs from the orbital's one, as expected from our previous analysis. To compare these results with our approximation in Eqs. (2.3.11), we consider the tunneling Hamiltonian in Eq. (3.4.1), whose parameters E_0 and Ω_0 are directly related to $E_\pm$ via Eq. (3.3.4a) and Eq. (3.3.4b), see also Eqs. (3.3.7). Using Ω_0 as energy shift

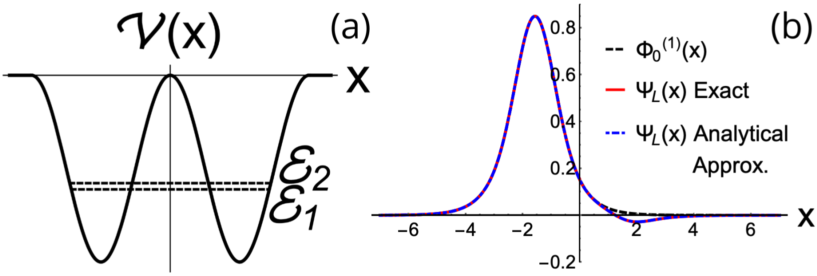

Figure D.1: (a) Symmetric double-well potential with first two exact eigenenergies $\mathcal{E}_{1,2}$ (black dashed lines). The bound states energies are: $\mathcal{E}_1 \simeq -2.75$ and $\mathcal{E}_2 \simeq -2.60$, respectively. (b) Comparison between the orbital $\Phi_0^{(1)}(x)$ (black dashed curve), the exact left-well WF $\Psi_L(x)$ (red solid curve) and the analytical approximated (neglecting $\mathcal{O}(\Omega_0^2)$ terms) left-well WF (blue dot-dashed curve) for lattice depth $V_0 = 4.5$. The exact ground-state energy and tunneling coupling are $\overline{E}_0 \simeq -2.672$ and $\overline{\Omega}_0 \simeq -0.075$, respectively, while the corresponding parameters given by the TPA are $E_0 \simeq -2.672$ and $\Omega_0 \simeq -0.075$.

in the orbital, we can evaluate the corresponding WF by using Eqs. (2.3.11), or equivalently Eqs. (3.3.23). The resulting analytical approximated WF is represented in Fig. D.1(b) (blue dot-dashed curve). For this set of parameters, our analytical approximated approach produces a result which is very close to the exact one. We expect our approach to be the more accurate the more the barrier height ensures a good localization of the left and right states in the respective well.

Appendix E

Sinusoidal double-well potential

In this Appendix, we compare the results of our analytical approximated approach (TPA) with the exact numerical evaluation of the WFs $\Psi_j(x)$ for the following sinusoidal double-well potential, shown in Fig. E.1(a):

$$\mathcal{V}(x) = \begin{cases} -V_0 \sin|x| & \text{for} \quad |x| \leq \pi \\ 0 & \text{for} \quad |x| > \pi \end{cases}, \tag{E.0.1}$$

where $V_0 > 0$ is the potential depth. The potential in Eq. (E.0.1) can be seen as a sum of two single-well potentials, namely

$$\mathcal{V}(x) = \mathcal{V}_1(x) + \mathcal{V}_2(x)\,,$$

where

$$\mathcal{V}_1(x) = \begin{cases} -V_0 \sin|x| & \text{for} \quad -\pi \leq x \leq 0 \\ 0 & \text{for} \quad x < -\pi \vee x > 0 \end{cases}, \tag{E.0.2}$$

while $\mathcal{V}_2(x) = \mathcal{V}_1(-x)$. To simplify the notation, in the following we will use dimensionless units, i.e. $\hbar = 2m = 1$, unless otherwise specified. First, we consider the exact numerical solution for $E_\pm$ and the wave functions $\psi_\pm(E_\pm, x)$, given by Eqs. (2.3.7), where $\overline{\Phi}^{(1)}(E, x)$ is obtained from the numerical solution of the Schrödinger equation

$$\begin{aligned} -\overline{\Phi}^{(1)\prime\prime}(E,x) &= (E - V_0 \sin|x|)\,\overline{\Phi}^{(1)}(E,x) \quad \text{for} \quad -\pi \leq x \leq 0\,, \\ \overline{\Phi}^{(1)}(E,x) &= e^{q(x+\pi)} \quad \text{for} \quad x \leq -\pi\,, \end{aligned} \tag{E.0.3}$$

where $q = \sqrt{-E}$. The eigenenergies are obtained from the matching conditions, namely $\overline{\Phi}^{(1)\prime}(E_+, 0) = 0$ for the symmetric state $\psi_+(E_+, x)$ and $\overline{\Phi}^{(1)}(E_-, 0) = 0$ for the antisymmetric state $\psi_-(E_-, x)$. Using Eqs. (2.3.11), we then obtain the exact WFs $\Psi_{L,R}(x)$. The eigenenergy levels

$$E_\pm = \mathcal{E}_{1,2} + \mathcal{O}(\beta^2)$$

are denoted by dashed black lines in Fig. E.1(a), while the exact left-well WF $\Psi_L(x)$ is displayed in Fig. E.1(b) (red solid curve) for lattice depth $V_0 = 4.5$. The corresponding left-well orbital $\Phi_0^{(1)}(x)$, defined in Eqs. (3.3.5), is also shown (black dashed curve). We note that the WF almost corresponds to the respective orbital inside the respective well, while its tail in the other well differs from the orbital's one, as expected from our previous analysis. To compare these results with our approximation in Eqs. (2.3.11), we consider the tunneling Hamiltonian in Eq. (3.4.1), whose parameters E_0 and Ω_0 are directly related to $E_\pm$ via Eq. (3.3.4a) and Eq. (3.3.4b), see also Eqs. (3.3.7). Using Ω_0 as energy shift in the orbital, we can evaluate the corresponding WF by using Eqs. (2.3.11), or equivalently Eqs. (3.3.23). The resulting analytical approximated WF is represented in Fig. E.1(b) (blue dot-dashed curve). For this set of parameters, our analytical approximated approach produces a result which is very close to the exact one. We expect our approach to be the more accurate the more the barrier height ensures a good localization of the left and right states in the respective well.

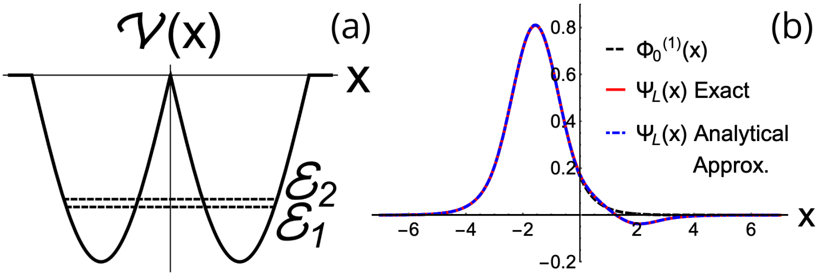

Figure E.1: (a) Symmetric double-well potential with first two exact eigenenergies $\mathcal{E}_{1,2}$ (black dashed lines). The bound states energies are: $\mathcal{E}_1 \simeq -3.2$ and $\mathcal{E}_2 \simeq -3.0$, respectively. (b) Comparison between the orbital $\Phi_0^{(1)}(x)$ (black dashed curve), the exact left-well WF $\Psi_L(x)$ (red solid curve) and the analytical approximated (neglecting $\mathcal{O}(\Omega_0^2)$ terms) left-well WF (blue dot-dashed curve) for lattice depth $V_0 = 4.5$. The exact ground-state energy and tunneling coupling are $\overline{E}_0 \simeq -3.1$ and $\overline{\Omega}_0 \simeq -0.094$, respectively, while the corresponding parameters given by the TPA are $E_0 \simeq -3.08$, $\Omega_0 \simeq -0.094$.

Appendix F

Dynamics of two distinguishable particles in a double-well potential

In this Appendix, we consider the effects of the nonstandard Hubbard terms on the dynamics of two distinguishable particles in the symmetric square double-well potential shown in Fig. 3.2. As a figure of merit of the system's dynamics, we consider the oscillation frequency of the time-dependent probability $P_{LL}(t)$, defined as the occupation probability to find both particles in the left well at time t. As initial state for the dynamics, we consider both particles placed in the infinite left-well state, and we compute the time-dependent occupation probability $P_{LL}(t)$ for the state

$$|LL\rangle \equiv \hat{a}_L^{\dagger(1)} \hat{a}_L^{\dagger(2)} |00\rangle \ .$$

The system's parameters have been chosen in such a way to have four bound energies in the double-well system, as shown in Fig. F.1. We compute the dynamics of the two particles by employing the single-band (SB) nonstandard model, where only one energy level per each well is considered, and the multiband (MB) nonstandard model, where all the energy levels (inside the potential well) are taken into account. In Fig. F.2, we show the probability $P_{LL}(t)$ to find the two particles in the left well, for two different repulsive interaction strengths, respectively in the weakly interacting regime in Fig. F.2(a) and in the strongly interacting regime in in Fig. F.2(b). Note that similar results were obtained for the case of attractive interaction strength in Fig. 3.6.

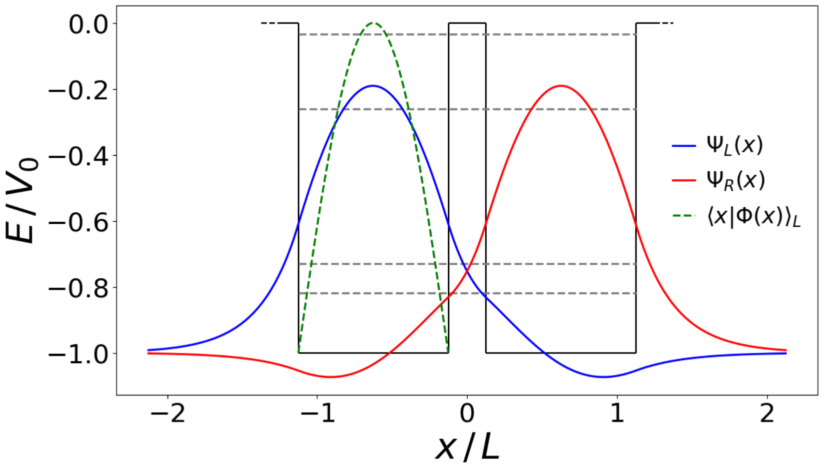

Figure F.1: Left (blue curve) and right (red curve) exact WFs for the symmetric square double-well system shown in Fig. 3.2. Parameters are $L = 2$, $b = 0.5$ and $V_0 = 5$. The eigenvalues (gray dashed lines, from bottom to top) are: $E_0 \simeq -4.089$, $E_1 \simeq -3.644$, $E_2 \simeq -1.308$, $E_3 \simeq -0.169$. $|\Phi(x)\rangle_L$ (green dashed curve) is the symmetric ground state of the infinite left-well potential considered as initial state for the system's dynamics.

Specifically, we compute $P_{LL}(t)$ by using the standard Hubbard model, the SB nonstandard model and the MB nonstandard model, the last two including novel effects given by the exact treatment of the interaction. In order to stress the importance of the PT process, we also include the no-PT model, obtained discarding artificially the effect of the PT process itself on the system's dynamics from the SB nonstandard model.

Looking at Fig. F.2, we note that the oscillation frequency of $P_{LL}(t)$ expected from the Hubbard model (yellow curve) is smaller than the one obtained from the SB and MB nonstandard models (respectively red and green curves), for both weakly and strongly repulsive interacting regimes. This highlights the role of the exact treatment of interaction in the system's dynamics, justifying the inclusion of the nonstandard terms in the Hamiltonian of the system. Specifically, we note that for weakly interacting regime, the frequency is closer to the SB nonstandard model one, being the nonstandard term less relevant in the dynamics, compared to the strongly interacting regime. Finally, we appreciate the difference between SB and MB nonstandard models, given by the different number of energy levels included in the dynamics, especially in the strongly interacting regime (the excitation probability for the higher levels is increased).

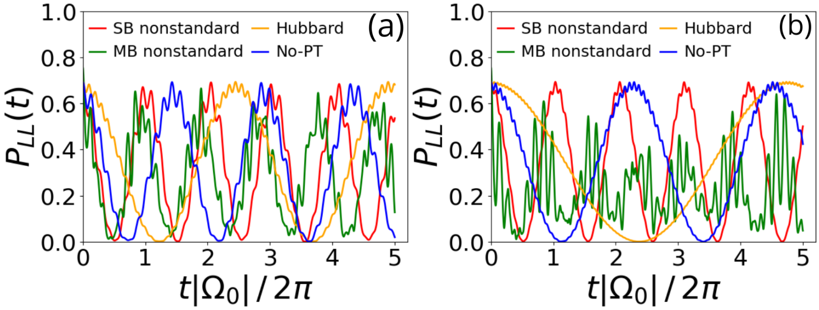

Figure F.2: Time-evolution of the probability $P_{LL}(t)$ of finding at time t two distinguishable particles together in the left well of the symmetric square double-well potential of Fig. 3.2. The particles are interacting via δ-shaped interaction potential of Eq. (3.5.1). The different models are: standard Hubbard model (orange curve), MB nonstandard model (green curve), SB nonstandard model (red curve) and no-PT model (blue curve). The double-well parameters are $L = 2$, $b = 0.5$ and $V_0 = 5$. The interaction strengths are: $U/|\Omega_0|\simeq 6$ (weakly interacting regime) in panel (a) and $U/|\Omega_0|\simeq 12$ (strongly interacting regime) in panel (b).

Appendix G

Dynamics of two bosons in a sinusoidal double-well potential: numerical analysis and experimental comparisons

G.1 Dynamics of two bosons in a sinusoidal double-well potential

In this Appendix, we analyze the dynamics of two bosons in a sinusoidal double-well potential in the parameter range between weakly and strongly interacting regimes, see Ref. [2]. Using our numerical simulations, and exploiting the versatility of our numerical method, which allows us to solve the dynamics for different potential shapes, we investigate regions of parameters relevant to the experimental results reported in Ref. [2]. Unless stated otherwise, all energies are expressed in units of the recoil energy

$$E_R = \frac{h^2}{2m\lambda^2} \,,$$

where $\lambda = 765 \; nm$ represents the periodicity of the lattice, and m is the mass of the atoms (see Sec. 3.8).

Restricting our considerations to a non-tilted double-well potential, the bosonic atoms are described by the standard Bose-Hubbard Hamiltonian, see Ref. [2]:

$$\hat{H}_{BH} = -J\left(\hat{b}_L^\dagger \hat{b}_R + \hat{b}_R^\dagger \hat{b}_L\right) + \frac{U}{2}\left[\hat{n}_L\left(\hat{n}_L - 1\right) + \hat{n}_R\left(\hat{n}_R - 1\right)\right] , \qquad \text{(G.1.1)}$$

where $J \equiv \Omega_0$ is the single-particle tunneling rate, $\hat{b}_{L,R}^{(\dagger)}$ are the annihilation (creation) operators for a bosonic particle in the ground state of the left and right wells, and U represents the interaction energy between two particles within the same well. The experimental sinusoidal double-well potential in Ref. [2] is achieved by superimposing two optical lattices with different periodic potentials: a long-lattice potential with amplitude A_{long} and wavelength 765.0 nm, and a short-lattice potential with amplitude B_{short} and wavelength 382.5 nm. The dynamics is initiated with both bosons placed in the left well, and a sudden decrease in the potential barrier depth triggers their motion. The system's dynamics is characterized by the average position

$$\langle x(t)\rangle = \frac{\langle \hat{n}_R(t)\rangle - \langle \hat{n}_L(t)\rangle}{\langle \hat{n}_R(t)\rangle + \langle \hat{n}_L(t)\rangle} , \qquad \text{(G.1.2)}$$

where $\hat{n}_{L,R}$ denotes the number of bosons in the left (L) and right (R) wells, respectively. We consider regions of parameters near to the experimental results reported in Ref. [2], namely both weakly ($U/J = 0.67$) and strongly ($U/J = 5$) interacting regimes. Our numerical model extends the standard Bose-Hubbard Hamiltonian to a single-band (SB) nonstandard Hubbard Hamiltonian, described as:

$$\begin{aligned} \hat{H} =& - J\left(\hat{b}_L^\dagger \hat{b}_R + \hat{b}_R^\dagger \hat{b}_L\right) + \frac{U}{2}\left[\hat{n}_L\left(\hat{n}_L - 1\right) + \hat{n}_R\left(\hat{n}_R - 1\right)\right] + \overline{U}\left(\hat{n}_L \hat{n}_R\right) + \\ & + \Omega_1\left[\hat{b}_L^\dagger\left(\hat{n}_L + \hat{n}_R\right)\hat{b}_R + \hat{b}_R^\dagger\left(\hat{n}_R + \hat{n}_L\right)\hat{b}_L\right] + \\ & + \Omega_2\left(\hat{b}_L^{\dagger 2}\hat{b}_R^2 + \hat{b}_R^{\dagger 2}\hat{b}_L^2\right) , \end{aligned} \qquad \text{(G.1.3)}$$

where $\overline{U}$ represents the nearest-neighbor interaction, Ω_1 denotes the density-induced tunneling (DT) term, and Ω_2 represents the pair tunneling (PT) term.

To simulate experimental conditions, we vary the ratio U/J as a function of the lattice depth V_0. From Ref. [86], we know that the ratio U/J increases exponentially with the lattice depth V_0, as follows:

$$\frac{U}{J} \sim \frac{a}{d}\exp\left(\sqrt{4V_0/E_R}\right) , \qquad \text{(G.1.4)}$$

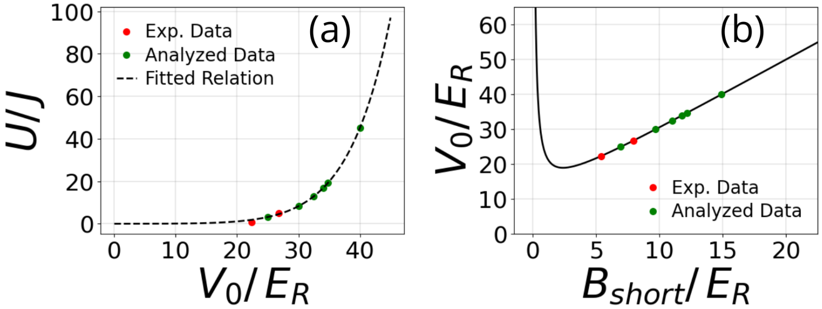

Figure G.1: Panel (a): exponential relation between the interaction-to-tunneling ratio U/J and the lattice depth V_0/E_R as described by Eq. (G.1.4). Red dots: parameter regimes for weakly ($U/J = 0.67$) and strongly ($U/J = 5$) interacting bosons, as taken from Ref. [2]. Green dots: data utilized in our numerical simulations ($U/J = 3.19, 8.27, 12.94, 16.78, 19.24, 45.04$) and ($V_0/E_R = 25, 30, 32.5, 34, 34.8, 40$). Panel (b): relation between the lattice depth V_0 and the short-lattice amplitude B_{short}. The short-lattice amplitude B_{short} is varied to mimic experimental conditions using two superimposed optical periodic potentials.

where a is the scattering length and $d = \lambda/2$ is the lattice spacing (see Sec. 3.8). Fig. G.1(a) illustrates the relation in Eq. (G.1.4), highlighting both the weakly and strongly interacting regimes from Ref. [2] (red dots) and our analyzed data (green dots). Fig. G.1(b) shows the relation between lattice depth V_0 and the short-lattice amplitude B_{short}.

The average position of two interacting bosons, initially placed in the infinite left-well state, for various values of U/J and corresponding lattice depths V_0, spanning regions near to weakly ($U/J = 0.67$) and strongly ($U/J = 5$) interacting regimes, is shown in Fig. G.2. We compare the standard Hubbard model (orange curve) with the SB nonstandard model (red curve). For further comparison, we also include the multiband (MB) nonstandard model (green curve, obtained numerically) to highlight the region where the SB approximation holds. As one can see, the nonstandard model predicts significantly different average positions compared to the standard Hubbard model, both in amplitude and frequency, underscoring the importance of nonstandard terms in capturing the system's dynamics. Moreover, in all panels of Fig. G.2, it is clear that the SB approximation is quite accurate for the interaction values considered. Nevertheless, it is important to observe that the SB nonstandard model closely approximates the MB nonstandard model when $U \ll \Delta E$ (i.e., when the interaction energy U does not exceed ΔE, ensuring that the energy levels are

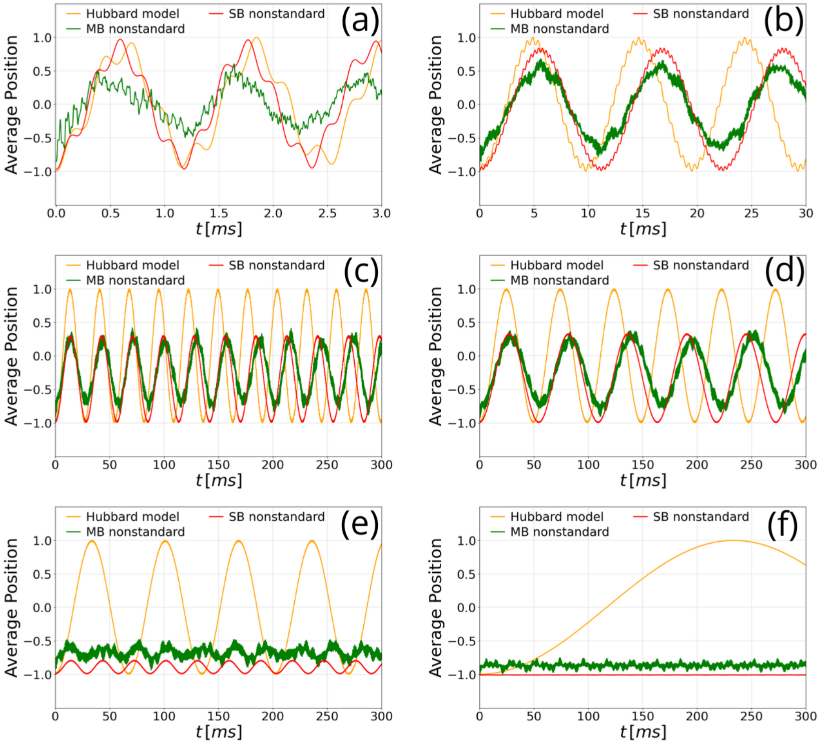

Figure G.2: Average position of two interacting bosons as a function of time. The dynamics of two bosons initially placed in the left well are simulated for different interaction regimes, with varying U/J ratios (from Fig. G.1). The plot compares the average position predicted by the standard Hubbard model (orange curve), the SB nonstandard model (red curve), and the MB nonstandard model (green curve). Panel (a): $|\Omega_1/\Omega_0|= 0.13$, $|\Omega_2/\Omega_0|= 0.04$, $U/\Delta E = 0.15$. Panel (b): $|\Omega_1/\Omega_0|= 0.12$, $|\Omega_2/\Omega_0|= 6 \cdot 10^{-3}$, $U/\Delta E = 0.08$. Panel (c): $|\Omega_1/\Omega_0|= 0.17$, $|\Omega_2/\Omega_0|= 3 \cdot 10^{-3}$, $U/\Delta E = 0.06$. Panel (d): $|\Omega_1/\Omega_0|= 0.08$, $|\Omega_2/\Omega_0|= 2 \cdot 10^{-3}$, $U/\Delta E = 0.05$. Panel (e): $|\Omega_1/\Omega_0|= 0.08$, $|\Omega_2/\Omega_0|= 2 \cdot 10^{-3}$, $U/\Delta E = 0.04$. Panel (f): $|\Omega_1/\Omega_0|= 3.23$, $|\Omega_2/\Omega_0|= 0.12$, $U/\Delta E = 0.03$.

not widely spaced).

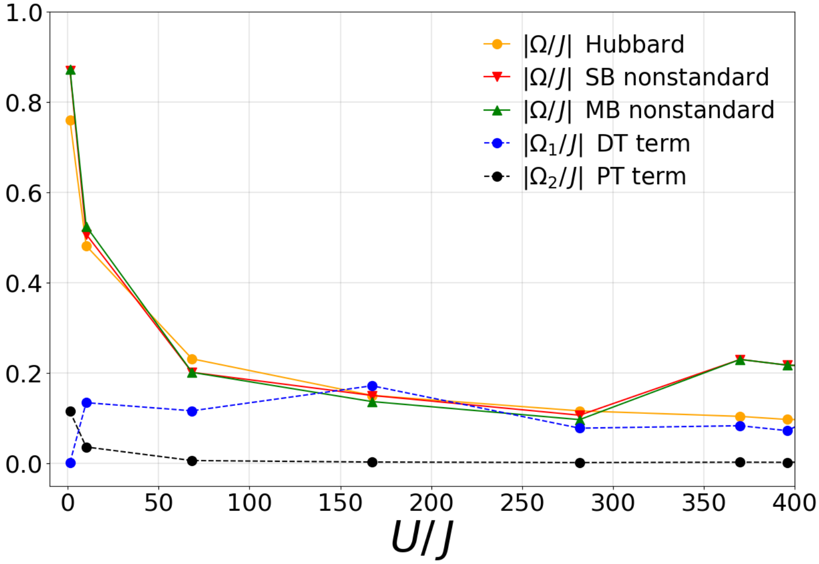

Figure G.3: Frequency spectrum of the dynamics of two bosons for different models, as a function of the interaction-to-hopping parameter U/J. The plot shows the frequencies of oscillation for the system as predicted by the standard Hubbard model, the SB nonstandard model, and the MB nonstandard model. The density-induced tunneling (DT) term Ω_1 and the pair tunneling (PT) term Ω_2 are also displayed.

G.2 Metal-insulator phase transition

A sharp transition from low to high U/J values is evident in Fig. G.2. Specifically, at low U/J values, the bosons tunnel between wells (metallic phase), while for large enough U/J, they remain localized in the initial well (insulating phase). This transition occurs in both the standard Bose-Hubbard model and the nonstandard models, but at considerably larger U/J values. As U/J increases, both the oscillation frequency and the amplitude of oscillation of the average position decrease (see the yellow curve for the Hubbard model), highlighting the emergence of an insulating phase.

In the SB and MB nonstandard models, the metal-insulator transition still occurs (see the red and green curves, respectively), but at a lower "critical"U/J value compared to the standard Hubbard model. This shift is primarly due to the effect of DT on the single-particle tunneling. An effective single-particle tunneling amplitude, $\Omega_{eff} = \Omega_0 + \Omega_1$, arises, which is interaction-dependent, as detailed in Refs. [43, 45]. For repulsive interaction, Ω_0 is reduced by Ω_1, resulting in a lower Ω_{eff} and, consequently, a shifted phase transition with respect to U/J. To confirm such a view, Fig. G.3 shows the dynamical frequencies predicted by the standard Hubbard model and both the SB and MB nonstandard models, along with the DT term Ω_1 and PT term Ω_2. Notably, the latter is largely irrelevant in the transition to the localized phase.

In conclusion, under the given experimental conditions, it is challenging to find interesting experimental parameter regions where the PT term is significant. This is because increasing U also necessitates increasing V_0, at variance with the theoretical case discussed. Despite this limitation, the presence of DT term requires a significant modification of the critical interaction strength at which the insulating phase appears. This suggests that the metal-insulator transition could be highly sensitive to the additional nonstandard terms considered in this work. On the other hand, alternative experimental setups may be needed to explore the relevance of the PT term further.

Bibliography

[1] D.-S. Lühmann, O. Jürgensen, and K. Sengstock, “Multi-orbital and density-induced tunneling of bosons in optical lattices,” *New Journal of Physics*, vol. 14, p. 033021, Mar 2012.

[2] S. Fölling, S. Trotzky, P. Cheinet, M. Feld, R. Saers, A. Widera, T. Müller, and I. Bloch, “Direct observation of second-order atom tunnelling,” *Nature*, vol. 448, Aug 2007.

[3] D. P. Arovas, E. Berg, S. A. Kivelson, and S. Raghu, “The Hubbard model,” *Annual Review of Condensed Matter Physics*, vol. 13, no. 1, pp. 239–274, 2022.

[4] G. M. Andolina, F. M. D. Pellegrino, V. Giovannetti, A. H. MacDonald, and M. Polini, “Cavity quantum electrodynamics of strongly correlated electron systems: A no-go theorem for photon condensation,” *Phys. Rev. B*, vol. 100, p. 121109, Sept 2019.

[5] G. M. Andolina, F. M. D. Pellegrino, V. Giovannetti, A. H. MacDonald, and M. Polini, “Theory of photon condensation in a spatially varying electromagnetic field,” *Phys. Rev. B*, vol. 102, p. 125137, Sept 2020.

[6] G. Mazza, A. Amaricci, M. Capone, and M. Fabrizio, “Field-driven Mott gap collapse and resistive switch in correlated insulators,” *Phys. Rev. Lett.*, vol. 117, p. 176401, Oct 2016.

[7] S. Miyasaka, Y. Okimoto, and Y. Tokura, “Anisotropy of Mott-Hubbard gap transitions due to spin and orbital ordering in $LaVO_3$ and YVO_3,” *Journal of the Physical Society of Japan*, vol. 71, no. 9, pp. 2086–2089, 2002.

[8] A. Georges, G. Kotliar, W. Krauth, and M. J. Rozenberg, “Dynamical mean-field theory of strongly correlated fermion systems and the limit of infinite dimensions,” *Rev. Mod. Phys.*, vol. 68, pp. 13–125, Jan 1996.

[9] J. K. Freericks and V. Zlatić, "Exact dynamical mean-field theory of the Falicov-Kimball model," *Rev. Mod. Phys.*, vol. 75, pp. 1333–1382, Oct 2003.

[10] H. Aoki, N. Tsuji, M. Eckstein, M. Kollar, T. Oka, and P. Werner, "Nonequilibrium dynamical mean-field theory and its applications," *Rev. Mod. Phys.*, vol. 86, pp. 779–837, Jun 2014.

[11] T. Oka and H. Aoki, "Photovoltaic Hall effect in graphene," *Phys. Rev. B*, vol. 79, p. 081406, Feb 2009.

[12] H.-C. Jiang and T. P. Devereaux, "Superconductivity in the doped Hubbard model and its interplay with next-nearest hopping t'," *Science*, vol. 365, pp. 1424 – 1428, Sept 2018.

[13] P. A. Lee, N. Nagaosa, and X.-G. Wen, "Doping a Mott insulator: Physics of high-temperature superconductivity," *Rev. Mod. Phys.*, vol. 78, pp. 17–85, Jan 2006.

[14] E. Dagotto, "Correlated electrons in high-temperature superconductors," *Rev. Mod. Phys.*, vol. 66, pp. 763–840, Jul 1994.

[15] J. G. Bednorz and K. A. Müller, "Possible high-T_c superconductivity in the Ba-La-Cu-O system," *Physik B - Condensed Matter*, vol. 64, Jun 1986.

[16] Y. Cao, V. Fatemi, A. Demir, S. Fang, S. L. Tomarken, J. Y. Luo, J. D. Sanchez-Yamagishi, K. Watanabe, T. Taniguchi, E. Kaxiras, R. C. Ashoori, and P. Jarillo-Herrero, "Correlated insulator behaviour at half-filling in magic-angle graphene superlattices," *Nature*, vol. 556, pp. 80–84, Mar 2018.

[17] P. Anderson, "Resonating valence bonds: A new kind of insulator?," *Materials Research Bulletin*, vol. 8, pp. 153–160, Feb 1973.

[18] A. Brinkman and H. Hilgenkamp, "Electron-hole coupling in high-T_c cuprate superconductors," *Physica C*, vol. 422, pp. 71–75, Jun 2005.

[19] P. A. Lee, "From high temperature superconductivity to quantum spin liquid: progress in strong correlation physics," *Reports on Progress in Physics*, vol. 71, p. 012501, Dec 2007.

[20] T. Yanagisawa, "Physics of the Hubbard model and high temperature superconductivity," *Journal of Physics: Conference Series*, vol. 108, p. 012010, Mar 2008.

[21] K. Haule and G. Kotliar, “Strongly correlated superconductivity: A plaquette dynamical mean-field theory study,” *Phys. Rev. B*, vol. 76, p. 104509, Sept 2007.

[22] E. Gull and A. J. Millis, “Energetics of superconductivity in the two-dimensional Hubbard model,” *Phys. Rev. B*, vol. 86, p. 241106, Dec 2012.

[23] C. Honerkamp, “Density waves and cooper pairing on the honeycomb lattice,” *Phys. Rev. Lett.*, vol. 100, p. 146404, Apr 2008.

[24] J. G. Bednorz and K. A. Müller, “Perovskite-type oxides - the new approach to high-T_c superconductivity,” *Rev. Mod. Phys.*, vol. 60, pp. 585–600, Jul 1988.

[25] S. Raghu, S. A. Kivelson, and D. J. Scalapino, “Superconductivity in the repulsive Hubbard model: An asymptotically exact weak-coupling solution,” *Phys. Rev. B*, vol. 81, p. 224505, Jun 2010.

[26] A. I. Lichtenstein and M. I. Katsnelson, “Antiferromagnetism and d-wave superconductivity in cuprates: A cluster dynamical mean-field theory,” *Phys. Rev. B*, vol. 62, pp. R9283–R9286, Oct 2000.

[27] M. Sigrist and K. Ueda, “Phenomenological theory of unconventional superconductivity,” *Rev. Mod. Phys.*, vol. 63, pp. 239–311, Apr 1991.

[28] J. Zaanen, G. A. Sawatzky, and J. W. Allen, “Band gaps and electronic structure of transition-metal compounds,” *Phys. Rev. Lett.*, vol. 55, pp. 418–421, Jul 1985.

[29] M. Ogata and H. Fukuyama, “The t-j model for the oxide high-T_c superconductors,” *Reports on Progress in Physics*, vol. 71, p. 036501, Feb 2008.

[30] J. M. Kosterlitz and D. J. Thouless, “Ordering, metastability and phase transitions in two-dimensional systems,” *Journal of Physics C: Solid State Physics*, vol. 6, p. 1181, Apr 1973.

[31] D. J. Scalapino, “The case for $d_{x^2-y^2}$ pairing in the cuprate superconductors,” *Physics Reports*, vol. 250, pp. 329–365, Jan 1995.

[32] P. J. Hirschfeld, M. M. Korshunov, and I. I. Mazin, “Gap symmetry and structure of Fe-based superconductors,” *Reports on Progress in Physics*, vol. 74, p. 124508, Oct 2011.

[33] D. S. Fisher, “Random transverse field Ising spin chains,” *Phys. Rev. Lett.*, vol. 69, pp. 534–537, Jul 1992.

[34] D. Loss and D. P. DiVincenzo, "Quantum computation with quantum dots," *Phys. Rev. A*, vol. 57, pp. 120–126, Jan 1998.

[35] N. F. Mott, "Metal-insulator transition," *Rev. Mod. Phys.*, vol. 40, pp. 677–683, Oct 1968.

[36] O. Gunnarsson, E. Koch, and R. M. Martin, "Mott-Hubbard insulators for systems with orbital degeneracy," *Phys. Rev. B*, vol. 56, pp. 1146–1152, Jul 1997.

[37] Y. Nagaoka, "Ferromagnetism in a narrow, almost half-filled s band," *Phys. Rev.*, vol. 147, pp. 392–405, Jul 1966.

[38] F. D. M. Haldane, "Fractional quantization of the Hall effect: A hierarchy of incompressible quantum fluid states," *Phys. Rev. Lett.*, vol. 51, pp. 605–608, Aug 1983.

[39] J. Hubbard, "Electron correlations in narrow energy bands," *Proceedings of the Royal Society of London. Series A, Mathematical and Physical Sciences*, vol. 276, pp. 238–257, Nov 1963.

[40] M. C. Gutzwiller, "Effect of correlation on the ferromagnetism of transition metals," *Phys. Rev. Lett.*, vol. 10, pp. 159–162, Mar 1963.

[41] F. H. L. Essler, H. Frahm, F. Göhmann, A. Klümper, and V. E. Korepin, *The One-Dimensional Hubbard Model.* Cambridge University Press, 2005.

[42] K. Held, "Electronic structure calculations using dynamical mean field theory," *Advances in Physics*, vol. 56, pp. 829–926, Oct 2007.

[43] O. Dutta, M. Gajda, P. Hauke, M. Lewenstein, D.-S. Lühmann, B. A. Malomed, T. Sowiński, and J. Zakrzewski, "Non-standard Hubbard models in optical lattices: a review," *Reports on Progress in Physics*, vol. 78, p. 066001, May 2015.

[44] O. Jürgensen, K. Sengstock, and D.-S. Lühmann, "Density-induced processes in quantum gas mixtures in optical lattices," *Phys. Rev. A*, vol. 86, p. 043623, Oct 2012.

[45] O. Jürgensen, F. Meinert, M. J. Mark, H.-C. Nägerl, and D.-S. Lühmann, "Observation of density-induced tunneling," *Phys. Rev. Lett.*, vol. 113, p. 193003, Nov 2014.

[46] M. Maik, P. Hauke, O. Dutta, M. Lewenstein, and J. Zakrzewski, "Density-dependent tunneling in the extended Bose-Hubbard model," *New Journal of Physics*, vol. 15, p. 113041, Nov 2013.

[47] J. Hirsch, “Inapplicability of the Hubbard model for the description of real strongly correlated electrons,” *Physica B: Condensed Matter*, vol. 199-200, pp. 366–372, Apr 1994.

[48] K. Winkler, G. Thalhammer, F. Lang, R. Grimm, J. Hecker Denschlag, A. J. Daley, A. Kantian, H. P. Büchler, and P. Zoller, “Repulsively bound atom pairs in an optical lattice,” *Nature*, vol. 441, Jun 2006.

[49] S. Mondal, A. Kshetrimayum, and T. Mishra, “Two-body repulsive bound pairs in a multibody interacting Bose-Hubbard model,” *Phys. Rev. A*, vol. 102, p. 023312, Aug 2020.

[50] M. Zendra, F. Borgonovi, G. L. Celardo, and S. Gurvitz, “Nonstandard Hubbard model and electron pairing,” *Phys. Rev. B*, vol. 109, p. 195137, May 2024.

[51] M. Zendra, F. Borgonovi, G. L. Celardo, and S. Gurvitz, “Many-body tunneling in a double-well potential,” 2024. Accepted for publication by *Phys. Rev. A*.

[52] S. Hunn, K. Zimmermann, M. Hiller, and A. Buchleitner, “Tunneling decay of two interacting bosons in an asymmetric double-well potential: A spectral approach,” *Phys. Rev. A*, vol. 87, p. 043626, Apr 2013.

[53] S. A. Gurvitz, “Two-electron correlated motion due to coulomb repulsion,” Mar 2002.

[54] D. Petrosyan, B. Schmidt, J. R. Anglin, and M. Fleischhauer, “Quantum liquid of repulsively bound pairs of particles in a lattice,” *Phys. Rev. A*, vol. 76, p. 033606, Sept 2007.

[55] T. Terashige, T. Ono, T. Miyamoto, T. Morimoto, H. Yamakawa, N. Kida, T. Ito, T. Sasagawa, T. Tohyama, and H. Okamoto, “Doublon-holon pairing mechanism via exchange interaction in two-dimensional cuprate Mott insulators,” *Science Advances*, vol. 5, p. eaav2187, Jun 2019.

[56] W. Hou, Y. Wang, J. Wei, Z. Zhu, and Y. Yan, “Many-body tunneling and nonequilibrium dynamics of doublons in strongly correlated quantum dots,” *Scientific Reports volume 7, Article number: 2486*, vol. 7, May 2017.

[57] J. Gong, L. Morales-Molina, and P. Hänggi, “Many-body coherent destruction of tunneling,” *Phys. Rev. Lett.*, vol. 103, p. 133002, Sept 2009.

[58] J. E. Hirsch and F. Marsiglio, “Superconducting state in an oxygen hole metal,” *Phys. Rev. B*, vol. 39, pp. 11515–11525, Jun 1989.

[59] I. N. Karnaukhov, "Model of fermions with correlated hopping (integrable cases)," *Phys. Rev. Lett.*, vol. 73, pp. 1130–1133, Aug 1994.

[60] J. de Boer, V. E. Korepin, and A. Schadschneider, "η pairing as a mechanism of superconductivity in models of strongly correlated electrons," *Phys. Rev. Lett.*, vol. 74, pp. 789–792, Jan 1995.

[61] G. I. Japaridze and A. P. Kampf, "Weak-coupling phase diagram of the extended Hubbard model with correlated-hopping interaction," *Phys. Rev. B*, vol. 59, pp. 12822–12829, May 1999.

[62] A. Anfossi, P. Giorda, A. Montorsi, and F. Traversa, "Two-point versus multipartite entanglement in quantum phase transitions," *Phys. Rev. Lett.*, vol. 95, p. 056402, Jul 2005.

[63] A. Dobry and A. A. Aligia, "Quantum phase diagram of the half filled Hubbard model with bond-charge interaction," *Nuclear Physics B*, vol. 843, pp. 767–783, Feb 2011.

[64] A. Montorsi, U. Bhattacharya, D. González-Cuadra, M. Lewenstein, G. Palumbo, and L. Barbiero, "Interacting second-order topological insulators in one-dimensional fermions with correlated hopping," *Phys. Rev. B*, vol. 106, p. L241115, Dec 2022.

[65] R. Strack and D. Vollhardt, "Hubbard model with nearest-neighbor and bond-charge interaction: Exact ground-state solution in a wide range of parameters," *Phys. Rev. Lett.*, vol. 70, pp. 2637–2640, Apr 1993.

[66] J. Hirsch, "Bond-charge repulsion and hole superconductivity," *Physica C: Superconductivity and its Applications*, vol. 158, pp. 326–336, May 1989.

[67] A. A. Aligia, A. Anfossi, L. Arrachea, C. Degli Esposti Boschi, A. O. Dobry, C. Gazza, A. Montorsi, F. Ortolani, and M. E. Torio, "Incommensurability and unconventional superconductor to insulator transition in the Hubbard model with bond-charge interaction," *Phys. Rev. Lett.*, vol. 99, p. 206401, Nov 2007.

[68] Y.-J. Kim, "Cooper pair wavefunction approach to the Josephson effect," *Journal of Applied Physics*, vol. 103, p. 103902, May 2008.

[69] A. J. Leggett, *Quantum liquids: Bose condensation and Cooper pairing in condensed-matter systems.* Oxford University press, Sept 2006.

[70] J. E. Hirsch, "Electron- and hole-hopping amplitudes in a diatomic molecule," *Phys. Rev. B*, vol. 48, pp. 3327–3339, Aug 1993.

[71] J. C. Amadon and J. E. Hirsch, "Metallic ferromagnetism in a single-band model: Effect of band filling and coulomb interactions," *Phys. Rev. B*, vol. 54, pp. 6364–6375, Sept 1996.

[72] P. Weckesser, K. Srakaew, T. Blatz, D. Wei, D. Adler, S. Agrawal, A. Bohrdt, I. Bloch, and J. Zeiher, "Realization of a Rydberg-dressed extended Bose Hubbard model," May 2024.

[73] A. Knothe and G. Burkard, "Extended Hubbard model describing small multi-dot arrays in bilayer graphene," Jun 2024.

[74] I. Affleck and J. B. Marston, "Large-n limit of the Heisenberg-Hubbard model: Implications for high-T_c superconductors," *Phys. Rev. B*, vol. 37, pp. 3774–3777, Mar 1988.

[75] V. F. Gilmutdinov, M. A. Timirgazin, and A. K. Arzhnikov, "Interplay of magnetism and superconductivity in 2D extended Hubbard model," *Journal of Magnetism and Magnetic Materials*, vol. 560, p. 169605, Oct 2022.

[76] W.-C. Chen, Y. Wang, and C.-C. Chen, "Superconducting phases of the square-lattice extended Hubbard model," *Phys. Rev. B*, vol. 108, p. 064514, Aug 2023.

[77] G. D. Adebanjo, J. P. Hague, and P. E. Kornilovitch, "Ubiquitous light real-space pairing from long-range hopping and interactions," *Physics Letters A*, vol. 507, p. 129474, May 2024.

[78] S. Kundu and D. Sénéchal, "CDMFT+HFD: An extension of dynamical mean field theory for nonlocal interactions applied to the single band extended Hubbard model," *SciPost Physics Core*, vol. 7, Jun 2024.

[79] K. Wrześniewski, T. Ślusarski, and I. Weymann, "Nonmonotonic buildup of spin-singlet correlations in a double quantum dot," *Phys. Rev. B*, vol. 108, p. 144307, Oct 2023.

[80] P. Frey, L. Hackl, and S. Rachel, "Hilbert space fragmentation and interaction-induced localization in the extended Fermi-Hubbard model," *Phys. Rev. B*, vol. 106, p. L220301, Dec 2022.

[81] A. Nico-Katz, G. Jaliel, P. Atkinson, T. A. Mitchell, D. A. Ritchie, C. G. Smith, and S. Bose, "Identifying many-body localization in realistic dot arrays," 2023.

[82] O. Dutta, A. Eckardt, P. Hauke, B. Malomed, and M. Lewenstein, "Bose-Hubbard model with occupation-dependent parameters," *New Journal of Physics*, vol. 13, p. 023019, Feb 2011.

[83] T. Sowiński, O. Dutta, P. Hauke, L. Tagliacozzo, and M. Lewenstein, "Dipolar molecules in optical lattices," *Phys. Rev. Lett.*, vol. 108, p. 115301, Mar 2012.

[84] J.-M. Lihm and C.-H. Park, "Wannier function perturbation theory: Localized representation and interpolation of wave function perturbation," *Phys. Rev. X*, vol. 11, p. 041053, Dec 2021.

[85] N. Marzari, A. A. Mostofi, J. R. Yates, I. Souza, and D. Vanderbilt, "Maximally localized wannier functions: Theory and applications," *Rev. Mod. Phys.*, vol. 84, pp. 1419–1475, Oct 2012.

[86] I. Bloch, J. Dalibard, and W. Zwerger, "Many-body physics with ultracold gases," *Rev. Mod. Phys.*, vol. 80, pp. 885–964, Jul 2008.

[87] M. Lewenstein, A. Sanpera, V. Ahufinger, B. Damski, A. Sen(De), and U. Sen, "Ultracold atomic gases in optical lattices: mimicking condensed matter physics and beyond," *Advances in Physics*, vol. 56, pp. 243–379, May 2007.

[88] S. Hild, T. Fukuhara, P. Schauß, J. Zeiher, M. Knap, E. Demler, I. Bloch, and C. Gross, "Far-from-equilibrium spin transport in Heisenberg quantum magnets," *Phys. Rev. Lett.*, vol. 113, p. 147205, Oct 2014.

[89] F. Meinert, M. J. Mark, E. Kirilov, K. Lauber, P. Weinmann, M. Gröbner, and H.-C. Nägerl, "Interaction-induced quantum phase revivals and evidence for the transition to the quantum chaotic regime in 1D atomic bloch oscillations," *Phys. Rev. Lett.*, vol. 112, p. 193003, May 2014.

[90] M. Greiner, O. Mandel, T. Esslinger, T. Haensch, and I. Bloch, "Quantum phase transition from a superfluid to a Mott insulator in a gas of ultracold atoms," *Nature*, vol. 415, pp. 39–44, Jan 2002.

[91] D. Jaksch and P. Zoller, "The cold atom Hubbard toolbox," *Annals of Physics*, vol. 315, pp. 52–79, Jan 2005.

[92] A. Bohrdt, L. Homeier, C. Reinmoser, E. Demler, and F. Grusdt, "Exploration of doped quantum magnets with ultracold atoms," *Annals of Physics*, vol. 435, p. 168651, Oct 2021.

[93] S. Trotzky, P. Cheinet, S. Fölling, M. Feld, U. Schnorrberger, A. M. Rey, A. Polkovnikov, E. A. Demler, M. D. Lukin, and I. Bloch, "Time-resolved observation and control of superexchange interactions with ultracold atoms in optical lattices," *Science*, vol. 319, pp. 295–299, Jan 2008.

[94] F. Schäfer, M. A. Bastarrachea-Magnani, A. U. J. Lode, L. d. F. de Parny, and A. Buchleitner, "Spectral structure and many-body dynamics of ultracold bosons in a double-well," *Entropy*, vol. 22, Mar 2020.

[95] C. Gross and I. Bloch, "Quantum simulations with ultracold atoms in optical lattices," *Science*, vol. 357, pp. 995–1001, Sept 2017.

[96] R. Ma, M. E. Tai, P. M. Preiss, W. S. Bakr, J. Simon, and M. Greiner, "Photon-assisted tunneling in a biased strongly correlated Bose gas," *Phys. Rev. Lett.*, vol. 107, p. 095301, Aug 2011.

[97] F. Meinert, M. J. Mark, K. Lauber, A. J. Daley, and H.-C. Nägerl, "Floquet engineering of correlated tunneling in the Bose-Hubbard model with ultracold atoms," *Phys. Rev. Lett.*, vol. 116, p. 205301, May 2016.

[98] F. Görg, M. Messer, K. Sandholzer, G. Jotzu, R. Desbuquois, and T. Esslinger, "Enhancement and sign change of magnetic correlations in a driven quantum many-body system," *Nature*, vol. 553, Jan 2018.

[99] M. Kremer, R. Sachdeva, A. Benseny, and T. Busch, "Interaction-induced effects on Bose-Hubbard parameters," *Phys. Rev. A*, vol. 96, p. 063611, Dec 2017.

[100] S. Zöllner, H.-D. Meyer, and P. Schmelcher, "Tunneling dynamics of a few bosons in a double well," *Phys. Rev. A*, vol. 78, p. 013621, Jul 2008.

[101] L. C., U. Bhattacharya, T. Grass, R. W. Chhajlany, T. Salamon, K. Baldwin, L. Pfeiffer, M. Lewenstein, M. Holzmann, and F. Dubin, "Extended Bose-Hubbard model with dipolar excitons," *Nature*, vol. 609, pp. 485–489, Sept 2022.

[102] P. W. Anderson, "The resonating valence bond state in La_2CuO_4 and superconductivity," *Science*, vol. 235, pp. 1196–1198, Mar 1987.

[103] M. Imada, A. Fujimori, and Y. Tokura, "Metal-insulator transitions," *Rev. Mod. Phys.*, vol. 70, pp. 1039–1263, Oct 1998.

[104] N. F. Mott, "The basis of the electron theory of metals, with special reference to the transition metals," *Proceedings of the Physical Society. Section A*, vol. 62, p. 416, Jul 1949.

[105] S. A. Gurvitz and G. Kalbermann, "Decay width and the shift of a quasistationary state," *Phys. Rev. Lett.*, vol. 59, pp. 262–265, Jul 1987.

[106] S. A. Gurvitz, "Novel approach to tunneling problems," *Phys. Rev. A*, vol. 38, pp. 1747–1759, Aug 1988.

[107] S. A. Gurvitz, P. B. Semmes, W. Nazarewicz, and T. Vertse, “Modified two-potential approach to tunneling problems,” *Phys. Rev. A*, vol. 69, p. 042705, Apr 2004.

[108] J. Bardeen, “Tunnelling from a many-particle point of view,” *Phys. Rev. Lett.*, vol. 6, pp. 57–59, Jan 1961.

[109] D. D. Vu and S. Das Sarma, “Moiré versus Mott: Incommensuration and interaction in one-dimensional bichromatic lattices,” *Phys. Rev. Lett.*, vol. 126, p. 036803, Jan 2021.

[110] R. Bistritzer and A. H. MacDonald, “Moiré bands in twisted double-layer graphene,” *Proceedings of the National Academy of Sciences*, vol. 108, pp. 12233–12237, Jul 2011.

[111] S. M. Chan, B. Grémaud, and G. G. Batrouni, “Pairing and superconductivity in quasi-one-dimensional flat-band systems: Creutz and sawtooth lattices,” *Phys. Rev. B*, vol. 105, p. 024502, Jan 2022.

[112] Y. Cao, V. Fatemi, S. Fang, K. Watanabe, T. Taniguchi, E. Kaxiras, and P. Jarillo-Herrero, “Unconventional superconductivity in magic-angle graphene superlattices,” *Nature*, vol. 556, pp. 43–50, Apr 2018.

[113] X.-F. Zhou, Y.-S. Zhang, and G.-C. Guo, “Pair tunneling of bosonic atoms in an optical lattice,” *Phys. Rev. A*, vol. 80, p. 013605, Jul 2009.

[114] S. A. Gurvitz, *Two-potential approach to multi-dimensional tunneling*, p. 91–103. World Scientific, Oct 2002.

[115] A. M. Lane and R. G. Thomas, “R-matrix theory of nuclear reactions,” *Rev. Mod. Phys.*, vol. 30, pp. 257–353, Apr 1958.

[116] E. Vermeyen, C. A. R. Sá de Melo, and J. Tempere, “Exchange interactions and itinerant ferromagnetism in ultracold Fermi gases,” *Phys. Rev. A*, vol. 98, p. 023635, Aug 2018.

[117] L. Yang, L. Guan, and H. Pu, “Strongly interacting quantum gases in one-dimensional traps,” *Phys. Rev. A*, vol. 91, p. 043634, Apr 2015.

[118] T. Esslinger, “Fermi-Hubbard physics with atoms in an optical lattice,” *Annual Review of Condensed Matter Physics*, vol. 1, pp. 129–152, Aug 2010.

[119] H. P. Büchler, “Microscopic derivation of Hubbard parameters for cold atomic gases,” *Phys. Rev. Lett.*, vol. 104, p. 090402, Mar 2010.

[120] H. S. Adlong, J. Levinsen, and M. M. Parish, “Microscopic theory of the Hubbard interaction in low-dimensional optical lattices,” 2024.

[121] E. Dagotto, “High-T_c superconductors: Numerical studies of the Hubbard model,” *AIP Conference Proceedings*, vol. 260, pp. 172–179, Jul 1992.

[122] D. Jaksch, C. Bruder, J. I. Cirac, C. W. Gardiner, and P. Zoller, “Cold bosonic atoms in optical lattices,” *Physical Review Letters*, vol. 81, pp. 3108–3111, Oct 1998.

[123] D. J. Thouless, *The Quantum Mechanics of Many-body Systems.* Academic Press, 1961.

List of publications

- M. Zendra, F. Borgonovi, G. L. Celardo and S. Gurvitz, "Nonstandard Hubbard model and electron pairing", *Phys. Rev. B*, vol. 109, p. 195137, 2024.
- M. Zendra, F. Borgonovi, G. L. Celardo and S. Gurvitz, "Many-body tunneling in a double-well potential", *arXiv*, eprint: 2409.04311, 2024 (accepted for publication by *Phys. Rev. A*).

FACOLTÁ DI SCIENZE MATEMATICHE, FISICHE E NATURALI
DIPARTIMENTO DI MATEMATICA E FISICA
THEORETICAL PHYSICS GROUP
Via della Garzetta 48
25133 Brescia
matteo.zendra@unicatt.it

FACULTY OF SCIENCE
DEPARTMENT OF PHYSICS AND ASTRONOMY
THEORETICAL PHYSICS GROUP
Celestijnenlaan 200D
B-3001 Leuven
matteo.zendra@kuleuven.be
https://fys.kuleuven.be/itf